NTNU

Norwegian University of
Science and Technology

# A Comparison of Analytical and Experimental Procedures to Verify a Lumped Drill String Element Model

Raz Taha Hassan

Petroleum Geoscience and Engineering
Submission date: June 2016
Supervisor: Sigve Hovda, IPT

Norwegian University of Science and Technology
Department of Petroleum Engineering and Applied Geophysics

## Abstract

A study of axial vibrations in a vertical drill string is conducted using a spring-mass-damper model with $n$-coupled elements. The main motivation behind this is to describe the axial vibrations using a simple mathematical model that allows for a substantial interpretation and application of control theory. In other words, the analytical model describing the test segments in this thesis can easily apply to other vertical drill string models, with a few adjustments. The study attempts to answer the following research question:

**To what extent can the lumped element model be used to replicate and predict axial vibrations in a vertical drill string?**

The analytical model is derived and tested on the following three scenarios. The first scenario considers only the transient state of the model. It divides into overdamped, critically damped, and underdamped systems. This scenario features both physical experiments and numerical simulations. Results from experiments and numerical simulations are presented graphically in order to identify similarities between the two systems. The second scenario considers the step response as the driving force, and the last scenario introduces a sinusoidal driving force. Only numerical simulations are presented in the last two scenarios.

It is found that the lumped element model cannot be verified on the basis of a comparison of the experimental results and the analytical model for the transient state. The analytical model cannot replicate and predict axial vibrations in a vertical drill string.

## Sammendrag

En studie av aksiale vibrasjoner av en vertikal borestreng har blitt utført ved bruk av en fjær-masse-demper-modell med $n$ elementer. Hovedmotivasjonen bak dette er å beskrive de aksiale vibrasjoner ved hjelp av en enkel matematisk modell som resulterer i betydelig tolkning og anvendelse av kontroll teorien. Med noen få justeringer, kan den analytiske modellen som beskriver testsegmenter i denne avhandlingen enkelt implementeres i andre vertikale borestreng modeller. Dette leder oss til å definere følgende problemstilling:

**I hvilken grad kan fjær-masse-demper-modellen benyttes til å gjenskape og forutsi aksielle vibrasjoner i en vertikal borestreng?**

Tre scenarioer ble utformet ved utledning av den analytiske modellen. Det første scenariet evaluerer den transiente tilstanden til modellen, og deles inn i systemene overdempet, kritisk dempet, og underdempet. Dette scenariet omfatter både fysiske eksperimenter så vel som numeriske simuleringer. Resultater fra de fysiske eksperimentene og numeriske simuleringer presenteres grafisk for å identifisere eventuelle likheter mellom de to systemene. Det andre scenariet evaluerer steg respons som den pådrivende kraften. Siste scenariet introduserer en sinusformet drivkraft. Kun resultater fra numeriske simuleringer har blitt presentert for de to siste scenariene.

På basis av sammenligningen mellom de eksperimentelle resultatene og den analytiske modellen for den transiente tilstanden, kan fjær-masse-demper modellen ikke verifiseres. Den analytiske modellen kan ikke presentere en pålitelig replikasjon og predikasjon av aksielle vibrasjoner i en vertikal borestreng.

# Preface

This Master's thesis is written as part of the MSc program in Petroleum Technology, at the Department of Petroleum Engineering and Applied Geophysics at the Norwegian University of Science and Technology (NTNU) in Trondheim, Norway. The work has primarily been done in the laboratory at Petroleum Technology Center at NTNU. This individual thesis is written as part of a team that collaborated during the experimental part of the project.

# Acknowledgements

I would like to thank my supervisor, associate professor Sigve Hovda at the Department of Petroleum Engineering and Applied Geophysics, for guidance throughout the work with the thesis, and for providing theoretical derivations of the model. Thanks also goes to the fellow student Thomas Løklingholm, for his support and cooperation during the experiments, and guidance during the preparation of this thesis. Finally, I would like to thank my family and friends for their encouragement and moral support.

Raz Taha Hassan

Trondheim, June 2016

## Table of Contents

## List of Figures

## List of Tables

# 1 Introduction

Mechanical vibrations in a drill string are the main causes of performance loss and a low rate of penetration (ROP) (Dupriest, 2006). Such mechanical vibrations occur unintentionally during drilling operations. They often have damaging effects on the overall drilling system, resulting in damaged equipment, borehole disruption, and can even cause safety problems (Macpherson et al., 1993). These damaging effects are often associated with economic losses in the drill string system (Márquez et al., 2015: Azar & Samuel, 2007: Dupriest et al., 2010).

Over the last fifty years, extensive research effort has been made on the modeling of drilling systems. Bailey and Finnie of Shell Development Company conducted the first analytical and experimental study on torsional and axial drilling vibrations in 1960 (Bailey & Finnie, 1960). Ever since, multiple methods are recognized to model different types of vibrations in a drill string, as described in chapter 2 in Márquez et al. (2015) and in Ghasemloonia et al. (2015). Márquez et al. (2015) classifies the drill string models into lumped element models, distributed element models, and neutral-type time-delay models. Such models are primarily used to simulate one of the three main types of drill string vibrations, namely axial (bit bouncing), lateral (bending behavior of the drill string) and torsional (stick and slip phenomenon).

Depending on the application, both distributed element models and lumped element models are commonly used. Distributed element models, however, involve solving a set of partial differential equations with boundary and initial conditions (Taylor & Zhu, 2005). In such a system, all dependent variables are functions of time and one or more spatial variables (Bilbao, 2014). Consequently, modelling and simulation of such systems is a highly time-consuming process. Moreover, the mathematical descriptions are only applicable for the specified part of the system. Any change in parameters requires more time-consuming simulations. In contrast, a lumped element model involves solving a set of ordinary differential equations where the dependent variables of interest are functions of time alone.

A spring-mass-damper system is a type of a lumped element model commonly used for describing vibrations in mechanical systems. This thesis investigates axial vibrations in a vertical drill string using a spring-mass-damper model. According to Hovda (2016), the simple mathematical description allows for a substantial interpretation and application of control theory. The study attempts to answer the following research question:

**To what extent can the lumped element model be used to replicate and predict axial vibrations in a vertical drill string?**

The purpose of this thesis is therefore threefold. Firstly, to derive a spring-mass-damper model of a vertical drill string for one and multiple elements. Secondly, to design experiments based on a vertical drill string to measure axial strain (displacement) using strain gauges. Finally, to compare the numerical models and experimental results, in order to be able to draw conclusions about the validity of the analytical model.

This thesis begins with a discussion of a spring-mass-damper model with a single element. The simple model is evaluated for overdamped, critically damped, and underdamped systems. The extension to multiple elements is described in Hovda (2015). According to Hovda (2015), the spatially distributed drill string approximates by a topology of discrete entities, i.e. $n$- coupled spring-mass-damper system. It is based on the assumption that all interactions between the rigid masses is only through springs and dampers. This leads to a system of second-order ordinary differential equations that is presented in a matrix form. Because these equations are coupled, an eigenvalue decomposition is necessary. Chapter 8 in Kreyszig (2006) describes various methods for determining eigenvalues and eigenvectors. By forming a set of decoupled equations, it is possible to solve the system using standard procedures.

Hovda (2015) considers only two scenarios, namely step response and sinusoidal driving forces. This thesis differ from Hovda (2015) by extending the model to a third scenario that considers the transient state of the drill string. Essentially, the model evaluates axial vibrations in a drill string after being subjected to an axial force.

This thesis is laid out as follows: Chapter 2 covers the derivation of a spring-mass-damper model for one and $n$ elements, respectively. Chapter 3 presents general information about strain gauges and technical instrumentation. The theory presented in chapter 3 builds on the work from Hassan (2015). Chapter 4 describes the general setup of the experiments. The experimental results and evaluation are given in chapter 5. Chapter 6 discusses uncertainties and the reliability of the experiments and the analytical model. Concluding remarks are given in chapter 6.

# 2 Dynamic Model of the Drill String

## 2.1 The Drill String as a Single Spring-Mass-Damper Element

Considering a point mass $m$ connected to the end of a weightless spring. The point mass stretches the spring by a length $q_0$ to reach the equilibrium position of the system. At this position, the spring force acting on the point mass and the gravity force acting on the spring is in equilibrium. $q(t)$ represents the displacement of the point mass at time $t$, relative to $q_0$. The piston acts as the viscous damping force, representing the drilling fluid in a borehole. Because of the viscous piston, the velocity decreases in proportion to the acting damping force. **Figure 2.1** illustrates a simple spring-mass-damper model compared to a continuous drill string. Notice that positive direction is downward. The spring is stretched $(q > 0)$ when the movement is below the equilibrium line, and compressed $(q < 0)$ when the movement is above that line.

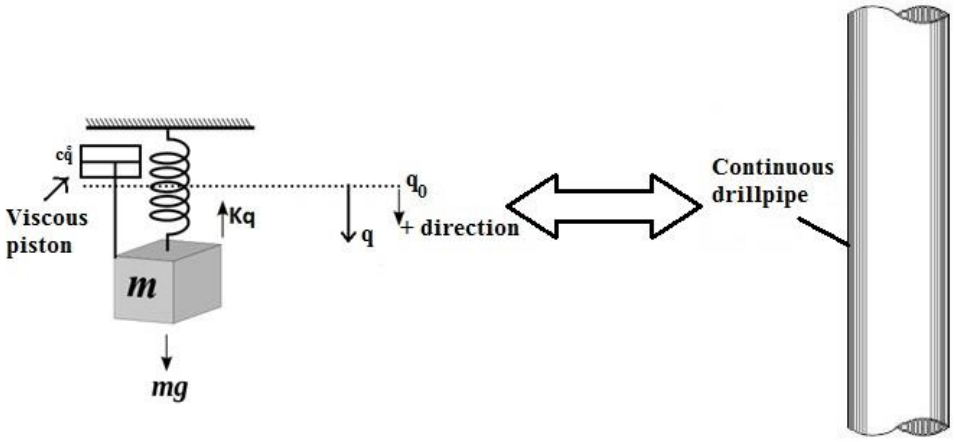


**Figure 2.1:** Left figure shows the damped harmonic oscillator with a point mass $m$ and a spring with a spring constant $k$. The forces acting on the point mass are the gravity force, $mg$, the force from the spring, $kq$, given by Hooke's law, and the viscous piston force, which acts as a damping force, $c\dot{q}$. The right figure illustrates a continuous drillpipe.

In mechanical systems, Hooke's law lays the foundation for the lumped element model. It connects the physical systems of a continuous drillpipe and a spring-mass-damper model together. Hooke's law presents therefore the stress acting on a drillpipe and the spring force acting on a point mass, respectively (**figure 2.1**):

$$\sigma = E\varepsilon \text{ and } F_s = k\Delta L.$$

$E$ is modulus of elasticity of the material (Young's modulus), $\varepsilon$ is strain, $k$ is the spring constant, and $\Delta L$ is displacement of the spring. Because both systems is assumed equal, the force acting on both of them must also be equal, i.e.:

$$\sigma = \frac{F}{A_c} = \frac{k\Delta L}{A_c} = E\varepsilon = E\frac{\Delta L}{L} \Leftrightarrow k = \frac{EA_c}{L}. \tag{2.1}$$

The lumped element model makes it possible to solve the system of a spring-mass-damper model using ordinary differential equations, which simplify the process of finding an analytical solution. Therefore, applying Newton's second law on the system implies

$$m\ddot{q} = -kq - c\dot{q} + mg \Leftrightarrow \ddot{q} + \frac{c}{m}\dot{q} + \frac{k}{m}q - g = 0. \tag{2.2}$$

A coordinate transformation from $q$ to $x$ eliminates the $g$-term and simplifies equation (2.2) (Hassan, 2015):

$$q = x + \frac{m}{k}g \Leftrightarrow \dot{q} = \dot{x} \Leftrightarrow \ddot{q} = \ddot{x} \tag{2.3}$$

The transformation also improves the equation by giving it a more realistic view, i.e. at no tension $x(0) = 0$ instead of $q(0) = 0,$ which is physically unrealistic. This statement is proven by the fact that when $q(0) = 0,$ equation (2.3) results in $q(0) = mg/k.$ Hence, even at equilibrium the system is under the influence of gravity. The result of the coordinate transformation is therefore:

$$\ddot{x} + 2\varsigma\omega_0\dot{x} + \omega_0{}^2 x = 0, \tag{2.4}$$

where

$$\omega_0 = \sqrt{\frac{k}{m}} \quad \text{and} \quad \varsigma = \frac{c}{2\sqrt{mk}}. \tag{2.5}$$

$\omega_0$ is the natural frequency of the system, which is the frequency of an undamped harmonic oscillator. $\varsigma$ is the damping ratio of the system (Tseng, 2008).

The characteristic equation of the second-order differential equation (2.4) can be formed:

$$r^2 + 2\varsigma\omega_0 r + \omega_0{}^2 = 0.$$

The roots of the characteristic equation are (Chu et al., 2011):

$$r = -\varsigma\omega_0 \pm \omega_0\sqrt{\varsigma^2 - 1}. \tag{2.6}$$

Equation (2.6) provides three possible solutions, depending on the damping ratio, $\varsigma$, which determines the behavior of the system.

### 2.1.1 Overdamped System $(\varsigma > 1)$

When $\varsigma > 1$, equation (2.6) provides two distinct real roots, $r = -\varsigma\omega_0 \pm \omega_0\sqrt{\varsigma^2 - 1}$, which form the solution (Tseng, 2008):

$$x(t) = C_1 e^{r_1 t} + C_2 e^{r_2 t} = C_1 e^{\left(-\varsigma - \sqrt{\varsigma^2 - 1}\right)\omega_0 t} + C_2 e^{\left(-\varsigma + \sqrt{\varsigma^2 - 1}\right)\omega_0 t}, \tag{2.7}$$

where constants $C_1$ and $C_2$ can be determined by the initial conditions.

### 2.1.2 Critically Damped System $(\varsigma = 1)$

When $\varsigma = 1$, equation (2.6) provides one real root, $r = -\varsigma\omega_0$, forming the solution (Tseng, 2008):

$$x(t) = C_1 e^{rt} + C_2 t e^{rt} = C_1 e^{-\varsigma\omega_0 t} + C_2 t e^{-\varsigma\omega_0 t}. \tag{2.8}$$

Similar to case I, the initial conditions determines the constants $C_1$ and $C_2$.

### 2.1.3 Underdamped System $(\varsigma < 1)$

When $\varsigma < 1$, equation (2.6) provides two complex roots, i.e. $r = -\varsigma\omega_0 \pm \omega_0\sqrt{\varsigma^2 - 1}$. This gives the following solution of the system (Tseng, 2008; Morin, 2015):

$$x(t) = e^{-\varsigma\omega_0 t}\left(C_1 \cos(\omega_d t) + C_2 \sin(\omega_d t)\right) \Leftrightarrow x(t) = A e^{-\varsigma\omega_0 t} \sin(\omega_d t + \phi). \tag{2.9}$$

$\omega_d = \omega_0\sqrt{1 - \varsigma^2}$ is the damped angular frequency of the system, $A$ is the amplitude, and $\phi$ is the phase shift.

## 2.2 The Drill String as $n$-Coupled Spring-Mass-Damper Elements

The system of one spring-mass-damper element describes the fundamental idea behind the lumped element model. However, in order to derive a proper analytical model, we need to generalize the system into $n$-point masses connected to $n$-spring elements. **Figure 2.2** illustrates such system. The springs are free to rotate with respect to the point masses, meaning that each spring cannot take up angular momentum. A one-dimensional coordinate system is introduced, where origin is at position $Q$, representing the rig deck. The first point mass has coordinates $q_1(t)$, the second one $q_2(t)$, and so on. $q_i(t)$ represents the distance between the center point on each point mass to the point where the spring is neither compressed or in tension. Hence, the generalized coordinates, $q_i(t)$, uniquely defines the position of each element in the drill string at time $t$ (Hovda, 2015).

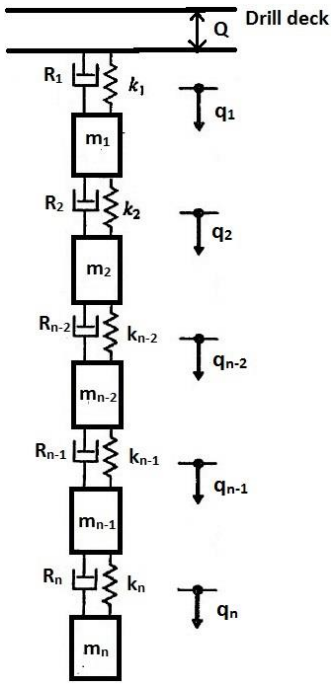


**Figure 2.2:** $n$-coupled spring-mass-damper model. $R$ represents the viscous friction force acting on the opposite direction of the displacement. Positive direction on the one-dimensional coordinate system is downward in $q$-direction.

The Newton's second law on each element is given by

$$0=\begin{cases}-m_i\ddot{q}_i+m_1g\beta-k_1(q_1-Q)+k_2(q_2-q_1)-R_1 & \text{for element } i=1\\ -m_i\ddot{q}_i+m_ig\beta-k_i(q_i-q_{i-1})+k_{i+1}(q_{i+1}-q_i)-R_i & \text{for element } 2\le i\le n-1\\ -m_n\ddot{q}_n+m_ng\beta-k_n(q_n-q_{n-1})-R_n & \text{for element } i=n\end{cases} \tag{2.10}$$

where $m_i$ is the mass of element $i$ and $k_i$ is the spring constant of the spring that is connected above point mass $i$. The buoyancy factor, $\beta$, is introduced to simulate the drill fluid in a typical borehole. The external force, $R_i$, is equivalent with the viscous friction force, as known from section (2.1).

Evidently, equation (2.10) is a system of $n$-coupled second order ordinary differential equations. Therefore, it can be written on matrix form as

$$\mathbf{M}\ddot{q} + \mathbf{C}\dot{q} + \mathbf{K}q = \mathbf{g} + \mathbf{f}(t), \tag{2.11}$$

where $\mathbf{M}$ and $\mathbf{C}$ is given by $m\mathbf{I}$ and $c\mathbf{I}$, respectively. The $\mathbf{C}$ matrix is determined from the relation $c_i = R_i / \dot{q}_i$. $\mathbf{g}$ is a vector with elements $m_i g \beta$, and $\mathbf{K}$ is a tridiagonal matrix of the form

$$\mathbf{K} = \begin{bmatrix} k_1 + k_2 & -k_2 & 0 & \cdots & 0 & 0 & 0 \\ -k_2 & k_2 + k_3 & -k_3 & \cdots & 0 & 0 & 0 \\ 0 & -k_3 & k_3 + k_4 & \cdots & 0 & 0 & 0 \\ \vdots & \vdots & \vdots & \ddots & \vdots & \vdots & \vdots \\ 0 & 0 & 0 & \cdots & k_{n-2} + k_{n-1} & -k_{n-1} & 0 \\ 0 & 0 & 0 & \cdots & -k_{n-1} & k_{n-1} + k_n & -k_n \\ 0 & 0 & 0 & \cdots & 0 & -k_n & k_n \end{bmatrix}.$$

$\mathbf{f}(t)$ is a vector with first element $-k_1 Q(t)$, and the others are zero. Because of the $Q(t)$, $f_1(t)$ is known as the driving force of the system.

It is necessary to make a coordinate transformation, similar to section 2.1, before further evaluation of equation (2.11), using the expression:

$$\mathbf{y} = \mathbf{q} + \mathbf{K}^{-1}\mathbf{g} \Leftrightarrow \dot{\mathbf{y}} = \dot{\mathbf{q}} \Leftrightarrow \ddot{\mathbf{y}} = \ddot{\mathbf{q}}.$$

It is possible to show that the inverse of $\mathbf{K}$ is given by

$$\mathbf{K}^{-1} = \sum_{i=1}^{n} \mathbf{K}_i \quad \text{where} \quad \mathbf{K}_i = \begin{bmatrix} \mathbf{0}_{i-1,i-1} & \mathbf{0}_{i-1,n+1-i} \\ \mathbf{0}_{n+1-i,i-1} & K_i^{-1}\mathbf{1}_{n+1-i,n+1-i} \end{bmatrix},$$

which is described in more details in Hovda (2015).

Obviously, $\mathbf{0}_{u,v}$ and $\mathbf{1}_{u,v}$ are $u$-by-$v$ matrices with zeroes and ones, respectively. Moreover, $\mathbf{K_i g}$ is a vector with zeros on the $i-1$ first elements, and rest of the elements have the value $k_i^{-1} gB\sum_{j=i}^{n} m_j$. According to Hovda (2015), this value is the same as the displacement of spring $i$ from its equilibrium position. Because of $\mathbf{K^{-1}}g = \sum_{i=1}^{n} \mathbf{K}_i g$, the coordinate transformation means that every $y_i$ is zero when all the elements are hanging at the equilibrium position. Hence, the coordinate transformation gives the model a more realistic view because of $y_i(0) = K_i^{-1} g$ instead of $q_i(0) = 0$, which means that the springs are not in tension or in compression. The last statement is only true for a massless drill string, i.e. $y_i = q_i$. The coordinate transformation results in:

$$\mathbf{M}\ddot{\mathbf{y}} + \mathbf{C}\dot{\mathbf{y}} + \mathbf{K}\mathbf{y} = \mathbf{f}(t). \tag{2.12}$$

The process of decoupling the equations in (2.12) depends highly on the tridiagonal matrix $\mathbf{K}$. If $\mathbf{K}$ is a diagonal matrix, no further procedures are required to decouple the equations and solve them separately. However, there is a procedure to decouple (2.12). Since both $\mathbf{M}$ and $\mathbf{K}$ are real symmetric and positive definite (i.e. $\mathbf{v}^T\mathbf{M}\mathbf{v} > 0$ and $\mathbf{v}^T\mathbf{K}\mathbf{v} > 0$ for any nonzero and real column vector $\mathbf{v}$), then ($\mathbf{M}$, $\mathbf{K}$) is a real definite pair (Hovda, 2016). Hence, the generalized eigenvalue problem

$$\mathbf{M}\mathbf{v} = \lambda\mathbf{K}\mathbf{v} \quad \text{where} \quad \mathbf{V}^T\mathbf{M}\mathbf{V} = \mathbf{I} \quad \text{and} \quad \mathbf{V}^T\mathbf{K}\mathbf{V} = \mathbf{D}$$

leads to a matrix of eigenvectors, $\mathbf{V}$, and a diagonal matrix $\mathbf{D}$ of eigenvalues, where $\mathbf{I}$ is the identity vector. Introducing the second coordinate transformation expressed as

$$\mathbf{y} = \mathbf{V}x \Leftrightarrow \dot{\mathbf{y}} = \mathbf{V}\dot{x} \Leftrightarrow \ddot{\mathbf{y}} = \mathbf{V}\ddot{x},$$

which leads to

$$\ddot{x} + \mathbf{V}^T C\mathbf{V}\dot{x} + \mathbf{D}x = \mathbf{V}^T\mathbf{f}(t). \tag{2.13}$$

Notice that equation (2.13) is multiplied by the transpose matrix of the eigenvectors, $\mathbf{V}^T$.

Obviously, the system is still coupled since $\mathbf{V}^T C\mathbf{V}$ is not diagonal. According to Hovda (2015), it is a fair approximation to assume that $\mathbf{C} = c\mathbf{M}$ where $c$ is a constant. If the bottom hole assembly (BHA) is short compared to the drillpipe, it is fair to assume that $c = c_1 / m_1$. This means that the BHA affects the damping ratio at a higher degree than what is real. The final set of uncoupled equations are therefore:

$$\ddot{x}_i + 2\varsigma_i \omega_i \dot{x}_i + \omega_i^2 x_i = -V_{1i} k_1 Q(t), \tag{2.14}$$

where $\omega_i = \sqrt{D_{ii}}$, $\varsigma_i = c/2\omega_i$, and $V_{1i}$ is the $i$-th element of the first eigenvector.

The general solution of equation (2.14) consist of an ordinary solution, also known as the transient solution, and a particular solution, known as the steady state solution.

$$x_i(t) = x_{o,i}(t) + x_{p,i}(t)$$

Considering three main scenarios:

1. The transient state of the system, i.e. $x_i(t) = x_{o,i}(t)$. The initial conditions are selected so that $x_i(0) = Q_i$ and $x_i'(0) = 0$, where $Q_i = k_i^{-1} w_i$ is the initial displacement caused by a specific mass loaded on the system. $k_i^{-1}$ is the inverse matrix of the spring constant and $w_i$ is the gravitational force caused by the loaded mass. It is important to notice that the initial conditions converted to a $n \times 1$ vector are given by $\mathbf{x}(0) = \mathbf{Q}$, where $\mathbf{Q} = \mathbf{k}^{-1}\mathbf{w}$. The $n \times 1$ vector, $\mathbf{w}$, consist of zeros except the $n-1$ element, i.e. the element where the mass is loaded.
2. The step response as the driving force, i.e.

$$Q(t) = \begin{cases} 0 & for\ t < 0 \\ Q_s & for\ t \geq 0. \end{cases}$$

   $Q_s$ is the initial displacement of the first element as a result of the step. Moreover, the initial conditions are defined as $x_i(0) = 0$ and $\dot{x}_i(0) = 0$.

3. A sinusoidal driving force, i.e. $Q(t) = Q_d \sin(\omega t)$.

Before discussing the three scenarios, it is important to derive an expression for the viscous friction force, $R_i$, so that the damping ratio can be determined.

### 2.2.1 The Viscous Friction Force

The viscous friction force acts in opposite direction of the movement of the drill string. $R_i$ is the viscous force acting on element $i$ of the drill string. **Figure 2.3** illustrates a moving drill string when POOH. The velocity profile of the drill mud shows the impact of the moving drill string. The velocity of the drill mud is higher between the drill collar and the borehole wall because the distance is smaller, i.e. $(R_{hole} - \alpha_p R_{hole}) < (R_{hole} - \alpha_c R_{hole})$. Hence, the force acting on the drill collar is larger than the one acting on the drillpipe.

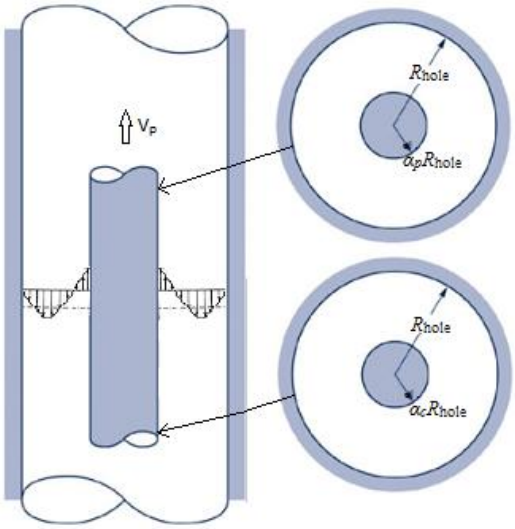


**Figure 2.3:** The viscous forces acting on the drillpipe and the drill collar when POOH. $R_{hole}$ is the radius of the borehole, $\alpha_p R_{hole}$ and $\alpha_c R_{hole}$ are radiuses of the drillpipe and drill the collar, respectively.

In order to derive a useful equation for the viscous friction force, it is necessary to generate the following assumptions, where we assume that

- the mud pump is turned off and no circulation in the mud.
- the fluid is Newtonian, i.e. $\tau_w = -\mu \left. \frac{\delta v}{\delta r} \right|_{\alpha R_{hole}}$
- the flow is laminar, steady and axial symmetric
- the flow component is only parallel to the movement of the drillpipe, i.e. no flow in horizontal plane (**figure 2.3**).

- no slip condition at the wellbore wall, $r = R_{hole}$, so that $u_i\left(R_{hole}\right) = 0$. In annulus, no slip condition on inner pipe as well, i.e. $u_i\left(\alpha_i R_{hole}\right) = \dot{q}_i$, where $\alpha_i R_{hole}$ is the outer radius of the drill string and $\dot{q}_i$ is the velocity of the drill string ($v_p$ in **figure 2.3**).

The viscous friction force acting on element $i$ with length $L_i$ is expressed as

$$R_i = -2\pi R_{hole} L_i \mu \left.\frac{\partial u_i}{\partial r}\right|_{\alpha_i R_{\text{hole}}}$$

The final equation for $R_i$ is derived in appendix **A**, and expresses as

$$R_i = -2\pi L_i \mu \dot{q}_i \left( \frac{2\left(1-\alpha_i^2\right)^2 + \left(\alpha_i^2 - \alpha_n^2\right)^2 - \left(1-\alpha_n^2\right)^2 - 4\alpha_i^2\left(\alpha_i^2 - \alpha_n^2\right)^2 \ln\left(\alpha_i\right)}{\left(1-\alpha_i^4\right)\ln\left(\alpha_i\right) + \left(1-\alpha_i^2\right)^2} \right), \tag{2.15}$$

where $\alpha_i$ is the ratio of the outer radius of the drillpipe and the borehole radius, i.e. $\alpha_i = r_p / R_{hole}$, and $\alpha_n$ is the ratio of the outer radius of the drill collar and the borehole radius, i.e. $\alpha_n = r_c / R_{hole}$. $\dot{q}_i$ is velocity of the drill string at element $i$.

### 2.2.2 Scenario 1: The Transient State

When only considering the transient state of the system, will equation (2.14) converts to

$$\ddot{x}_i + 2\varsigma_i \omega_i \dot{x}_i + \omega_i^2 x_i = 0. \tag{2.16}$$

Clearly, this will give the same homogeneous solutions as described in section 2.1, but for $n$ elements. The characteristic equation of (2.16) gives three possible solutions, depending on the damping ratio, $\varsigma_i$.

#### 2.2.2.1 Overdamped System $\left(\varsigma_i > 1\right)$

Modifying equation (2.7) from section 2.1.1:

$$x_i(t) = C_{1,i} e^{\left(-\varsigma_i - \sqrt{\varsigma_i^2 - 1}\right)\omega_i t} + C_{2,i} e^{\left(-\varsigma_i + \sqrt{\varsigma_i^2 - 1}\right)\omega_i t} = C_{1,i} e^{\gamma_{i,1} t} + C_{2,i} e^{\gamma_{i,2} t}$$

where $\gamma_{i,1} = -\varsigma_i \omega_i - \omega_i \sqrt{\varsigma_i^2 - 1}$ and $\gamma_{i,2} = -\varsigma_i \omega_i + \omega_i \sqrt{\varsigma_i^2 - 1}$. By implementing the initial conditions $x_i(0) = Q_i$ and $x_i'(0) = 0$, we get the following equation:

$$x_i(t) = \frac{Q_i}{\gamma_{i,2} - \gamma_{i,1}}\left(\gamma_{i,2}e^{\gamma_{i,1}t} - \gamma_{i,1}e^{\gamma_{i,2}t}\right), \tag{2.17}$$

where $C_{1,i} = \dfrac{Q_i\gamma_{i,2}}{\gamma_{i,2} - \gamma_{i,1}}$ and $C_{2,i} = -\dfrac{Q_i\gamma_{i,1}}{\gamma_{i,2} - \gamma_{i,1}}$.

The system in equation (2.17) will not oscillate because it represents the overdamped system, which is obvious because it lacks a complex term in the exponentials. It is worth noting that each element will cross its equilibrium line maximum once.

It is necessary to obtain the solution in the original or the physical coordinate system, i.e.

$$\mathbf{Y} = \mathbf{Vx},$$

where $\mathbf{V}$ is a matrix of eigenvectors. Again, by applying the initial conditions in the coordinate system, it is possible to determine the new initial displacement of the $\mathbf{x}$ matrix. Evidently, it is known that

$$\mathbf{Y}(0) = \mathbf{Vx}(0) = \mathbf{Q} \text{ which implies } \mathbf{x}(0) = \mathbf{C}_{\mathbf{I.C.}} = \mathbf{V}^{-1}\mathbf{Q} = \mathbf{V}^{-1}\mathbf{k}^{-1}\mathbf{w}, \tag{2.18}$$

where $\mathbf{C}_{\mathbf{I.C.}}$ is the initial condition vector. Using the fact that

$$y_j(t) = \sum_{i=1}^{n} V_{ji}x_i(t)$$

to superposition the modal solutions. Hence

$$y_j(t) = \sum_{i=1}^{n} \frac{V_{ji}C_{I.C.,i}}{\gamma_{i,2} - \gamma_{i,1}}\left(\gamma_{i,2}e^{\gamma_{i,1}t} - \gamma_{i,1}e^{\gamma_{i,2}t}\right). \tag{2.19}$$

#### 2.2.2.2 Critically Damped System $(\varsigma_i = 1)$

Recalling equation (2.8) from section 2.1.2, modified to element $i$:

$$x_i(t) = C_{1,i}e^{-\varsigma_i\omega_i t} + C_{2,i}te^{-\varsigma_i\omega_i t}.$$

Similar to the overdamped system, implementing the initial conditions $x_i(0) = Q_i$ and $x_i'(0) = 0$ to determine constants $C_{1,i}$ and $C_{2,i}$. The final equation is therefore

$$x_i(t) = Q_i e^{-\varsigma_i\omega_i t}\left(1 - \varsigma_i\omega_i t\right),$$

where $C_{1,i} = Q_i$ and $C_{2,i} = -Q_i\varsigma_i\omega_i$.

Since this is a critically damped system, the elements returns to its equilibrium position as quickly as possible without oscillating. However, each element could cross its equilibrium line maximum once, just like the overdamped system.

Similar to the overdamped system, it is necessary to obtain the solution in the original or the physical coordinate system. Therefore:

$$y_j(t) = \sum_{i=1}^{n} V_{ji} C_{I.C.,i} e^{-\varsigma_i \omega_i t} (1 - \varsigma_i \omega_i t). \tag{2.20}$$

Notice that the initial condition, $C_{I.C.,i}$, derived in section 2.2.2.1 has been implemented in the equation.

### 2.2.2.3 Underdamped System $(\varsigma_i < 1)$

Recalling equation (2.9) from section 2.1.3, modified to element $i$:

$$x_i(t) = A_i e^{-\frac{c}{2}t} \sin(\omega_{d,i} t + \phi_i).$$

Implementing the initial conditions $x_i(0) = Q_i$ and $x_i'(0) = 0$ to determine the amplitude $A_i$ and the phase shift $\phi_i$, which gives the following equation:

$$x_i(t) = \frac{Q_i e^{-\frac{c}{2}t}}{\sin(\phi_i)} \sin(\omega_{d,i} t + \phi_i),$$

where $A_i = \dfrac{Q_i}{\sin(\phi_i)}$ and $\phi_i = \arctan\left(\dfrac{\sqrt{1-\varsigma_i^2}}{\varsigma_i}\right)$.

Again, the superposition of modal solutions results in the equation:

$$y_j(t) = e^{-\frac{c}{2}t} \sum_{i=1}^{n} \frac{V_{ji} C_{I.C.,i}}{\sin(\phi_i)} \sin(\omega_{d,i} t + \phi_i). \tag{2.21}$$

Notice that the initial condition, $C_{I.C.,i}$, derived in section 2.2.2.1 has been implemented to the equation.

### 2.2.3 Scenario 2: Step Response as the Driving Force

Recalling equation (2.14):

$$\ddot{x}_i + 2\zeta_i \omega_i \dot{x}_i + \omega_i^2 x_i = -V_{1i} k_1 Q(t),$$

where $Q(t)$ is the displacement of the elements at time $t = 0$ denoted to the step response, given as:

$$Q(t) = \begin{cases} 0 & for\ t < 0 \\ Q_s & for\ t \geq 0. \end{cases}$$

At $t = 0,$ the element is moved to $Q_s$, assuming this happens momentarily, i.e. $\ddot{x} \approx \infty.$ At steady state, i.e. when $t \to \infty,$ the statements $y = \dot{y} = x = \dot{x} = 0$ are valid. These initial conditions imply that all amplitudes are zero, $A_i = 0.$

The transient solution of the system, assuming underdamped, is given as:

$$x_{o,i}(t) = A_i e^{-\frac{c}{2}t} \sin\left(\omega_{d,i} t + \phi_i\right).$$

The particular solution is found by investigating the right-hand side of equation (2.14), which is the constant $-V_{1i} k_1 Q_s$. Hence, we search for a particular solution of the form

$$x_{\mathrm{p},i}(t) = K_i \Rightarrow \dot{x}_{\mathrm{p},i}(t) = 0 \Rightarrow \ddot{x}_{\mathrm{p},i}(t) = 0,$$

where $K_i$ is an arbitrary constant. By inserting the expressions of $x_{\mathrm{p},i}$ into the differential equation, one can find that

$$x_{\mathrm{p},i}(t) = -\frac{V_{1i} k_1 Q_s}{\omega_i^2}.$$

The general solution of the system is determined by a superposition of the homogeneous solution and the particular solution, i.e.:

$$x_i(t) = x_{o,i}(t) + x_{\mathrm{p},i}(t) = A_i e^{-\frac{c}{2}t} \sin\left(\omega_{d,i} t + \phi_i\right) - \frac{V_{1i} k_1 Q_s}{\omega_i^2}.$$

The amplitude $A_i$ and the phase shift $\phi_i$ are determined by the initial conditions $x_i(0) = 0$ and $\dot{x}_i(0) = 0,$ which leads to:

$$A_i = -\frac{V_{1i} k_1 Q_s}{\omega_i^2 \sin(\phi_i)} \text{ and } \frac{\sin(\phi_i)}{\cos(\phi_i)} = \frac{\sqrt{1-\varsigma_i^2}}{\varsigma_i} \Leftrightarrow \sin(\phi_i) = \sqrt{1-\varsigma_i^2} \ \& \ \cos(\phi_i) = \varsigma_i.$$

The general solution is therefore:

$$x_i(t) = \begin{cases} 0 & \text{for } t < 0 \\ -\frac{V_{1i} k_1 Q_s}{\omega_i^2} \left( 1 - \frac{\mathrm{e}^{-\frac{c}{2}t}}{\sqrt{1-\varsigma_i^2}} \sin\left(\omega_{d,i} t + \phi_i\right) \right) & \text{for } t \geq 0. \end{cases}$$

Similar to the previous sections, it is necessary to obtain the solution in the original or the physical coordinate system. Hence

$$y_j(t) = \begin{cases} 0 & \text{for } t < 0 \\ -k_1 Q_s \sum_{i=1}^{n} \left[ \frac{V_{ji} V_{1i}}{\omega_i^2} \left( 1 - \frac{\mathrm{e}^{-\frac{c}{2}t}}{\sqrt{1-\varsigma_i^2}} \sin\left(\omega_{d,i} t + \phi_i\right) \right) \right] & \text{for } t \geq 0 \end{cases}$$

According to Hovda (2016), the fact that $\mathbf{K}^{-1} = \mathbf{V}^T \mathbf{D}^{-1} \mathbf{V}$ implies $\sum_{i=1}^{n} \frac{V_{ji} V_{1i}}{\omega_i^2} = \left(\mathbf{K}^{-1}\right)_{j1} = -k_1^{-1}$, which leads to the final solution:

$$y_j(t) = \begin{cases} 0 & \text{for } t < 0 \\ Q_s - Q_s \, \mathrm{e}^{-\frac{c}{2}t} \sum_{i=1}^{n} \frac{k_1 V_{ji} V_{1i}}{\omega_i^2 \sqrt{1-\varsigma_i^2}} \sin\left(\omega_{d,i} t + \phi_i\right) & \text{for } t \geq 0. \end{cases} \tag{2.22}$$

### 2.2.4 Scenario 3: Sinusoidal Driving Force

In the case of sinusoidal driving force, i.e. $Q(t) = Q_d \sin(\omega t)$, equation (2.14) converts to

$$\ddot{x}_i + 2\varsigma_i \omega_i \dot{x}_i + \omega_i^2 x_i = -V_{1i} k_1 Q_d \sin(\omega t), \tag{2.23}$$

where $Q_d$ is a constant that characterize the strength of the driving force, and $\omega$ is its angular frequency.

The system starts at rest in its initial position and the transient solution is therefore zero. Hence, the general solution consists only of the steady state solution. Evidently, the steady state solution is of the form

$$x_i(t) = A_i \sin(\omega t + \psi_i), \tag{2.24}$$

where $A_i$ is a constant and $\psi_i$ is an induced phase shift relative to the driving force. When equation (2.24) is substituted into equation (2.23), it is found to satisfy that equation only when

$$A_i = \frac{V_{1i} k_1 Q_d}{\sqrt{\omega^2 c^2 + \left(\omega_i^2 - \omega^2\right)^2}} \text{ and } \psi_i = \arctan\left(\frac{c\omega}{\omega^2 - \omega_i^2}\right).$$

The derivation of these results are given in appendix **B**. The solution to the steady state is therefore:

$$x_i(t) = \frac{V_{1i} k_1 Q_d}{\sqrt{\omega^2 c^2 + \left(\omega_i^2 - \omega^2\right)^2}} \sin(\omega t + \psi_i).$$

Similar to previous sections, it is necessary to obtain the solution in the original or the physical coordinate system, i.e.:

$$\mathbf{Y} = \mathbf{V}\mathbf{x}(t) \Leftrightarrow y_j(t) = \sum_{i=1}^{n} V_{ji} x_i(t).$$

The superposition of modal solutions is therefore:

$$y_j(t) = \sum_{i=1}^{n} \Psi_{ij} \sin(\omega t + \psi_i),$$

where

$$\Psi_{ij} = \frac{V_{ji} V_{1i} k_1 Q_d}{\sqrt{\omega^2 c^2 + \left(\omega_i^2 - \omega^2\right)^2}}.$$

Because all the sinusoids have the same frequency, they can be added together in this way (Hovda, 2015; Smyth, 2015):

$$y_j(t) = \Gamma_j \sin(\omega t + \gamma_j), \tag{2.25}$$

where

$$\Gamma_j = \sqrt{\sum_{i=1}^{n}\sum_{k=1}^{n} \Psi_{ij}\Psi_{kj} \cos(\psi_i - \psi_k)} \quad \text{and} \quad \gamma_j = \arctan\left(\frac{\sum_i \Psi_{ij} \sin(\psi_i)}{\sum_i \Psi_{ij} \cos(\psi_i)}\right) \tag{2.26}$$

# 3 Strain Gauges as a Tool of Strain Measurements

Strain gauges are electrical devices used to measure strain on solid bodies. This chapter consists of four sections and presents all technical aspects of strain gauges as a tool for strain measurements. The first section provides general information about strain gauges and strain. The second section explains the system structure of strain gauges, which consists of different bridge circuits and their applications. The third section explains noise control and methods to mitigate error by reducing electrical noise that affects the system. The last section provides information of methods for calibrating strain gauge systems.

## 3.1 Strain Gauges

A strain gauge measures microscopic changes in position, usually measured in $\mu m$. The electrical resistance of the device varies proportional to the amount of strain in the device, and is due to a solid body is stretched, twisted or compressed. Hence, strain that the device measures is defined as the amount of deformation a solid body undergoes due to an applied force, or the fractional change in length, as shown in **figure 3.1**.

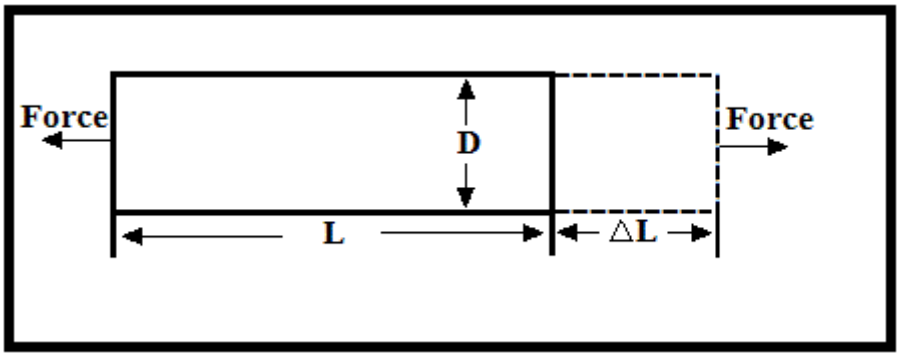


**Figure 3.1:** The definition of strain. A solid body undergoes deformation due to an applied force, where $\Delta L$ represents the amount of deformation parallel to the applied force. (NI, 2014)

Mathematically, strain defines as

$$\varepsilon = \frac{\Delta L}{L} = \frac{\sigma}{E}, \tag{3.1}$$

where $\sigma$ is the stress acting on the cross sectional area of a solid body and $E$ is the modulus of elasticity of the material. The magnitude of strain depends therefore on the Young's modulus of the material, and the magnitude of the applied force. According to equation (3.1), when a solid body undergoes a tensile force, the magnitude of the strain will be positive. However, if the force is compressive, the magnitude of the strain will be negative.

When the material in **figure 3.1** undergoes strain, a phenomenon known as Poisson strain occurs. This phenomenon causes the thinning of the material by making the girth of the material, $D$, to contract in the transverse direction. Therefore, the Poisson's ratio of the material determines the magnitude of this transverse contraction. Poisson's ratio, $\nu$, is defined as the negative ratio of the strain in the transverse direction, to the strain in the axial direction, i.e. (NI, 2014):

$$\nu = -\frac{\varepsilon_T}{\varepsilon}, \tag{3.2}$$

where $\varepsilon_T$ is strain in the transverse direction (perpendicular to the applied force).

There exist several types of strain gauges used for different purposes. Most commonly used are bonded metallic strain gauges, which is illustrated in **figure 3.2**. The bonded metallic strain gauge consists of a metallic foil arranged in a grid pattern. This will maximize the amount of metallic foil subjected to strain in the parallel direction of the applied force. At the same time, the effect of Poisson's strain and shear strain is minimized by keeping the cross sectional area of the grid as small as possible. The grid is embedded in a carrier sheet of plastic or rubber, and must be attached directly to the test body, so that the grid pattern is parallel to the direction of the applied force. The strain gauge will then respond with a linear change in the electrical resistance (NI, 2014). In order to avoid uncertainties and inaccuracies in the measurements, it is important to mount the device correctly and according to its regulations on the test specimen.

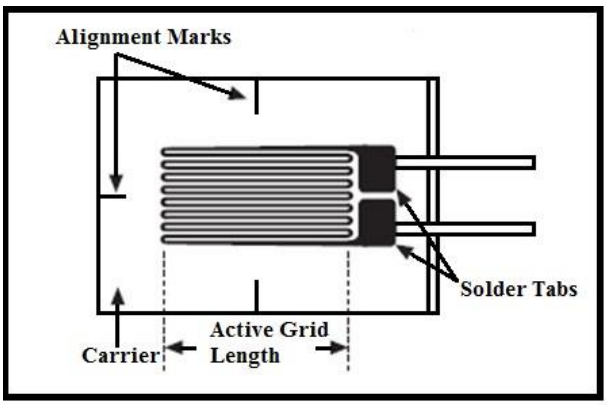


**Figure 3.2:** Bonded metallic strain gauge. The metallic foil is arranged in a grid pattern to maximize the area of the foil that is subjected to strain. (SEESL, 2015)

The nominal resistance of strain gauges varies from 30 to 3000 Ω. High nominal resistance provides high resistance changes, which means higher sensitivity. The problem with high resistance devices is that they are easily worn out and the probability of damaging the device

during the experiments is high. Since our system requires both high resolution of the measurements and high threshold for wear, it will be wise to choose a strain gauge with low resistance. Increasing the resolution of the measurement system will compensate for this. The strain gauges used in the experiments have a nominal resistance of $120\ \Omega$.

Gage Factor, GF, is a quantitative constant that expresses the sensitivity of the gauges. According to NI (2014), the gage factor is defined as the ratio of the fractional change in electrical resistance to the fractional change in length, as shown in equation (3.3).

$$\mathrm{GF} = \frac{\left(\frac{\Delta R}{R}\right)}{\left(\frac{\Delta L}{L}\right)} = \frac{\Delta R}{\varepsilon R} \tag{3.3}$$

## 3.2 System Structure of Strain Gauges

Generally, strain gauges measure no more than a few millistrain ($\varepsilon \times 10^{-3}$). Therefore, it requires accurate measurement tools to detect such small resistance changes. Consider the following scenario; if a test body undergoes a strain of 1 millistrain, will a strain gauge with $\mathrm{GF} = 2$ experience a resistance change of $2 \times \left(1 \times 10^{-3}\right) = 0.2\ \%$. If the nominal resistance of the strain gauge is $120\ \Omega$, will the change only be $0.24\ \Omega$. Therefore, in order to measure such small changes the strain gauges are arranged in a so-called Wheatstone bridge. **Figure 3.3** illustrates the general Wheatstone bridge, which consists of four resistance points and an excitation voltage, $V_{\mathrm{Ex}}$, that is applied across the bridge.

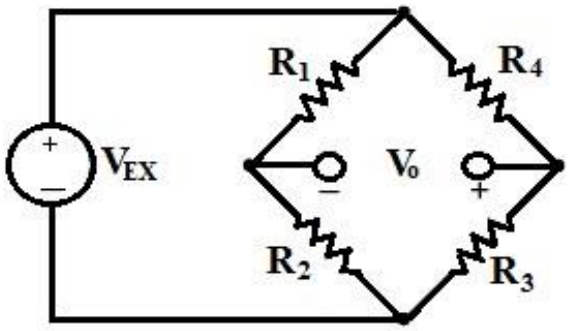


**Figure 3.3:** The Wheatstone bridge. $R_1 - R_4$ represents the resistors, $V_O$ is the output voltage, and $V_{\text{EX}}$ is the excitation voltage. (NI, 2014)

The output voltage, $V_O$, measures the voltage at the intersection point between $R_1$ and $R_2$, relative to the intersection point of $R_3$ and $R_4$. In order for $V_O$ to change in value, it requires a change in resistance. Applying Kirchhoff's law at both intersection points gives the following equations:

$$V_{R_2} = V_{\text{EX}} \frac{R_2}{R_1 + R_2} \quad \text{and} \quad V_{R_3} = V_{\text{EX}} \frac{R_3}{R_3 + R_4}.$$

Combining these equations gives the formula for the output voltage:

$$V_O = V_{R_3} - V_{R_2} = V_{\text{EX}} \left( \frac{R_3}{R_3 + R_4} - \frac{R_2}{R_1 + R_2} \right). \tag{3.4}$$

When the bridge is balanced, the system is not strained and the relation between those two intersection points in **figure 3.3** are $R_1 / R_2 = R_4 / R_3$. The output voltage in equation (3.4) will then be zero. In an ideal, physical system, such offset voltage is always zero, but because of small differences in resistance and other factors that affects the system, the offset voltage is never zero. In addition, any changes in resistance in any arm of the bridge will lead to a nonzero output voltage.

In most cases, a Wheatstone bridge controls a strain gauge system. Such bridge is designed to measure the difference in resistance of voltage change. The bridge consists of four resistors, a power source and a voltmeter. The voltmeter often includes an analog to digital converter to convert the signals to stable, digital outputs. It is important to point out that electrical noise easily affects the analog signal. Good connections, shielding and soldering are key elements in order to make such system work properly.

For the system in **figure 3.3**, one can replace one of the resistors with a strain gauge to create a signal that varies with the change in resistance. There are many ways to connect the system. It exists bridges with one, two or four strain gauges, known as quarter-, half- and full-bridge.

### 3.2.1 Quarter-Bridge Circuit

A quart-bridge circuit is a system where a strain gauge replaces one resistance in the general Wheatstone bridge. **Figure 3.4** shows the general Wheatstone bridge, where a strain gauge replaces the resistance $R_3$. Such quarter-bridge circuit is used to detect any changes in the resistance of the strain gauge because any changes in the resistance will unbalance the circuit. This unbalance in resistance will then produce a nonzero output voltage that can be readable by the measuring device. A quarter-bridge circuit is often used in places where there is short on space, for example on load springs, and in places where the temperature is constant. High sensitivity to temperature changes makes such circuit not applicable for measurements that requires higher accuracy. Manufactures often provide graphs and charts to compensate for such inaccuracies, but this requires installation of a temperature sensor to the system. Therefore, this type of circuit will not be used in the experiments.

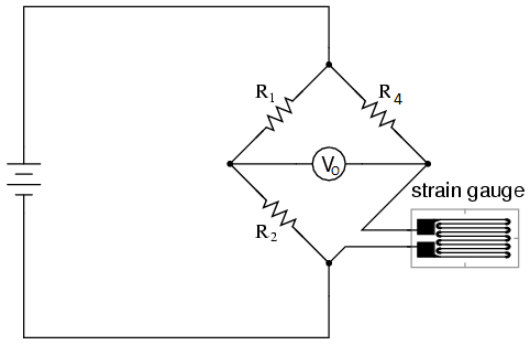


**Figure 3.4:** Quarter-bridge circuit with a strain gauge replacing resistance $R_3$. (All About Circuits, 2015)

The strain gauge in **figure 3.4** measures resistance change, denoted by $R_G$. By using equation (3.4), we can find an expression for the strain-induced change in resistance, denoted by $\Delta R$,

$$\mathrm{GF} = \frac{\Delta R}{R_G \varepsilon} \Leftrightarrow \Delta R = \mathrm{GF} \times R_G \times \varepsilon. \tag{3.5}$$

### 3.2.2 Half-Bridge Circuit

A half-bridge circuit consists of two strain gauges that replaces two of the four resistors in the Wheatstone bridge. Such bridge is used in systems where there is important to measure axial strain and bending in the specimen. This will double the sensitivity of the bridge compared to the quart-bridge circuit. In addition, both strain gauges will help reduce the effects of temperature because both experience the same temperature changes, and therefore will cancel out the effects.

There are two methods to configure a half-bridge circuit, depending on the purpose of the experiment. The first one is half-bridge circuit type I, which is illustrated in **figure 3.5**. Both strain gauges are organized in such a way that the upper one undergoes tension, and the lower one undergoes compression. Hence, this type of half-bridge circuit will only react to bending stress.

Another type of half-bridge circuit is type II. One strain gauge is connected with the direction of the axial stress, and the other one acts in such a way that it will reduce the Poisson strain, and therefore connected perpendicular to the axial stress. This will make it possible to measure both axial and bending strain. **Figure 3.6** illustrates how both strain gauges are oriented relative to each other.

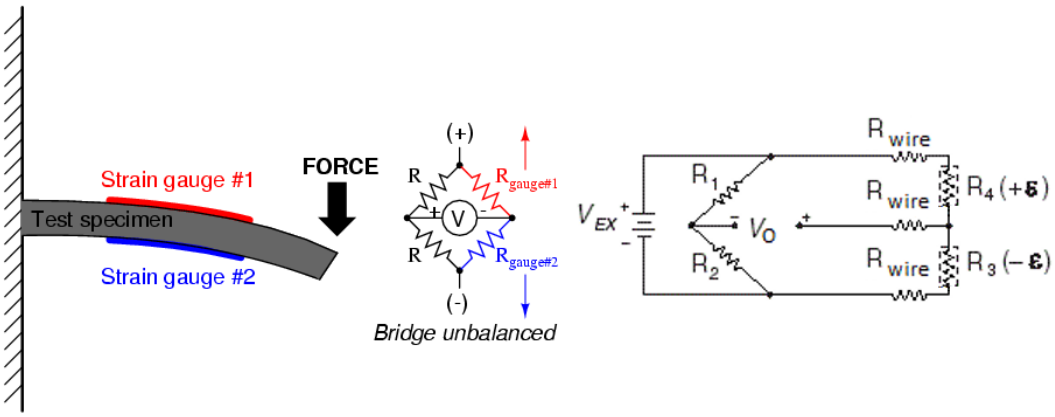


**Figure 3.5:** Left figure shows a downward force applied to a test specimen with an active half-bridge system, and right figure shows the system structure of a half-bridge circuit type I. Strain gauges are organized in parallel to each other and will therefore only react to bending forces. (All About Circuit, 2015; NI, 2015)

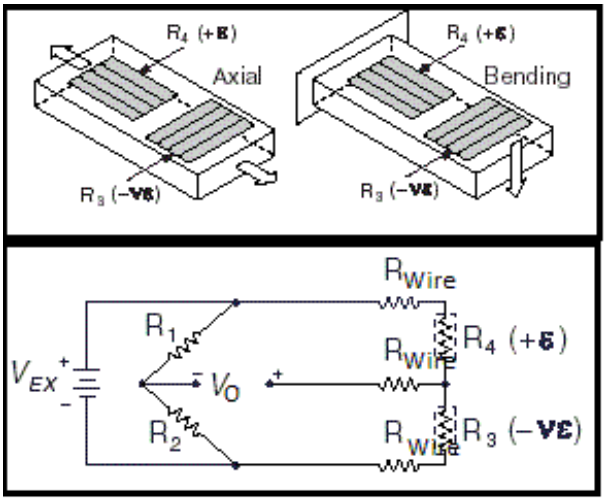


**Figure 3.6:** Half-bridge circuit type II measuring axial and bending strain. (NI, 2016)

### 3.2.3 Full-Bridge Circuit

Four strain gauges can be bonded to the circuit, and create a full-bridge circuit. The advantages of such system is higher sensitivity than the half-bridge circuit, and gives higher amounts of measurements. Like the half-bridge circuit, the full-bridge will compensate for the temperature changes and wire resistance. The disadvantages of such circuit are that it requires more space, more cables to handle, and a complicated process to attach the strain gauges on the test specimen. There exist three methods to connect the strain gauges, depends on the purpose of the measurements.

The first one, full-bridge circuit type I, consists of four active strain gauges that are mounted in such a way that two of them are mounted at the top of the specimen, parallel to each other. The other two are mounted at the bottom, parallel to each other, as shown in **figure 3.7**. Therefore, the top pair will measure tension, and the bottom pair will measure the compression. The bridge is highly sensitive to bending stress, but minimizes the effect of axial stress.

The second one, full-bridge circuit type II, consists of four active strain gauges where two of them are mounted in the direction of the bending stress on both sides of the test specimen. The other two are mounted perpendicular to the principal axis of stress on both sides of the test specimen, and works together to minimize Poisson's strain, as shown in **figure 3.7**. The bridge will only measure bending strain, and will reject axial strain because the two perpendicular strain gauges are connected parallel in the circuit, as shown in **figure 3.7** as $R_1(-\nu\varepsilon)$ and $R_2(+\nu\varepsilon)$.

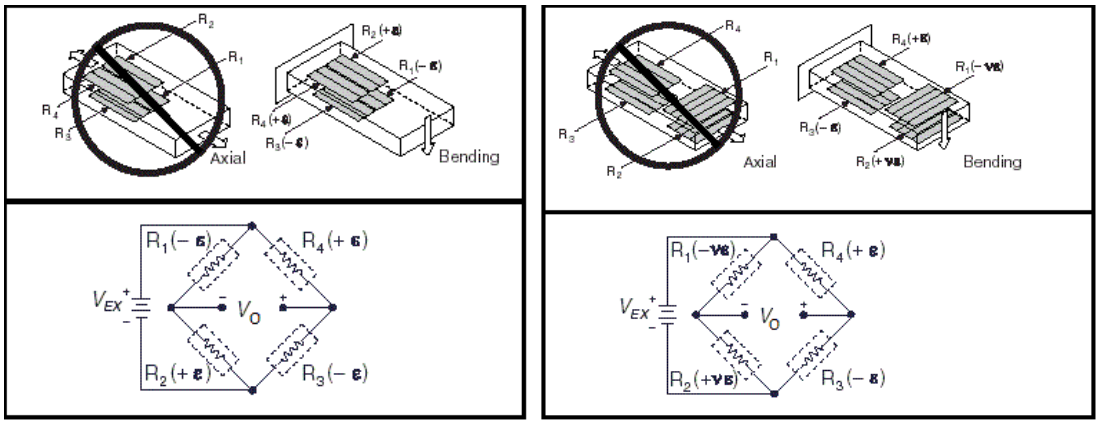


**Figure 3.7:** Left figure shows full-bridge circuit type I, which measures only bending strain. Right figure shows full-bridge circuit type II, measuring only bending strain, but at the same time compensating for Poisson's strain. (NI, 2016)

The third type of full-bridge is mounted the same way as type II, but the difference is the way they are connected to the circuit. By connecting them in both parts of the circuit, as shown in **figure 3.8**, one can compensate for Poisson's strain as well as minimizing the effect of bending stress. This is effective in cases where the primary goal is to measure axial strain. Therefore, this type of bridge circuit is used in the experiments.

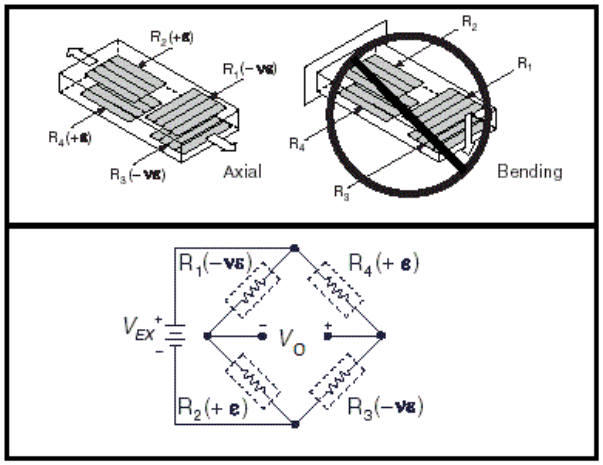


**Figure 3.8:** Full-bridge circuit type III measuring axial strain while compensating for Poisson's strain. (NI, 2016)

Equations (3.4) and (3.5) lays the basement for deriving equations for strain calculated for the different bridge configurations, which results in **table 3.1** where the different strain equations are given. Notice that in cases where wire resistance is crucial, the term $\left(1+\frac{R_{\text{wire}}}{R_G}\right)$ is applied to the equation.

**Table 3.1:** Equations for strain calculations given for the different bridge configurations. (Agilent Technologies, 1999)

| Bridge configuration | Type | Equation for strain $(\varepsilon)$ |
|---|---|---|
| **Quarter-bridge** | Normal | $\varepsilon = \frac{-4V_o}{\mathrm{GF}(1+2V_r)}$ |
| | Compensating for wire resistance | $\varepsilon = \frac{-4V_r}{\mathrm{GF}(1+2V_r)} \times \left(1+\frac{R_{\mathrm{wire}}}{R_G}\right)$ |
| | Compensating for temperature changes | |
| **Half-bridge** | Type I | $\varepsilon = \frac{-2V_r}{\mathrm{GF}} \times \left(1+\frac{R_{\mathrm{wire}}}{R_G}\right)$ |
| | Type II | $\varepsilon = \frac{-4V_r}{\mathrm{GF}\left[(1+\nu)-2V_r(1-\nu)\right]} \times \left(1+\frac{R_{\mathrm{wire}}}{R_G}\right)$ |
| **Full-bridge** | Type I | $\varepsilon = -\frac{V_r}{\mathrm{GF}}$ |
| | Type II | $\varepsilon = -2\frac{V_r}{\mathrm{GF}(\nu+1)}$ |
| | Type III | $\varepsilon = -2\frac{V_r}{\mathrm{GF}\left[(\nu+1)-V_r(\nu\text{-}1)\right]}$ |

Where

$$V_r = \frac{V_O - V_{\mathrm{offset}}}{V_{\mathrm{EX}}}. \tag{3.6}$$

## 3.3 Noise Control

During strain gauge measurements, analog signals are transported through the gauges and to the analog to digital converter (ADC). It is possible to change these signals with electrostatic noise, and leads to inaccurate results and incorrect interpretation of the strain signals. In the worst case, the strain signals can be useless (Vishay, 2013). The sources of electrostatic noise are usually power wires, motors, fluorescent lamps, welding and soldering equipment, vibrators or radio transmitters. The noise can either follow the power-supply wire into the system, or intercept the wiring that transports the analogue signals. Noise following the power-supply wire into the system have specific frequencies, and therefore easy to filter out in the software used to process the measurements. The power-supply noise will show up as 50-60 Hz noise in the measurements (NI, 2012). **Figure 3.9** shows possible noise sources. Notice that the noise affects even the strain gauges. This is especially important in experiments where steel is used. In such cases, it is important to wrap the steel surface with isolating material, such as tape.

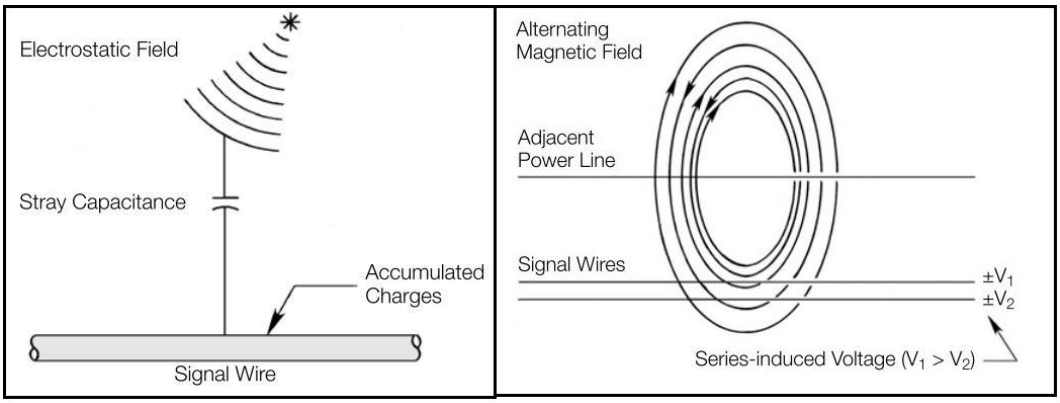


**Figure 3.9:** Electrostatic noise coupling (left) and electromagnetic noise coupling (right). (Vishay, 2013)

Most common barrier against electrostatic noise is a conductive shield, known as a Faraday cage, placed around the conductor. The cage captures charges and preventing them to reach the signal wire. It is necessary to ground the cage for best effect. **Figure 3.10** illustrates how to shield the signal wires from electrostatic noise.

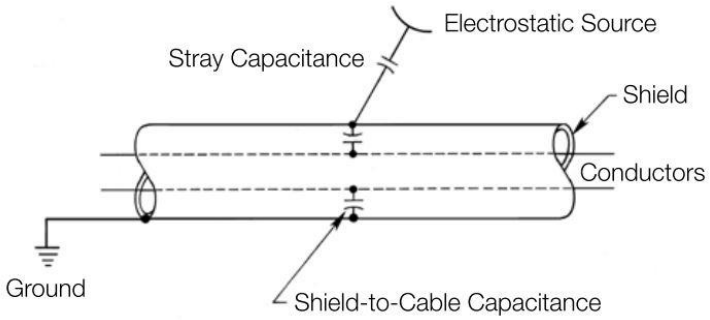


**Figure 3.10:** Electrostatic shielding. (Vishay, 2013)

Short wires should be considered to reduce the effect of wire resistance, but also effects from the environment. Twisting the wires as shown in **figure 3.11** will also reduce the absorption of any noise.

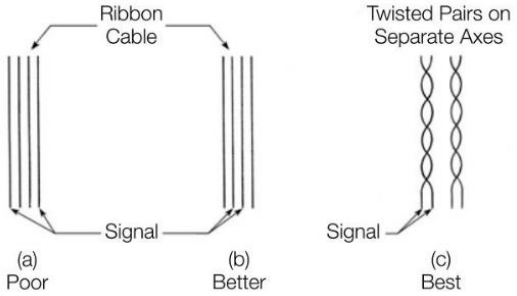


**Figure 3.11:** Cable comparison. (Vishay, 2013)

## 3.4 Calibrating Methods for Strain Gauge Systems

In principle, there is a linear relationship between strain and stress in a strain gauge system. However, this can change due to instrumentation, and the signals can be disproportionate. Three important factors are considered to ensure accurate measurements.

### 3.4.1 Amplification

The actual measurements, $V_O$, of strain gauges are relatively small. The output of the bridges is usually no more than a few $\mathrm{mV}$ per volt of excitation voltage ($V_{EX}$). Therefore, it is necessary to implement an amplifier to increase the signal level and improve the resolution of the measurements. An amplifier increases the measurement data by a factor, $k$. It means that the actual output multiplies by the $k$-factor. The amplifiers used in the experiments has a $k$-factor of 1000.

### 3.4.2 Offset

The output voltage of the bridge is usually nonzero when no stress is applied. This is due to the effects of wire resistance, small differences in resistance among the bridge arms, and temperature changes. There are two methods to offset the initial voltage output, but only the second method is used in the experiments (NI, 2014).

1. Software Compensation: the simplest and fastest method where one initial measurement is done before any stress is applied to the system. This offset value, denoted by $V_{\text{offset}}$, is used to adjust the measurements. Therefore, the following expression should be true in unstrained condition:

$$V_O - V_{\text{offset}} = 0.$$

2. Offset Nulling Circuit: an adjustable resistance, also known as a potentiometer, applies to the circuit to offset the output of the bridge to zero.

### 3.4.3 Shunt Calibration

Shunt calibration is a technique for simulating strain in a strain gauge measurement system by shunting a known resistance to one leg of the bridge. In this way, one can verify the outputs relative to the known or predetermined resistance. A resistor with high amount of resistance, known as $R_S$, connects across one leg of the bridge. This will create a known change in resistance, $\Delta R$. The output compares to the known or expected value. **Figure 3.12** shows the process of shunting $R_S$ across $R_3$ in a strain gauge circuit. Shunt calibration is described in details in Vishay (2013) for all the different bridge circuits.

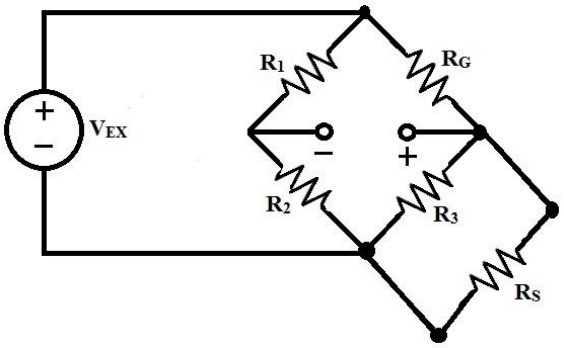


**Figure 3.12:** Shunt resistor with known resistance is connected across $R_3$.

# 4 Experimental Setup

This chapter introduces the setup used in the experiments. Six main experiments have been designed. The first section covers three experiments related to the first scenario with 6, 20, and 46 elements, denoted by experiment I.I, I.II, and I.III. The second section cover experiment II, which consist of experimenting with a continuous pipe. The third and fourth sections relate to scenario two and three, respectively. The setup of the experiments builds on the baseline of a strain gauge structure. Such structure consists of strain gauges on test specimen, an amplifier to amplify the signals, a DAQ measurement hardware, also known as a microcontroller. Finally, a software to process the data. **Figure 4.1** illustrates the system. Section five to nine introduces these components.

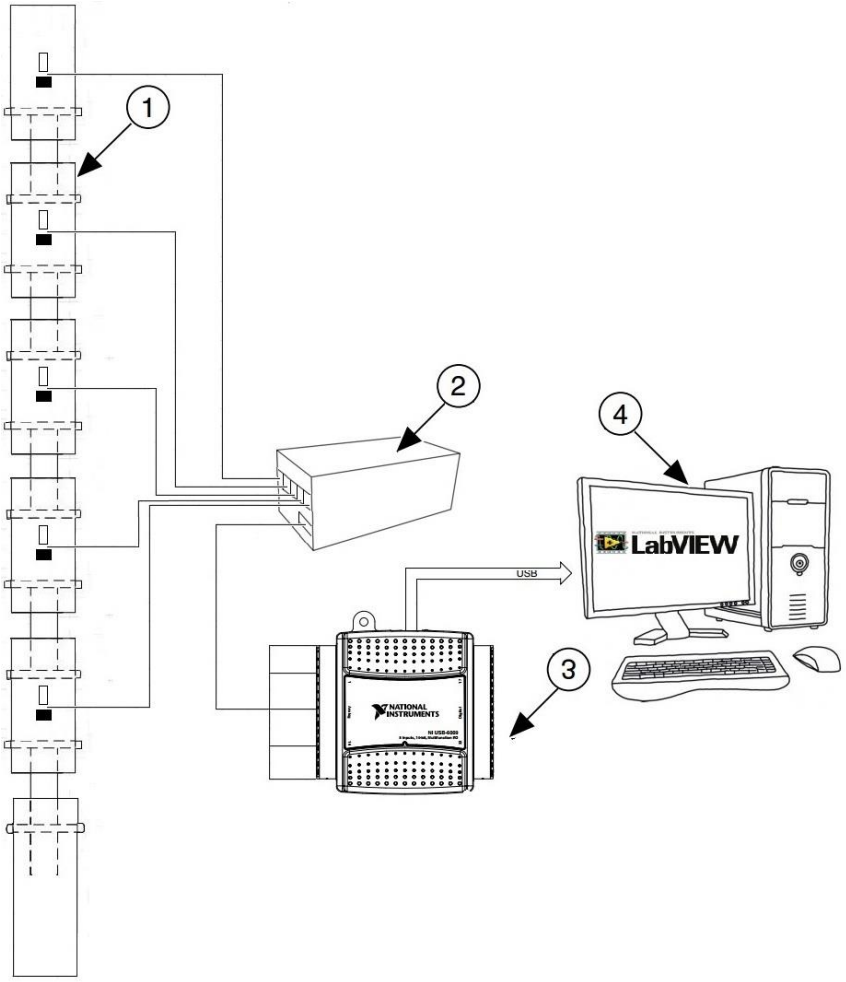


**Figure 4.1:** Block diagram of a typical test system. (1) is the test segment. Notice that the last element is a BHA-segment. (2) is the amplifier system, (3) is the DAQ microcontroller, and (4) is the software where the digital data is processed (LabVIEW).

## 4.1 Experiment I: Vertical Drill String in a Transient State

The purpose of the following experiments is to design a drill string and examine its behavior in form of axial vibrations. A specific weight is loaded on element $i = n-1$ of the drill string, and the weight is then released. The strain in four different elements will be measured. The result will be compared to the numerical simulation to prove the accuracy of the theoretical model. Only the transient state of the system is considered, which is described in details in section 2.2.2.

**Table 4.1:** Technical specifications of experiments I.I-I.III. Channels $\#1-\#4$ indicate element number where the strain gauges are installed.

| Experiment # | Elements | Length$[\mathrm{m}]$ | Channel #1 | Channel #2 | Channel #3 | Channel #4 |
|---|---|---|---|---|---|---|
| **I.I** | 6 | 0.975 | 2 | 3 | 4 | 5 |
| **I.II** | 20 | 2.865 | 2 | 17 | 18 | 19 |
| **I.III** | 46 | 6.375 | 2 | 15 | 30 | 45 |

**Table 4.1** summarizes the technical specifications of the test segments in experiment I.I-I.III. The first test segment consists of six elements. The first five elements consist of $95\ \mathrm{mm}$ long plexiglas pipes connected to $100\ \mathrm{mm}$ long steel pipes. Each element is therefore $135\ \mathrm{mm}$ long. The last element is a $300\ \mathrm{mm}$ long BHA made of steel. **Figure 4.2** and **figure 4.3** illustrates the technical specifications and the setup of the system, respectively. It is important to notice that the plexiglas pipes is assumed to associate with the spring elements in the analytical model. Hence, the steel pipes is the point-mass element and all mass is assumed to be accumulated there. This is a fair approximation because steel has a much higher modulus of elasticity than plexiglas. As a result, only strain on the plexiglas segments will be measured.

The test segment in experiment I.II is extended and consists of 20 elements. The first 19 elements consist of plexiglas-steel pipes, and the last element is the BHA. It is important to notice that the thickness of the plexiglas pipes is changed to $5\ \mathrm{mm}$, i.e. $\mathrm{ID} = 20\ \mathrm{mm}$, as shown in **figure 4.4**. The test segment in experiment I.III is extended to 46 elements. The first 45 elements consist of plexiglas-steel pipes, and the last element is the BHA. It has the same dimensions as experiment I.II, as shown in **figure 4.4**.

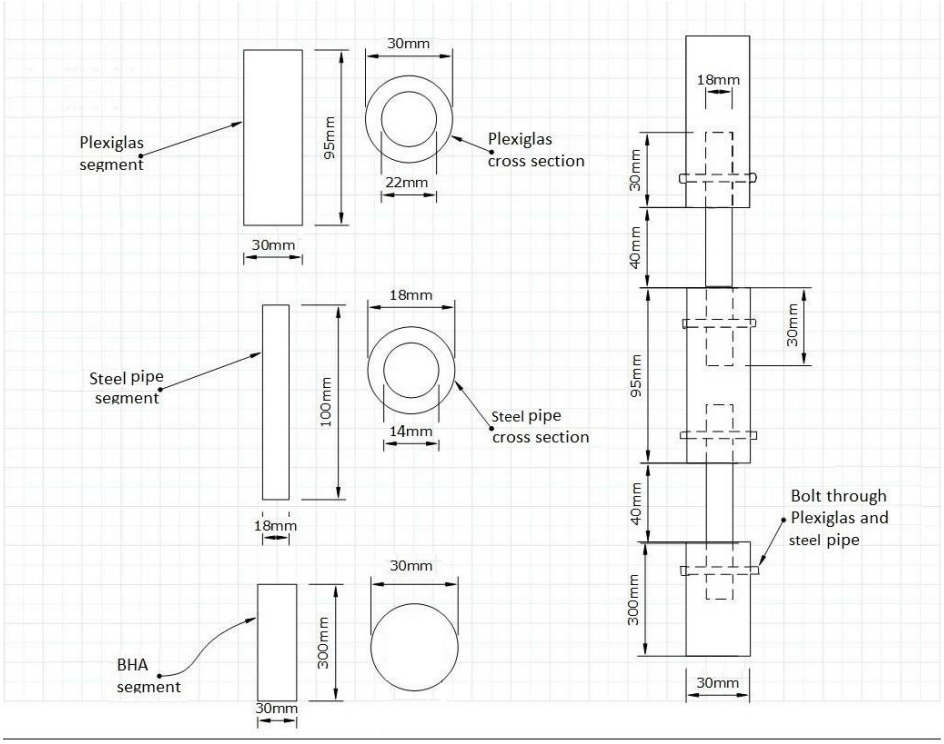


**Figure 4.2:** Technical specifications of experiment I.I. It consists of five elements plus a heavy weight BHA at the end. A full-bridge circuit type III is installed on each of the elements 2-5. (Hassan, 2015)

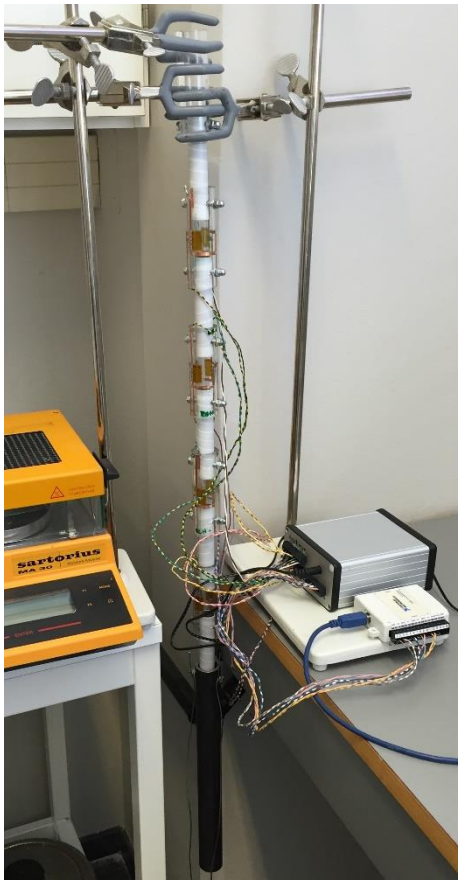


**Figure 4.3:** The experiment I.I setup. The weight loads on element $i = n - 1$.

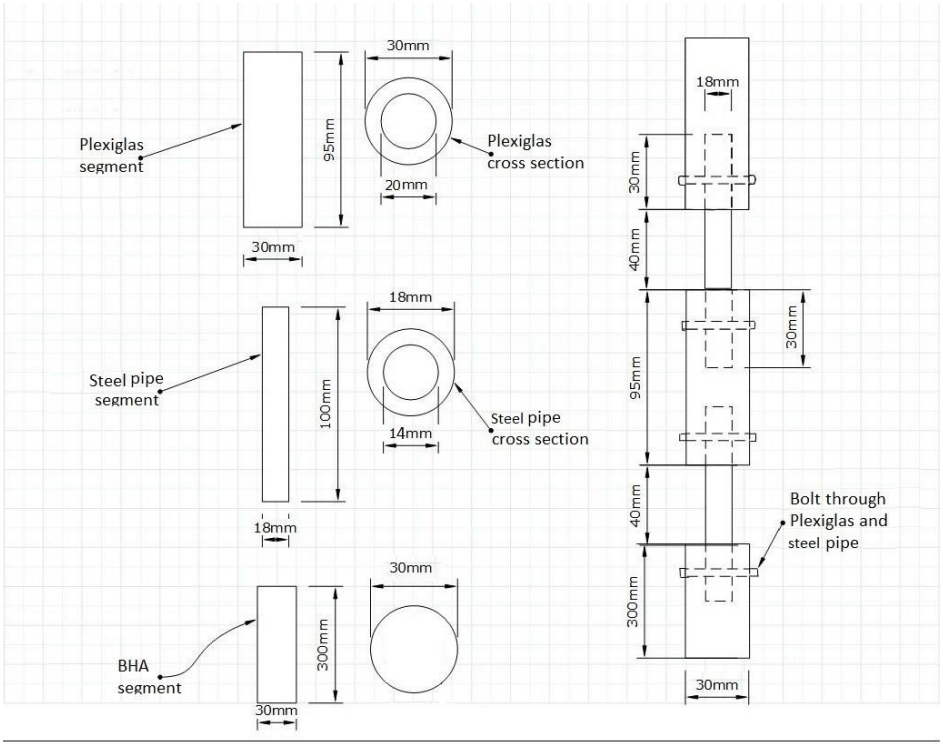


**Figure 4.4:** Technical specifications of the extended test segment in experiment I.II and I.III. Notice that the thickness of the plexiglas segment is changed to 5 mm, i.e. ID = 20 mm.

## 4.2 Experiment II: The Continuous Drill String

This experiment is designed as a control experiment with the purpose of validating the results in experiment I. A continuous plexiglas pipe is chosen with a length of 2.0 m and an outer diameter of 30 mm. Essentially, we want to investigate the behavior of the continuous plexiglas pipe and its reaction to an applied force. This is done by comparing the behavior to the test segments in experiment I. Moreover, this is a method to investigate the reliability of the strain gauges. Four strain gauges are installed in the center of the pipe. The gauges arranges in the so-called full-bridge circuit type III. Similar to experiment I, a specific weight is loaded at the end of the pipe. The weight is then released and the impact measured.

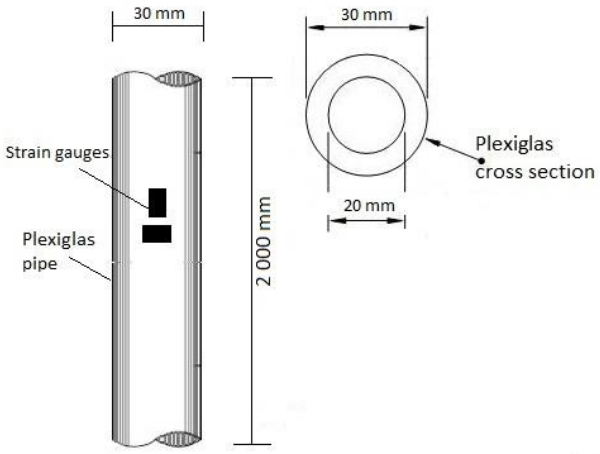


**Figure 4.5:** The technical specifications of the continuous plexiglas pipe.

## 4.3 Experiment III: Step Response

Experimenting with step response on the models presented in experiment I is difficult. This is due to the size of the models. As a result, it requires a motor or a mechanical device that can generate a displacement change faster than the period of the longitudinal mode. The frequency and the period of the pressure waves created as a result of the displacement change, is given by

$$f = \frac{c_s}{2n_r L} \Leftrightarrow T = \frac{1}{f} = \frac{2n_r L}{c_s}, \tag{4.1}$$

where $c_s$ is the speed of sound in the specific material, $n_r$ is the refractive index of the material, and $L$ is the length of the material (Choudhary & Verma, 2011).

The step response produces two longitudinal modes, i.e. a wave that moves downward the system, and then reflected at the bottom of the last element ($n_r = 2$). Obviously, the pressure wave will reach each of the elements at different times due to the distance from the impact zone. Moreover, both plexiglas and steel pipes have different sound velocities. This results in two cases, in which the first one is to only consider the sound velocity of plexiglas. The other case considers only the sound velocity of steel pipes. **Table 4.2** compares both cases and presents the time in which the wave will reach element $i = n - 1$ and reflected back, for experiments I.I-I.III, determined from equation (4.1). The BHA segment is not considered in this evaluation. Furthermore, it is important to notice that the sound velocities of plexiglas and steel are $c_{s,p} = 1700$ m/s and $c_{s,s} = 5920$ m/s, respectively (Classltd, 2013).

**Table 4.2** shows that the three experiments have different times for the longitudinal mode to reach the last plexiglas element, i.e. element $n-1$, and then reflected. This is due to the length of each drill string, whereas experiment I.III has longest test segment and hence longest wave propagation time. Consequently, the model presented in experiment I.III is most suitable for a step response experiment rather than the two other models. Clearly, it is easier for the mechanical motor or device to generate a displacement change at least faster than $4.10\ \text{ms}$ (experiment I.III) rather than $0.456\ \text{ms}$ (experiment I.I). As a result, it is easier to design the mechanical motor to achieve the requirements. This thesis will only consider models presented in experiment I.I and I.III in the numerical simulation.

**Table 4.2:** The effect of longitudinal mode in both plexiglas- and steel pipes for experiments I.I-I.III. The time required for the wave to reach the end of element $i = n-1$, and then reflected, is given by $T$. $f$ indicates the frequency of the pressure wave. Clearly, it takes longer time for the wave to propagate through the plexiglas contra the steel pipe.

| **Experiment** | | **Plexiglas** | | **Steel** | |
|---|---|---|---|---|---|
| # | Total depth for $i = n-1$ [m] | $T$ [s] | $f$ [$\text{s}^{-1}$] | $T$ [s] | $f$ [$\text{s}^{-1}$] |
| I.I | 0.675 | $1.59\times10^{-3}$ | 629.6 | $4.56\times10^{-4}$ | 2192.6 |
| I.II | 2.565 | $6.04\times10^{-3}$ | 165.7 | $1.73\times10^{-3}$ | 577.0 |
| I.III | 6.075 | $14.3\times10^{-3}$ | 70.0 | $4.10\times10^{-3}$ | 243.6 |

## 4.4 Experiment IV: Sinusoidal Driving Force

In order to simulate the test segment in experiment I.III with a sinusoidal driving force, it is necessary to implement a mechanical motor to the system in **figure 4.1**. The mechanical motor will rotate with a predefined, constant angular frequency, and hence create steady constant sinusoidal oscillations. **Figure 4.6** illustrates the principal idea behind the mechanical motor. Choosing low amplitude and high frequency results in a more realistic system. However, it is important to be aware of the measuring frequency of the strain gauges. If the driving frequency of the motor is higher than the measuring frequency of the gauges, the measurements will be invalid and useless.

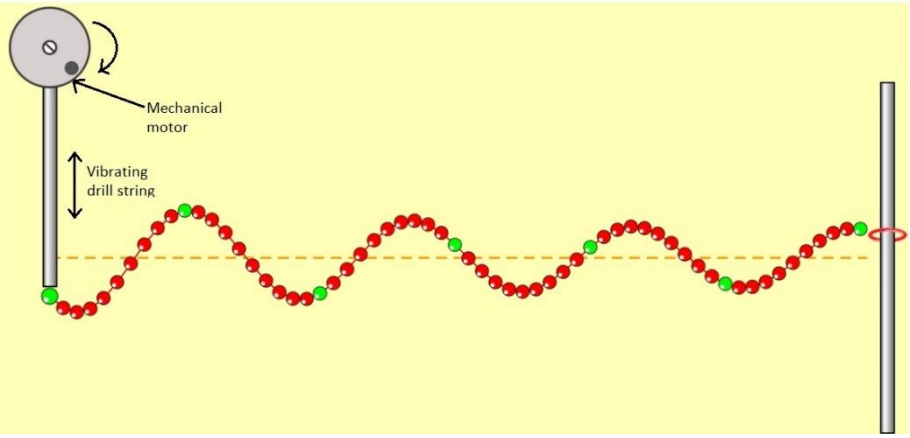


**Figure 4.6:** A mechanical rotating motor installed on the system in order to create steady, sinusoidal oscillations. The rotating device creates vertical vibrations, and forcing the drill string to move along. (Hassan, 2015)

## 4.5 HBM XY Strain Gauge

The strain gauges used in the experiments are manufactured by HBM, of the XY series with two measuring grids arranged at an $90^{\circ}$ offset from each other. Such strain gauges are used for analysis of a biaxial stress state where the principal directions are known. The gauges have a nominal resistance of $120\ \Omega$, and are designed to neutralize the effects of temperature changes automatically. **Table 4.3** presents the technical specification of the strain gauges and the full-bridge circuit type III. Because each system consists of two strain gauges, it makes the process of installing the system on the test bodies much easier. Hence, one has to take into account only two systems when installing the gauges in order to produce the full-bridge circuit.

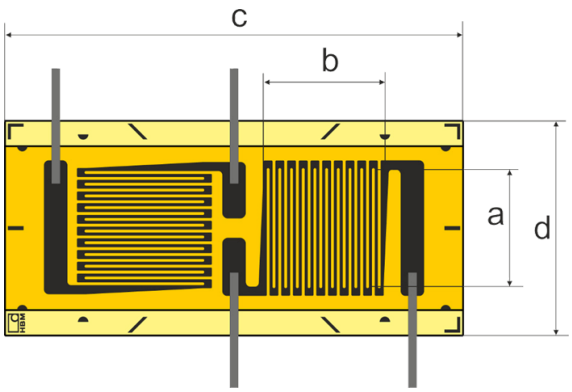


**Figure 4.7:** HBM XY1 rosette strain gauge with two measuring grid. The grid dimensions are $a = 6$ mm, $b = 6$ mm, and $c = 23.5$ mm. (NSMarket, 2016)

**Table 4.3:** Technical specification of the strain gauges and the full-bridge circuit type III.

| Parameter | Value | Unit | Comment |
|---|---|---|---|
| $V_{\text{offset}}$ | 0.00 | V | Offset voltage |
| $V_{\text{EX}}$ | 5.00 | V | Excitation voltage |
| $R_{\text{nominal}}$ | 120 | Ω | Nominal resistance |
| $GF$ | 2 | – | Gage Factor |

## 4.6 The Amplifier System

The signal from the strain gauges amplifies before further processing. Therefore, an amplifier system is custom-built as shown in **figure 4.8**. The signal from the strain gauges enters the system from input port (2), and leaves the system from the output port (3) to the DAQ microcontroller. The system consists of four-paired amplifier of the type BB INA125P, which again connects to each full-bridge strain gauge circuit. **Figure 4.9** shows the basic setup of a single INA125p amplifier. The system powers by a Traco Power DC/DC converter, which converts $18-32$ V input voltage to $\pm 12$ V output voltage. The system will amplify the signals by a factor of 1000, as mentioned in section 3.4.3.

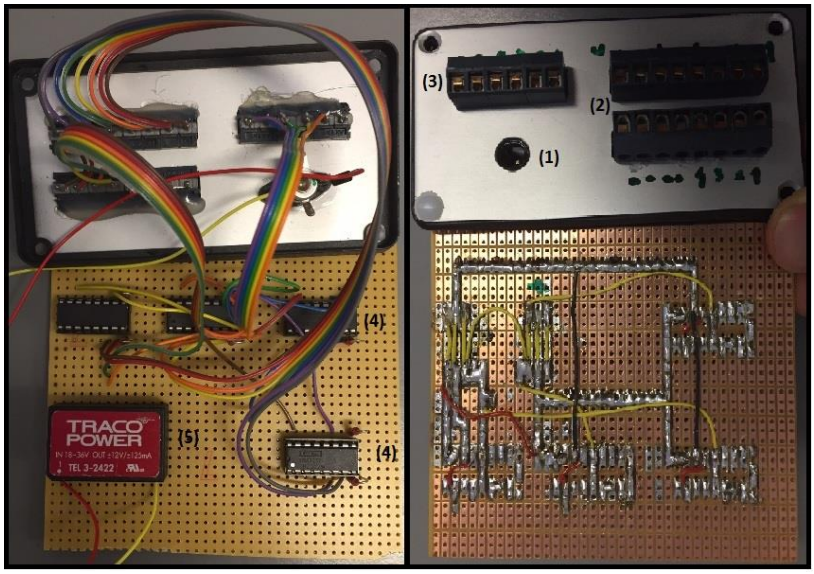


**Figure 4.8:** The structure of the amplifier. (1) is the power supply, (2) is the input port from the strain gauges, (3) is the output port that goes to the DAQ microcontroller, (4) is the BB INA125P amplifier and (5) is the TRACO POWER DC/DC converter.

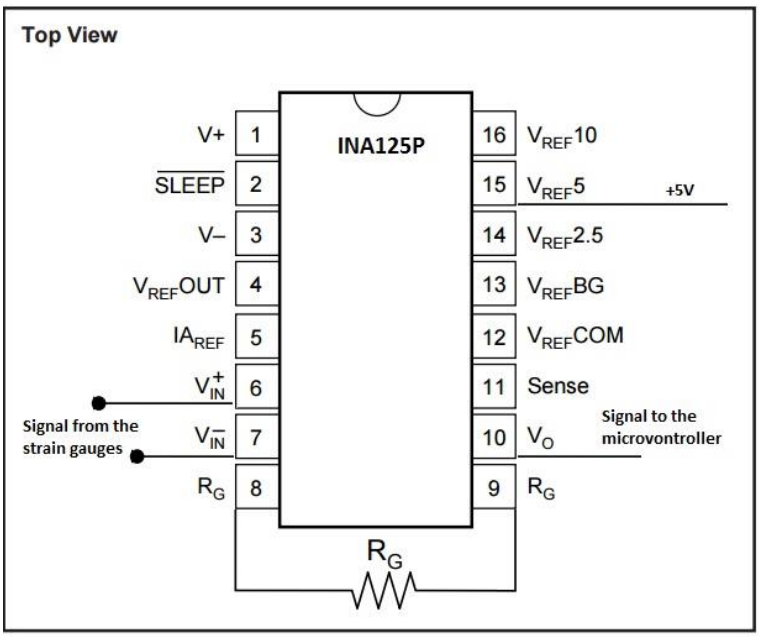


**Figure 4.9:** The basic setup for a single BB INA125P amplifier. Signals from the full-bridge strain gauge circuit enters the system at the ports $V_{IN}^{+}$ and $V_{IN}^{-}$. The signals are then amplified by a gaining factor of 1000, and leaves the system from port $V_O$. (ChinaICMart, 2012)

## 4.7 DAQ Microcontroller

The amplified signal transports to the data acquisition hardware, also known as DAQ microcontroller. The NI USB-6009 device provides eight single-ended analog input channels, AI, two analog output channels, AO, 12 digital input/output channels, DIO, and a 32-bit counter with a full-speed USB interface (NI, 2015). The analog signals connect to the AI input channels. The DAQ microcontroller converts the signals to readable, digital signals, before transporting to a computer through the USB channel for further processing in LabVIEW. **Figure 4.10** illustrates the system.

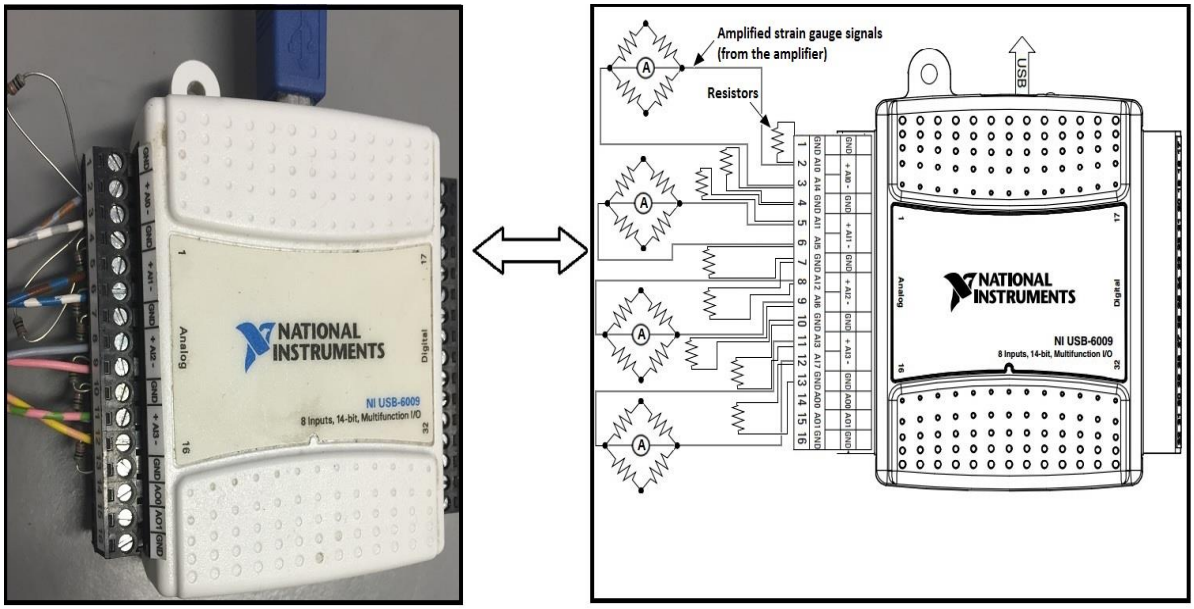


**Figure 4.10:** Left figure shows how the amplified signals from the strain gauge circuits are connected to the DAQ microcontroller. Right figure shows the block diagram of the system. Notice the 8 resistors that are connected between GND (ground) and the analog input channels, AI.

## 4.8 LabVIEW

Laboratory virtual instrumentation engineering workbench, also known as LabVIEW, is a visual programming language where one builds a block diagram and a control panel. The blocks connect together by strings so that the programming becomes visual. The program will then be of such a high level that it does not require any programming skills from the operator. Therefore, behind each block several blocks perform necessary tasks that together will build up that specific block. LabVIEW operates also graphical while- and if-loops.

The digital signals from the DAQ microcontroller are automatically processed in LabVIEW according to the specific designed block diagram. Appendix **C** illustrates the designed block diagram.

It is worth mentioning that the measuring frequency of the circuit is $11{,}000\ \text{Hz}$, and because of that, LabVIEW cannot filtrate and smoothen the signals during the measurements. Therefore, the method of Savitzky-Golay filtering applies to the raw data to "smooth out" the noisy signal before further processing. Appendix **D** provides further details about the method of Savitzky-Golay filtering.

## 4.9 Simulations in MATLAB

The analytical model presented in section 2.2 is implemented and simulated in the numerical computing program MATLAB for the three scenarios. For this, three main assumptions are required to simplify the algorithm. First, it is important to assume that only the plexiglas elements reacts to stress. Hence, the strain gauges are only installed on the plexiglas elements. Because of much higher modulus of elasticity of the steel elements, the stress acting on them results in negligible strain. This is compatible with the lumped element model because the plexiglas elements act as the spring elements, and the steel pipes as point masses. Moreover, each element is designed as a 95 mm plexiglas element and a 100 mm steel element. This results in the length of 135 mm for all elements except the BHA, which is 300 mm long HWDP (**figure 4.2** and **figure 4.4**).

Because of the simplicity of the analytical model, it is necessary to assume that all the non-conservative forces acting on the system are integrated into the viscous friction force $R$. Clearly, equation (2.14) from section 2.2.1 shows that the magnitude of the viscous friction force varies only with the viscosity of the liquid, $\mu$. This means that the viscosity parameter behaves more like the friction factor of the system rather than a parameter related only to the viscous fluid. The viscosity of the three systems in section 2.2.2 is chosen in accordance with the experimental results. The determined value of the viscosity of the underdamped system (section 2.2.2.3) lays the ground for the numerical simulations of experiment III and IV.

**Table 4.4** presents the necessary input parameters of the models for the three scenarios. It is important to notice that an "invisible" borehole is created around the drill string. Creating such borehole makes it possible to calculate alpha, $\alpha$, which is the ratio between the outer radius of the drill string and the borehole, and hence determine the viscous friction force. The argument behind determining the size of the borehole is the relation between a $9\ ⅝''$ borehole drilled with a $5\ ½''$ drill string, which is 1.75. The outer radius of the drill string in our system is $15\,\text{mm}$, which results in $26.25\,\text{mm}$ as the outer radius of the "invisible" borehole.

Table 4.4: Input parameters in MATLAB.

| Parameter | Value | Unit | Parameter Description |
|---|---|---|---|
| $l_i$ | 0.135 | m | Length of each elements |
| $l_{\text{BHA}}$ | 0.300 | m | Length of BHA |
| $r_{\text{Plexiglas}}$ | 0.015 | m | Outer radius of the plexiglas pipe |
| $r_{\text{steel}}$ | 0.009 | m | Outer radius of the steel block |
| $r_{\text{BHA}}$ | 0.015 | m | Outer radius of BHA |
| $R_{\text{hole}}$ | 0.026 | m | Assumed radius of the “borehole” |
| $\rho_{\text{steel}}$ | 7850 | $\frac{\text{kg}}{\text{m}^3}$ | Density of steel (ETB, 2015) |
| $\rho_{\text{Plexiglas}}$ | 1180 | $\frac{\text{kg}}{\text{m}^3}$ | Density of plexiglas (PubChem, 2015) |
| $m_{\text{element}}$ | 0.116 | kg | Mass of each drill string elements |
| $m_{\text{BHA}}$ | 1.66 | kg | Mass of the BHA segment |
| $\nu_{\text{plexiglas}}$ | 0.35 | – | Poisson’s ratio, plexiglas (Altuglas, 2008) |
| $E_{\text{Plexiglas}}$ | 3.1 | GPa | Young’s modulus, plexiglas (Altuglas, 2008) |
| $E_{\text{steel}}$ | 210 | GPa | Young’s modulus, steel (ETB, 2015) |

# 5 Experimental Results and Evaluation

The most important findings from experiments and simulations are presented in this chapter. Sections that consist of both experimental results and numerical simulations divides into three parts (experiment I.I and I.II). Firstly, the measured raw data is filtrated and converted to displacement before plotting and presented in graphs. Secondly, numerical results from simulations in MATLAB are presented for their respective systems, i.e. overdamped and underdamped systems. Finally, both results are plotted together for the specific elements, in order to find correlations between both models.

Only results from simulations are presented for experiment I.III, III, and IV. The respective elements have been selected arbitrary.

The results of the continuous plexiglas pipe in experiment II are compared to the experimental results in experiment I.II.

## 5.1 Experiment I

The initial systems in experiment I.I and I.II was loaded with the same weight of $10\ \text{kg}$ while LabVIEW measured the output data from the DAQ microcontroller. The mass was then removed instantly and the output data were recorded until the system reached initial state. The output data from LabVIEW was then imported to MATLAB.

Before further processing of the raw data, it is necessary to filtrate and smoothen the data to eliminate the unnecessary noise, as described in section 4.8. The method of Savitzky-Golay (polynomial) smoothing filter is implemented for each output data. In order to filtrate the data, it is necessary to determine the polynomial order, $p$, which creates the polynomial equation that approximates the data points. It is also necessary to determine the frame size, $N$, known as the data window in which the model considers when looking at each individual point during the smoothing routine. **Figure 5.1** compares three cases of filtration with the original data. Obviously, higher polynomial order in combination with smaller frame size results in less filtration, i.e. closest to the original data (case I). In comparison, case III presents a more realistic filtration because it filtrates out the unnecessary noise and at the same time preserves the shape of the original data. Hence, a polynomial order of $p = 5$ and a frame size of $N = 51$ is chosen in the filtration of all the output data from the experiments.

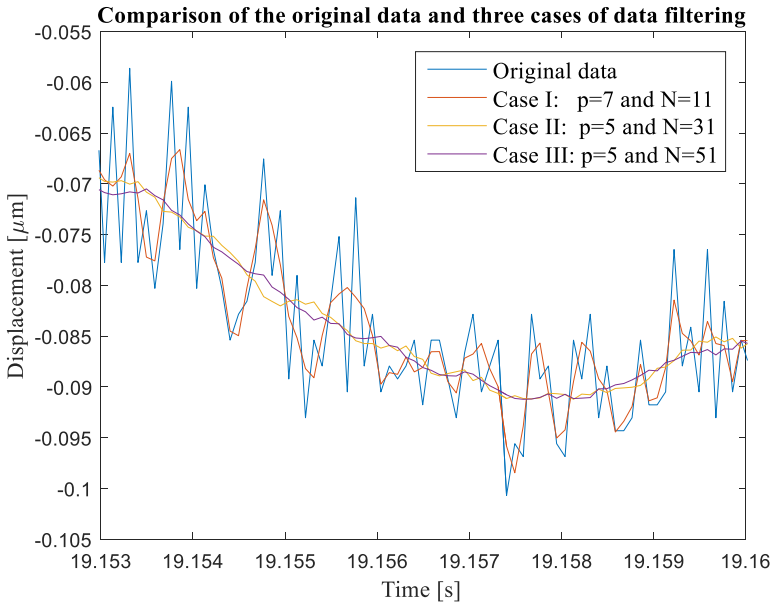


**Figure 5.1:** Comparison of the original data and three cases of data filtration. Higher polynomial order in combination with low frame size gives less filtration (case I). In comparison, higher frame size gives a more realistic view because it filtrates out the unnecessary noise and at the same time preserves the shape of the original data (case III).

It is necessary to convert the filtrated voltage data to strain. **Table 3.1** in section 3.2 provides the correct formula for calculating the strain for the full-bridge circuit type III, which is

$$\varepsilon = -2\frac{V_r}{\mathrm{GF}\left[(\nu+1)-V_r(\nu-1)\right]},$$

where $V_r = \dfrac{V_O - V_{\text{offset}}}{V_{\text{EX}}}$. $V_{\text{offset}}$, $V_{\text{EX}}$, and GF are given in **Table 4.3**. The final stage of determining the displacement of each measuring points is by using equation (3.1), i.e. $\Delta L = \varepsilon L_0$ where $L_0$ is the initial length of each element.

### 5.1.1 Experiment I.I

**Figure 5.2** illustrates the displacement of the four channels (measuring points) during the entire experiment. Observing the fact that before offset nulling the circuit in LabVIEW, each element has a significantly different initial displacement. Element 4 and 5 starts with positive displacement. On the other hand, element 2 starts with negative displacement, while element 3 does not sustain the same level of initial displacement. This behavior is a result of the way the strain gauge circuits are connected to the amplifier system. However, the offset nulling process in LabVIEW correlates this diversity.

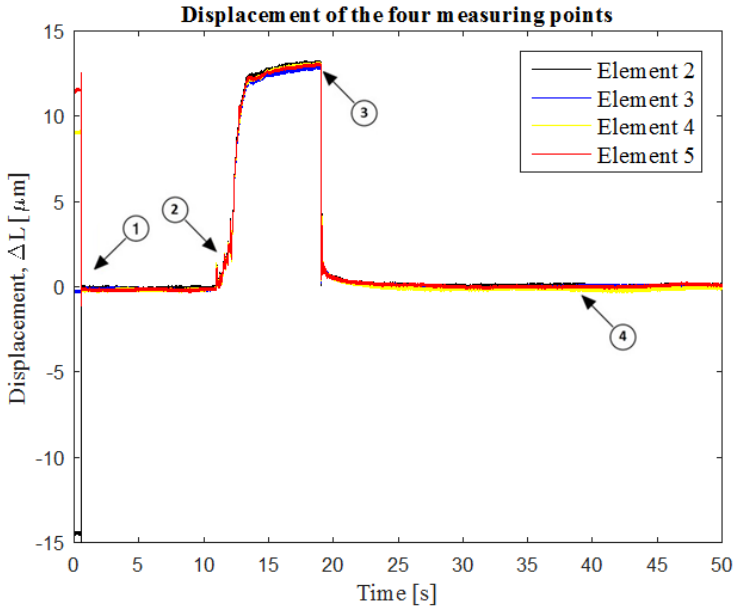


**Figure 5.2:** Displacement of elements 2-5. The plot presents the process of offset nulling the circuit (1), loading a mass of 10 kg on the system (2), instantly remove the mass (3), and observe the process of returning to initial state (4).

**Figure 5.3** shows the behavior of the system during, and after the release of the mass. Observations indicate that it takes the system approximately 12 ms from the mass is released until it reaches the point where it starts to stretch again.

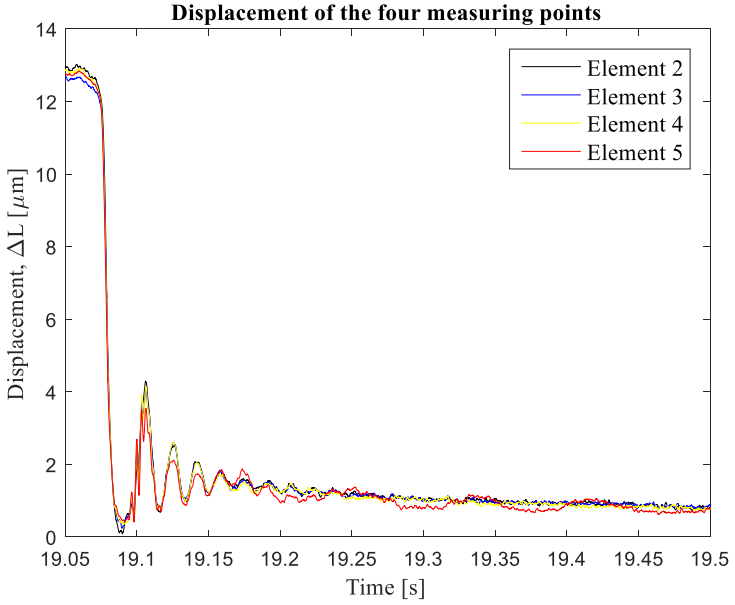


**Figure 5.3:** Displacement of elements 2-5 during release of the mass. The system reaches the initial state during the first 500 ms after the impact.

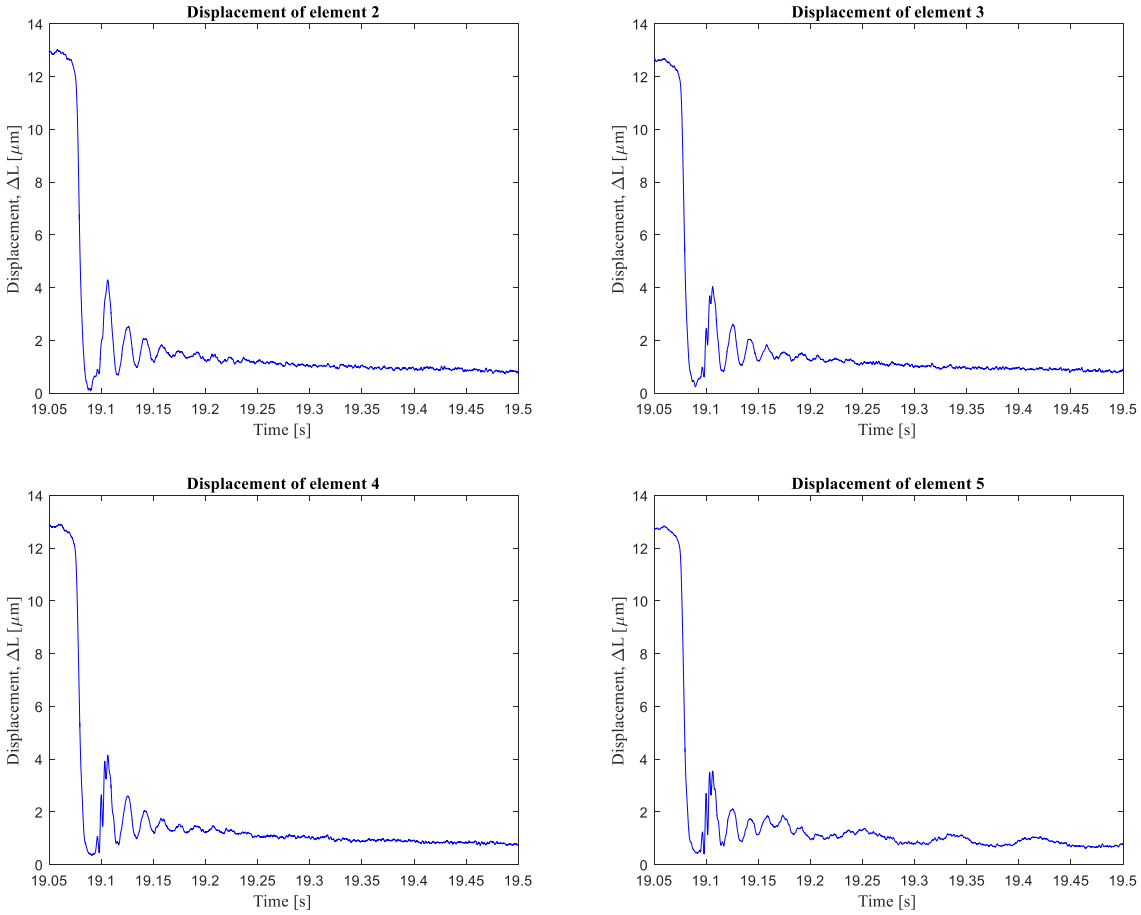


**Figure 5.4:** Displacement of each element during, and after release of the mass. Element 5 behaves different because after the impact, the element oscillates with relatively high period before it reaches the initial state. In contrast, element 2-4 oscillates maximum four times with quite low period (approximately 18 ms ) before they reaches initial state.

By implementing the transient state of the vertical drill string in MATLAB for the three systems, i.e. overdamped, critically damped, and underdamped systems, it is possible to compare them to the experimental results. Furthermore, it is important to adjust the magnitude of the viscosity for the three systems. This is done to satisfy the requirements of the damping ratio. Three arbitrary parameters are chosen so that

$$\mu\left[\text{Pa}\times\text{s}\right]=\begin{cases}180 & \text{for overdamped system, i.e.} \quad \varsigma_i=1.55857594\\ 115.49006 & \text{for critically damped system, i.e.} \quad \varsigma_i=1.00000000\\ 1.5 & \text{for underdamped system, i.e.} \quad \varsigma_i=0.01298813.\end{cases}$$

The critically damped system requires a damping ratio that equals one, i.e. $\varsigma_i=1$. It is difficult to determine a value for the viscosity in order to satisfy such requirement. However, the viscosity can be approximated so that the damping ratio is close to one. This is a fair assumption because the deviation is negligible $\left(\Delta\varsigma_i=2.22\times10^{-16}\right)$.

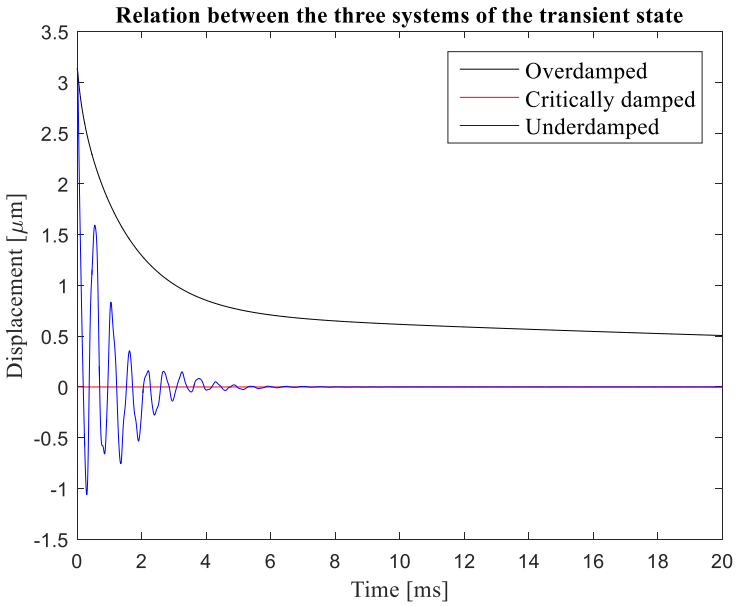


**Figure 5.5:** Relation between overdamped. Critically damped, and underdamped systems of the transient state. Observing that the critically damped system dies out rapidly without oscillating, and reaches zero at 0.05 ms. The underdamped system on the other hand oscillates at least six times before the vibrations dies out. In comparison, the overdamped system slightly decreases to zero.

**Figure 5.5** illustrates the relation between the three systems of the transient state. Obviously, the critical damped system cannot be further considered because of its rapidly decreasing behavior. However, evaluating the overdamped system for elements 2-5 are necessary before comparing them to the experimental results.

The behavior of the overdamped system for elements 2-5 is shown in **figure 5.6**. Clearly, the elements have the same decreasing time with an approximate value of 250 ms. Close observation indicates that each element has a different initial displacement. Element 2 starts with the lowest initial displacement $\left(\Delta L_2 = 1.25\ \mu\text{m}\right)$ and the value increases proportional with increased element numbers.

This is a result of Hooke's law where the initial displacement of element $i$ is a sum of initial displacements of the previous elements, i.e. $\Delta L_n = \sum_{i=1}^{n-1} \Delta L_i \Leftrightarrow L_n = \sum_{i=1}^{n-1} L_i$.

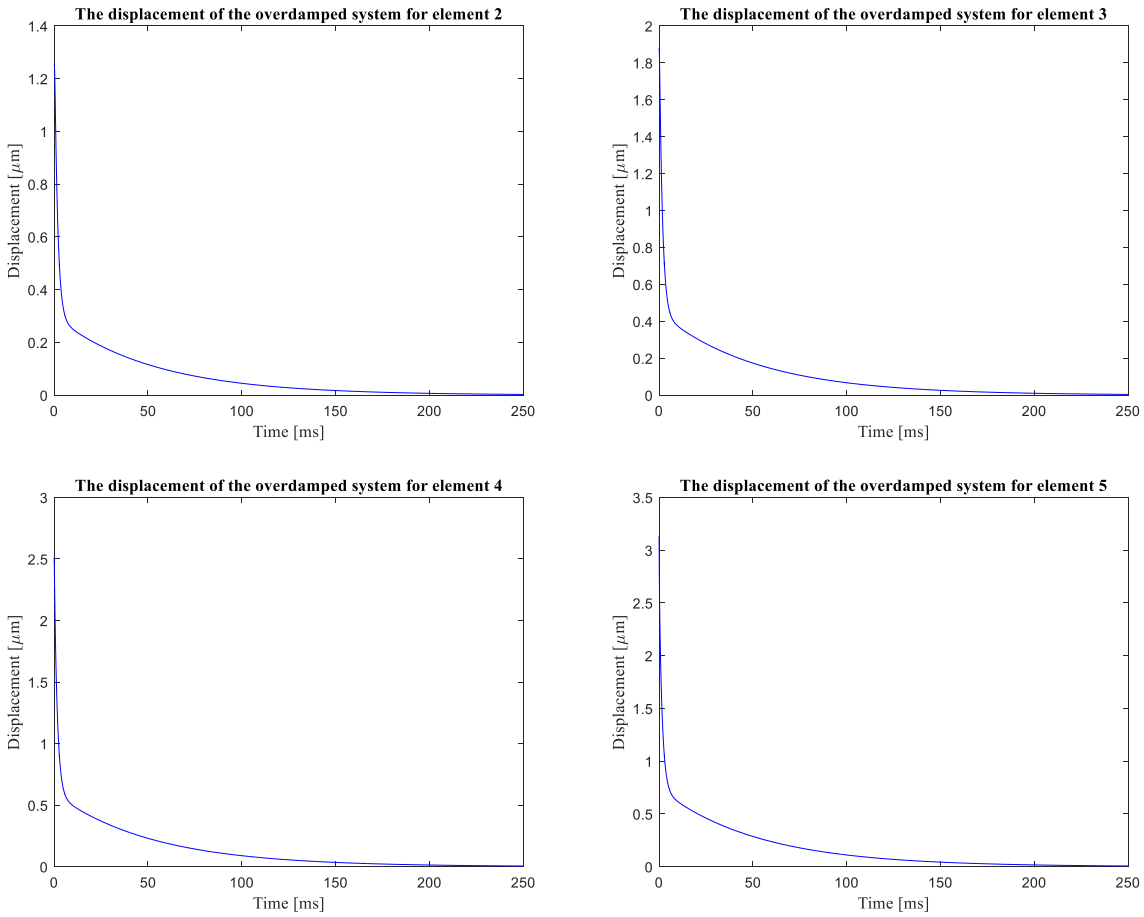


**Figure 5.6:** The overdamped system for elements 2-5. Observing that the elements decreases towards zero with the same decreasing time. Furthermore, each element starts at different initial displacement due to Hooke's law. Hence, element 5 have highest initial displacement.

**Figure 5.7** illustrates the comparison of the overdamped system and the experimental results of elements 2-5. After close observation, it is found that there are no correlations between both models. This is due to the non-oscillating behavior of the overdamped system. In comparison, the experimental model tends to oscillate at least six times before it dies out. In addition, the initial displacement of the experimental model is approximately 13 µm. The value tends to diverge between the elements, but this diversity is minimal. The initial displacement of the overdamped system on the other hand is much lower, starting at 1.3 µm for element 2, and increases to 3.5 µm for element 5.

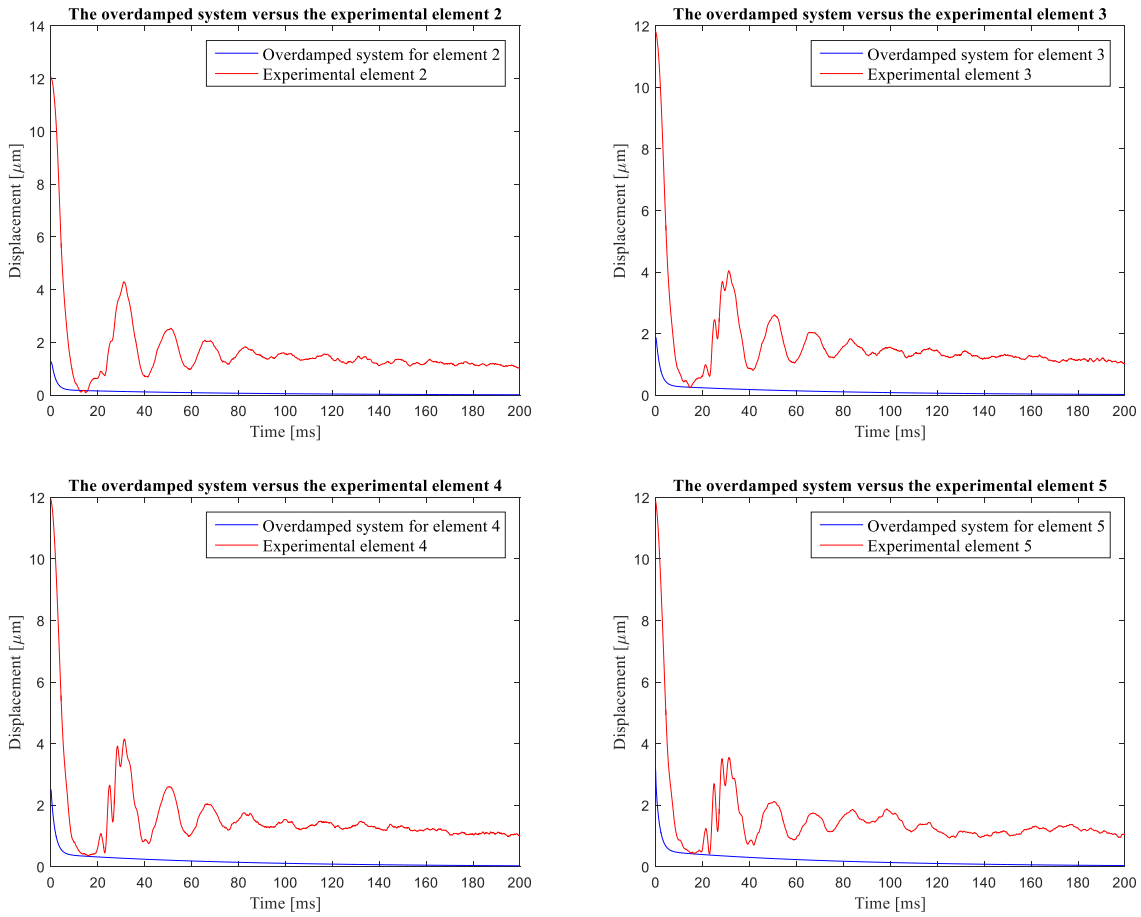


**Figure 5.7:** A comparison of the experimental results and the overdamped system for elements 2-5.

**Figure 5.8** illustrates the behavior of the underdamped system for elements 2-5. Clearly, the elements reach zero at the same time, i.e. at 5 ms. Similar to the overdamped system, each element have different initial displacement. This is again due to Hooke's law, which results in increased initial displacement as we move down the elements in the vertical drill string. Moreover, observations indicate that the shape of the waves becomes clearer from element 2 to element 5, i.e. element 5 have better wave shape than element 2.

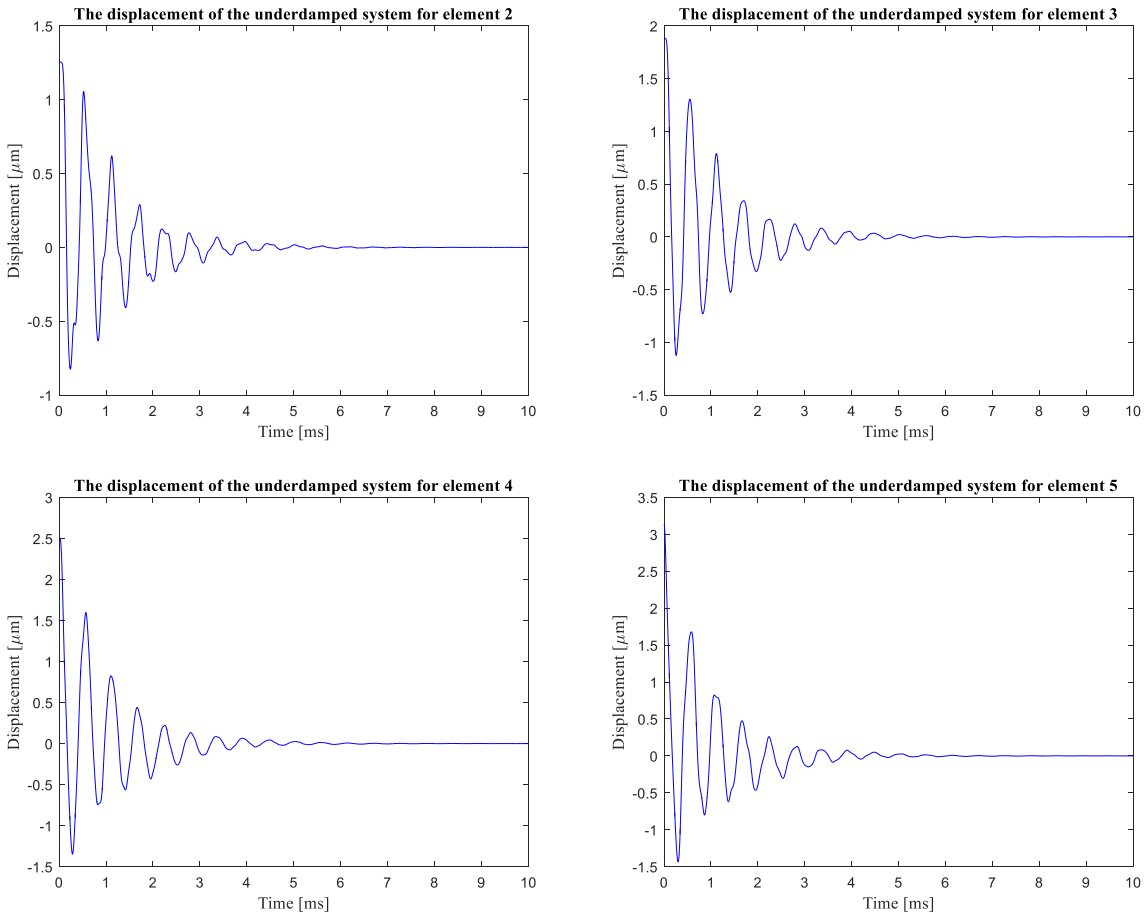


**Figure 5.8:** The underdamped system for elements 2-5. Clearly, the elements reach zero at the same time $(5\text{ ms})$. Similar to the overdamped system, each element starts at different initial displacement due to Hooke's law.

The comparison of the underdamped system and the experimental results for elements 2-5 are illustrated in **figure 5.9**. By comparing both results, it is clear that there are no similarities between the systems. The underdamped system oscillates with much higher frequency, and hence dies out long before the experimental system. The waves of the underdamped system have a period of $T \approx 0.5$ ms. In comparison, the waves of the experimental system have a period of $T \approx 16$ ms. Besides, the amplitudes of the underdamped system are much lower. The underdamped model tends to cross origin multiple times. This means each element undergoes compression. This behavior is not observed in the experimental model.

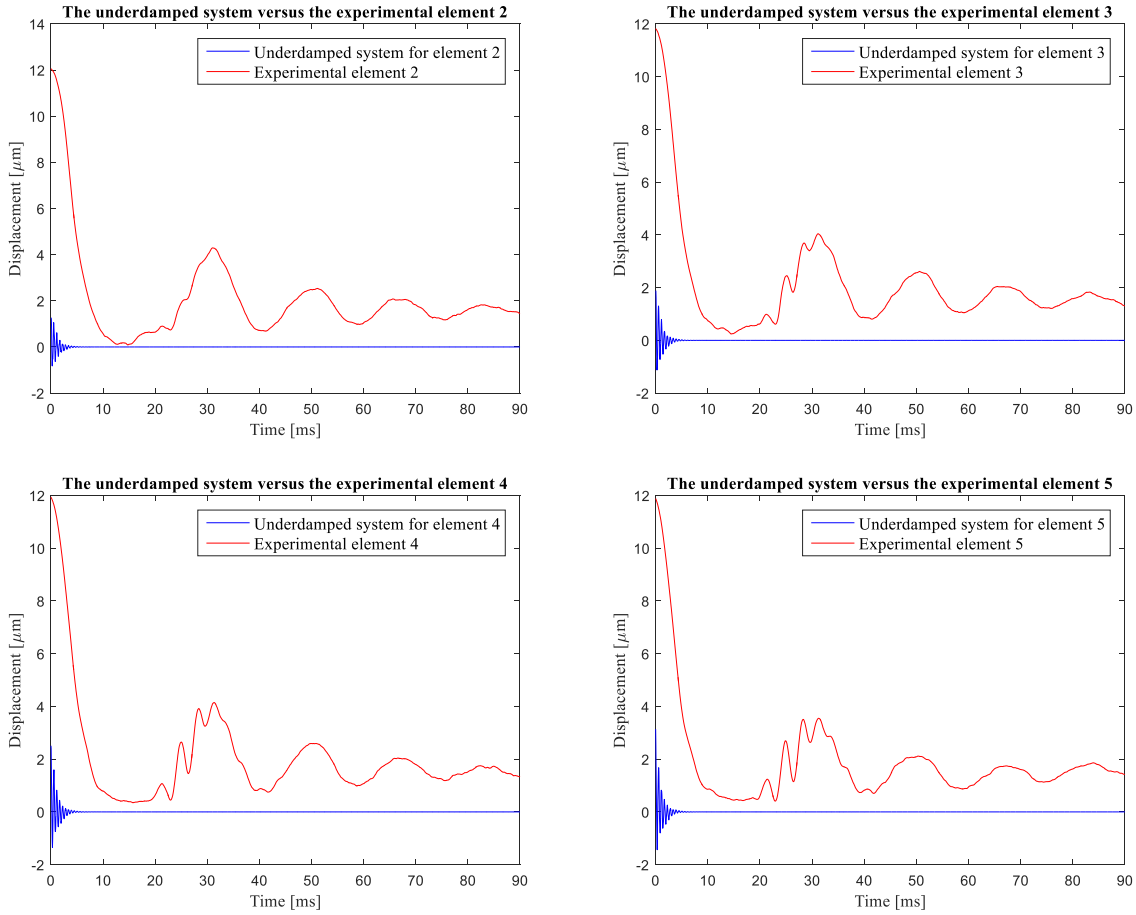


**Figure 5.9:** A comparison of the experimental results and the underdamped system for elements 2-5.

### 5.1.2 Experiment I.II

**Figure 5.10** shows the behavior of the system during, and after the release of the mass. Observation indicates that it takes the system approximately 20 ms from the mass is released until it reaches the point where it starts to stretch again.

**Figure 5.11** illustrates the displacement of each element during, and after the release of the mass. Element 2 behaves differently because it oscillates with a higher amplitude, and goes below zero at least two times, i.e. the element undergoes compression. In contrast, elements 17, 18, and 19 oscillate with approximately same amplitude, and neither of them goes below the zero line $(y = 0)$.

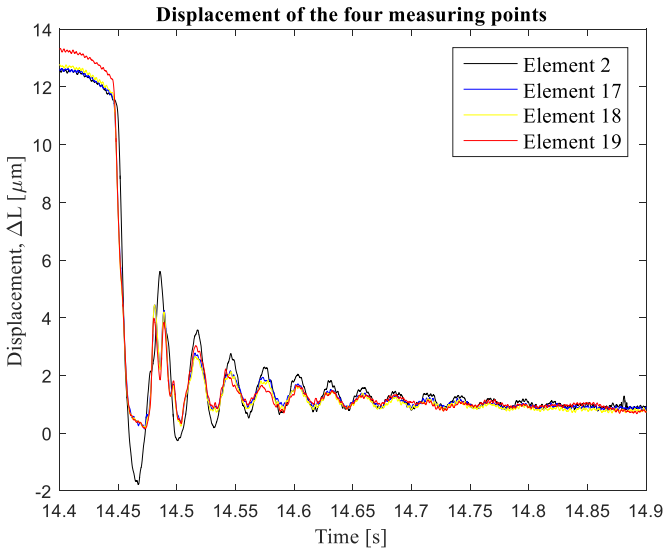


**Figure 5.10:** Displacement of elements 2, 17, 18, and 19 during release of the mass. It take the system 400 ms to reach the steady state.

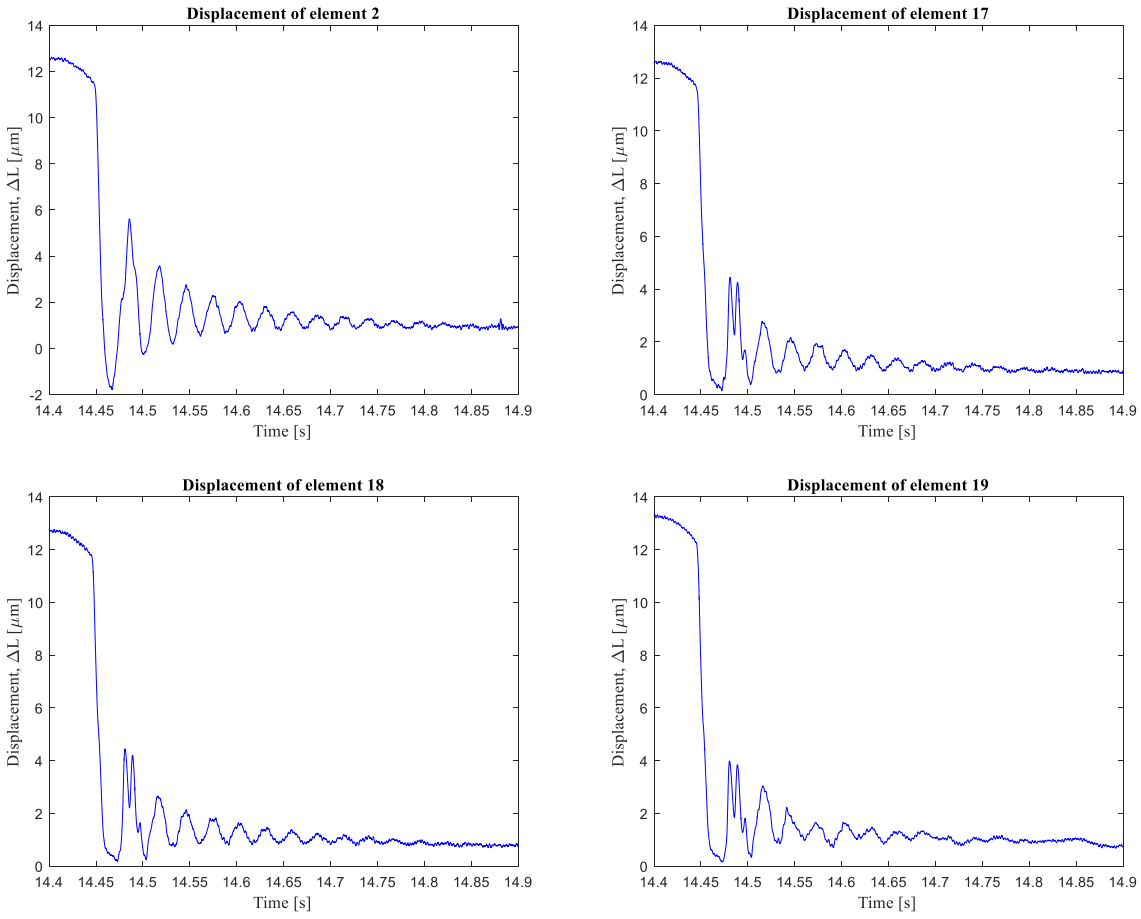


**Figure 5.11:** Displacement of element 2, 17, 18, and 19 during, and after release of the mass.

Regarding the transient state of the system, only the overdamped and the underdamped systems are considered. Because of the rapid decreasing behavior of the critical system, it cannot be considered. However, before further evaluation it is important to adjust the magnitude of the viscosity for both systems. This is done to satisfy the requirements of the damping ratio, but also to fit the experimental results. Two arbitrary parameters are chosen so that

$$\mu\left[\mathrm{Pa}\times\mathrm{s}\right]=\begin{cases}55 & \text{for overdamped system, i.e.} \quad \varsigma_i = 1.53193728\\ 0.035 & \text{for underdamped system, i.e.} \quad \varsigma_i = 0.00097487.\end{cases}$$

**Figure 5.12** illustrates the overdamped system for elements 2, 17, 18, and 19. Similar to experiment I.I, it is clear that the initial displacement increases as we move down the elements in the vertical drill string. Again, this is a result of Hooke's law. Furthermore, observation indicates that the elements behave similar regarding decreasing time and the required time to reach equilibrium state. However, by analyzing the initial displacement of each element, i.e. the displacement at $0\ \mathrm{ms} \le t \le 2.5\ \mathrm{ms},$ it can be found that element 2 has a response time of $t_r \approx 0.4\ \mathrm{ms}.$ This is due to the period of the longitudinal mode created as a result of removing the mass. By using equation (4.1) in section 4.3, it is possible to determine theoretically the period of the longitudinal mode, i.e. the time required for the wave to reach element 2 and reflected back. The distance between element 19 and element 2 is $2.16\ \mathrm{m}.$ If we consider both plexiglas- and steel pipe systems, we get

$$T_{\text{plexiglas}} = \frac{2n_r L}{c_s} = \frac{4\times 2.16}{1700} = 5.082\ \mathrm{ms} \Leftrightarrow t_{\text{plexiglas}} = 2.541\ \mathrm{ms}$$

$$T_{\text{steel}} = \frac{2n_r L}{c_s} = \frac{4\times 2.16}{5920} = 1.46\ \mathrm{ms} \Leftrightarrow t_{\text{steel}} = 0.73\ \mathrm{ms}.$$

Evidently, the time required for the longitudinal mode to reach element 2 through steel is closer to the actual value than through plexiglas. This means that the steel elements play a higher role than expected.

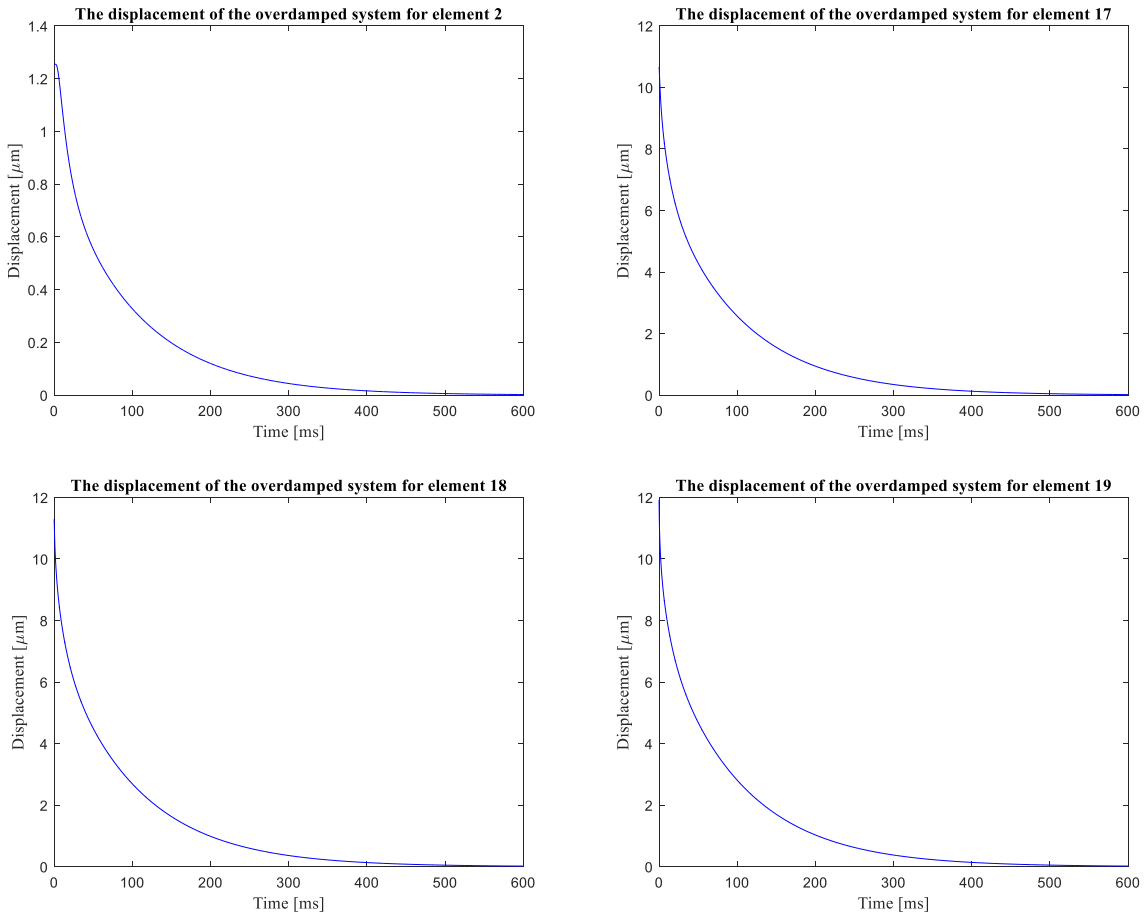


**Figure 5.12:** The overdamped system for elements 2, 17, 18, and 19. Observing that the elements decreases towards zero with the same decreasing time. Furthermore, each element starts at different initial displacement due to Hooke's law.

**Figure 5.13** compares the overdamped system with the experimental results of elements 2, 17, 18, and 19. Similar to experiment I.I, observations indicate that there are no relations between both models. Neither of the elements shows correlation with the overdamped system. This is due to the lack of oscillations in the overdamped system. Obviously, the experimental results indicate that each element oscillates at least ten times before reaching the equilibrium state. This is in contrast to the overdamped system, which decreases without oscillating. However, the last elements, i.e. $i = 17,\ 18,\ \text{and}\ 19,$ show some similarity with the experimental results. This is primarily seen at the initial displacement, whereas both models start approximately at the same position.

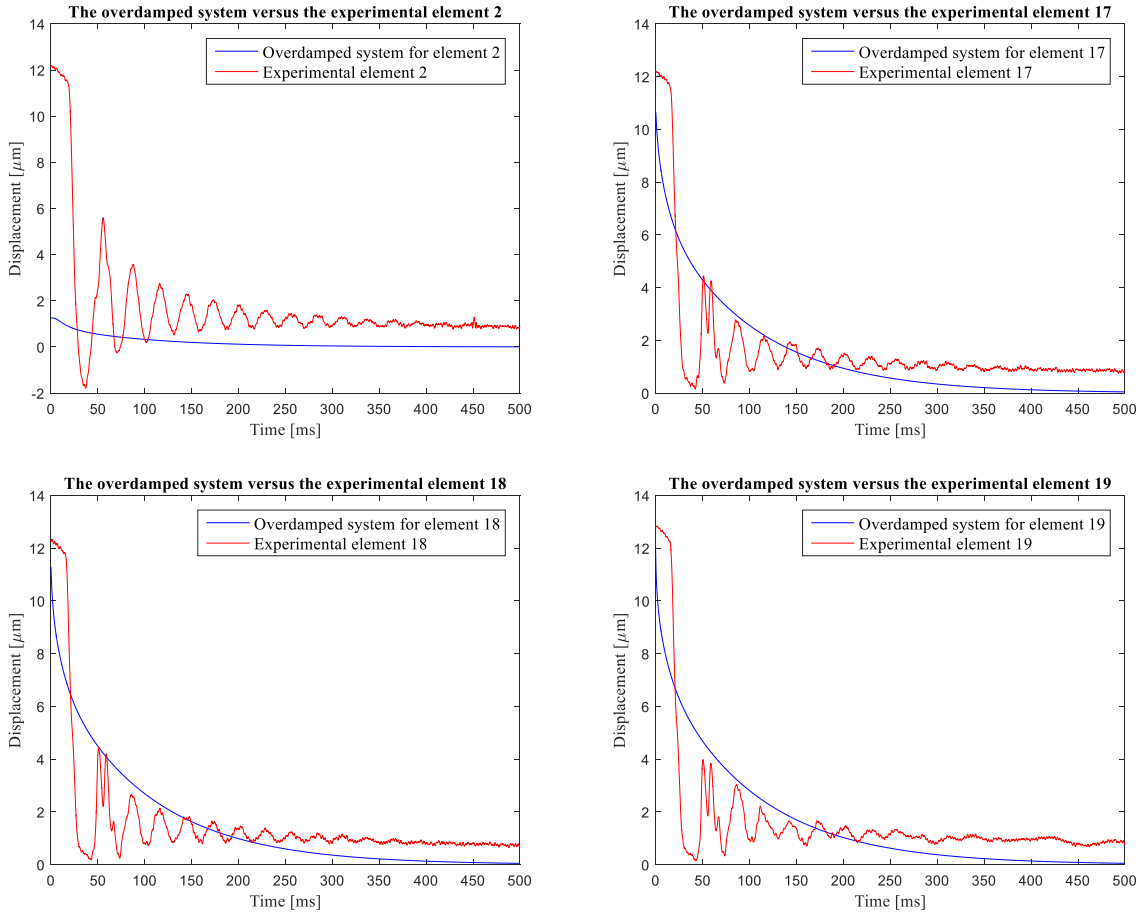


**Figure 5.13:** A comparison of the experimental results and the overdamped system for elements 2, 17, 18, and 19.

The behavior of the underdamped system is illustrated in **figure 5.14**. Again, it can be observed that the elements reaches an equilibrium state at the same time, i.e. at $\sim 70$ ms. Furthermore, observing that the shape of the waves becomes smoother as we move down the vertical drill string, i.e. closer to the element where the weight was loaded on. It is important to notice the response time in element 2. The value is similar to the one calculated for the overdamped system $\left(t_r \approx 0.4 \text{ ms}\right)$ because the period of the longitudinal mode is not affected by the behavior of the system. It depends only on the properties of the material.

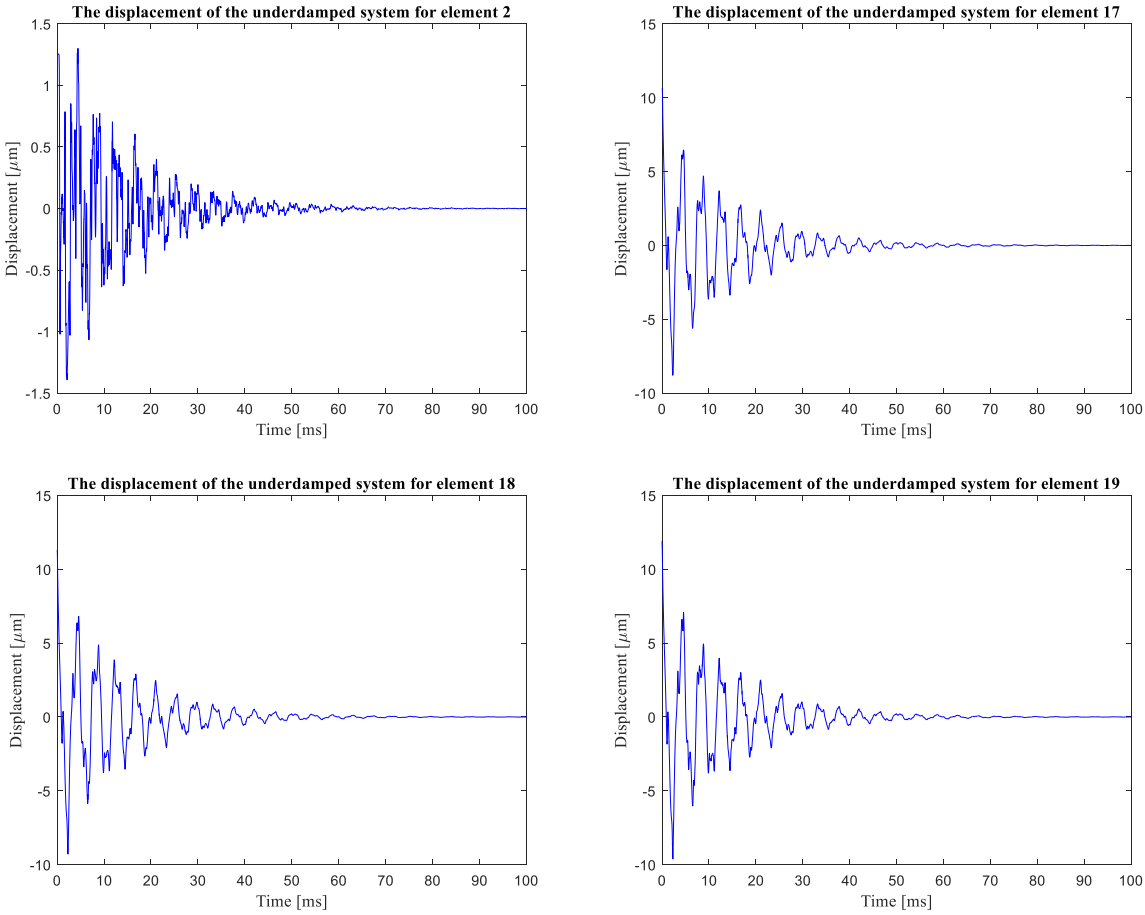


**Figure 5.14:** The underdamped system for elements 2, 17, 18, and 19. Observing that the elements reaches zero at the same time $(\sim 70\ ms)$. Similar to the overdamped system, each element starts at different initial displacement due to Hooke's law.

**Figure 5.15** shows the comparison of the underdamped system and the experimental results for elements 2, 17, 18, and 19. Similar to experiment I.I, there are no clear relation between both systems. The underdamped system oscillates with much higher speed, and hence dies out long before the experimental system. The waves of the underdamped system have a period of $T \approx 4.5$ ms. In comparison, the waves of the experimental system have a period of $T \approx 30$ ms.

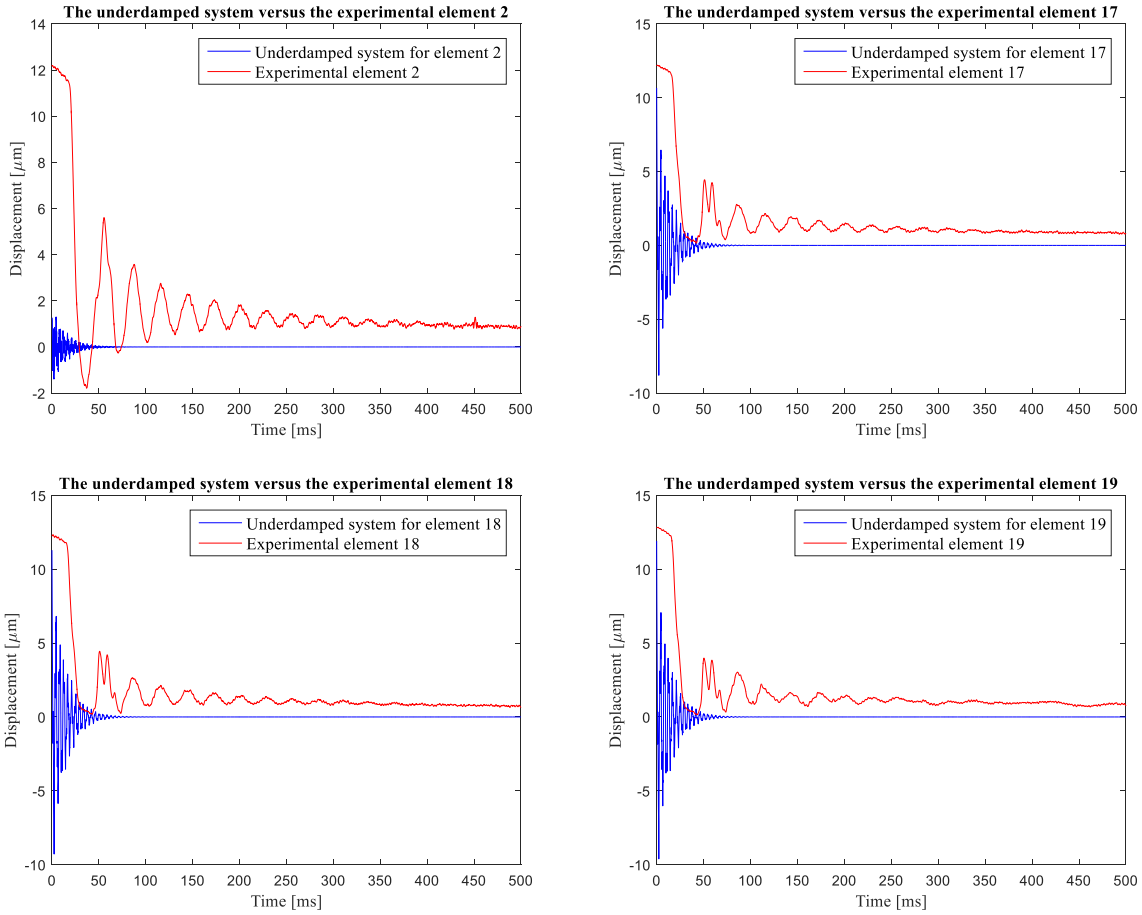


**Figure 5.15:** A comparison of the experimental results and the underdamped system for elements 2, 17, 18, and 19.

### 5.1.3 Experiment I.III

The test segment with 46 elements are evaluated for both overdamped and underdamped systems. The magnitude of the viscosity is adjusted for both systems. Two arbitrary parameters are suggested so that

$$\mu\left[\text{Pa}\times\text{s}\right]=\begin{cases}25 & \text{for overdamped system, i.e.} \quad \varsigma_i=1.59733647\\ 0.015 & \text{for underdamped system, i.e.} \quad \varsigma_i=0.00095840.\end{cases}$$

**Figure 5.16** shows the displacement of the overdamped system for elements 1, 15, 30, and 46 (BHA). Observation indicates that the response time for elements 1 and 15 are $t_r=20$ ms and $t_r=1.7$ ms, respectively. The response time decreases as we move closer to the element where the mass was loaded on.

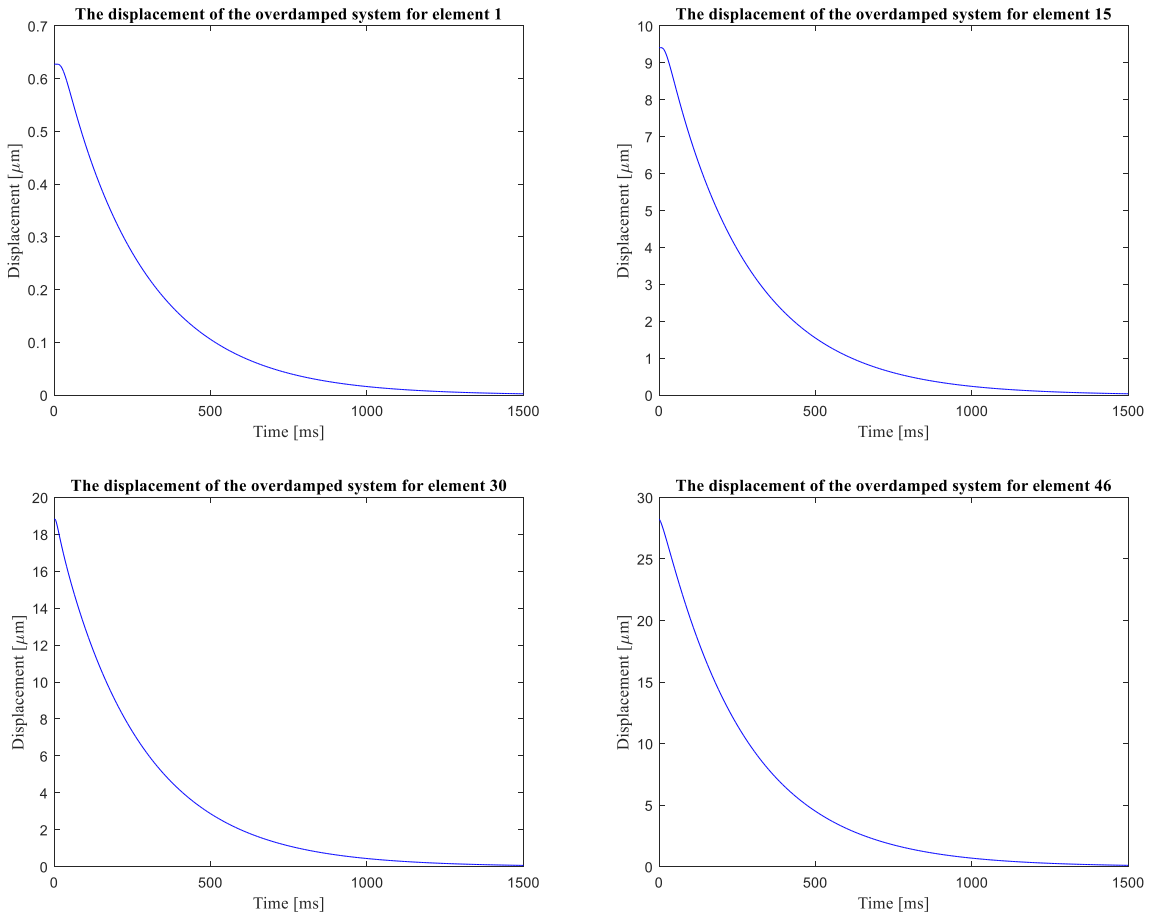


**Figure 5.16:** The overdamped system for elements 1, 15, 30, and 46 (BHA). A similar behavior is observed between the elements. This is particularly seen in decreasing time and the shape of the graphs.

**Figure 5.17** illustrates the displacement of the underdamped system for elements 1, 15, 30, and 46, respectively. Similar to the overdamped system, the response time for elements 1 and 15 are clearly observed. The values are equivalent because the response time is not affected by the behavior of the systems. It depends only on the properties of the material. Further observations of element 1 indicate a wide range of frequencies. Besides the dominating waves with high amplitude and low frequencies, secondary waves are also observed. The frequencies of such waves are high with low amplitudes, and are usually implemented in the dominating waves. This phenomenon tends to die out as we move down the test segment, i.e. closer to the element where the mass was loaded on.

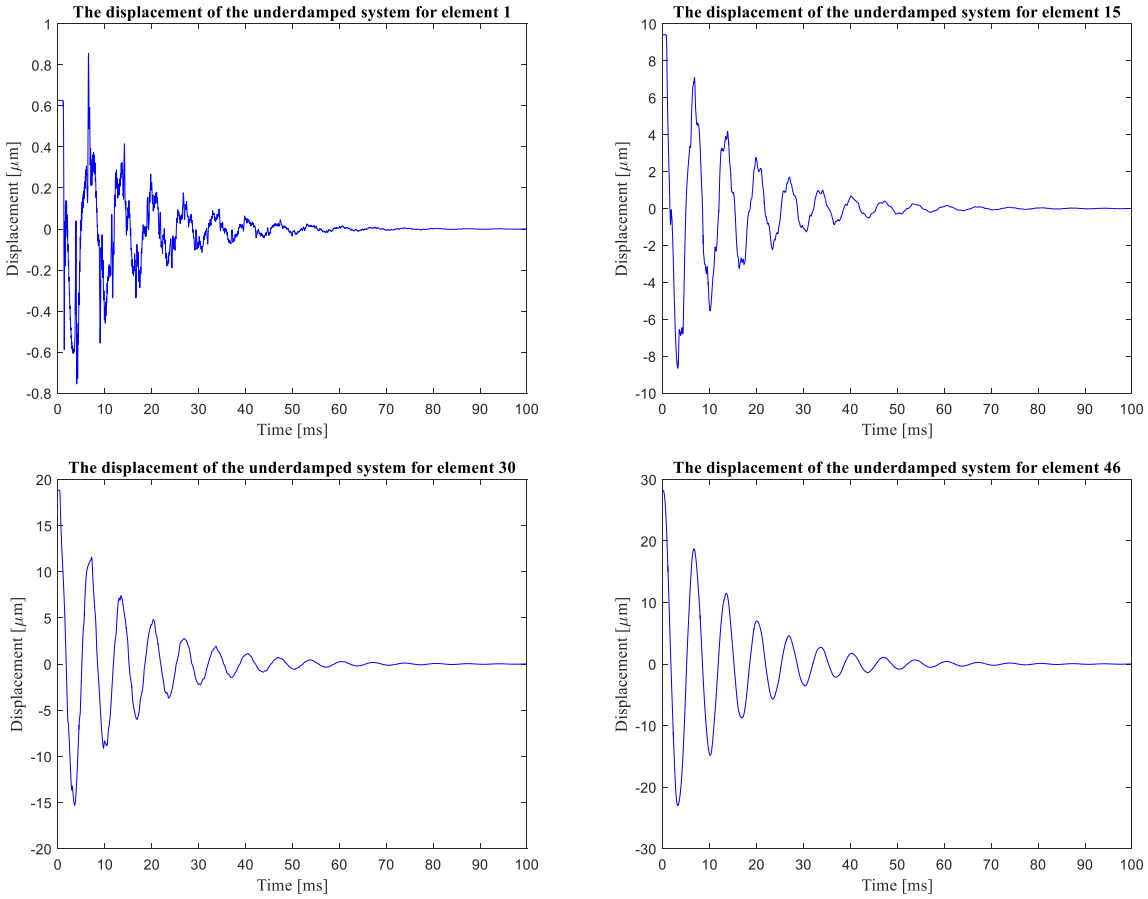


**Figure 5.17:** The underdamped system for elements 1, 15, 30, and 46 (BHA).

## 5.2 Experiment II: The Continuous Drill String

The plexiglas pipe was subjected to a weight of 10 kg, similar to experiment I. **Figure 5.18** shows the displacement of the plexiglas pipe during the entire process.

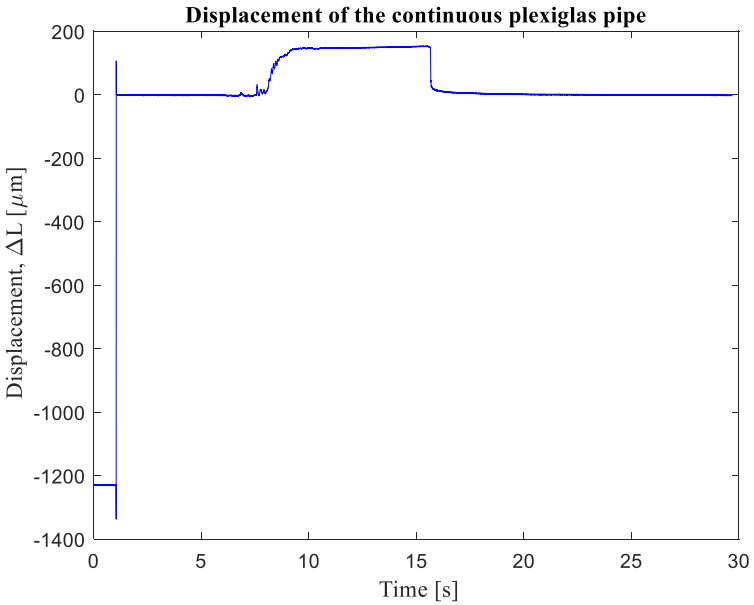


**Figure 5.18:** Displacement of the continuous plexiglas pipe. The figure illustrates the entire process of offset nulling the circuit, loading a mass of 10 kg on the system, instantly remove the mass, and observe the process of returning to initial state.

**Figure 5.19** illustrates the displacement of the plexiglas pipe during, and after the mass was released. Observing that the plexiglas pipe oscillates a few times during its return to initial state.

A comparison between the measured strain for the plexiglas pipe and element 17 from experiment I.II is made in **figure 5.20**. Measured time is converted to a non-dimensional time step. This is done to align both graphs in order to compare them with each other. The data to the plexiglas pipe is therefore shifted along the x-axis by a factor of $-0.134\times10^{5}$. Clearly, both system returns to the initial state at the same time. The plexiglas pipe, however tends to oscillate around the line $y=0$. In comparison, element 17 oscillates around the line $y=1.5$. Moreover, element 17 have larger displacement after the mass applies to both systems, resulting in higher strain. Observing that $\varepsilon_{\text{plexiglas}}=76\times10^{-6}$ and $\varepsilon_{\text{element 17}}=94\times10^{-6}$. This is a result of the additional mass loaded on element 17, which includes elements 18, 19, and BHA.

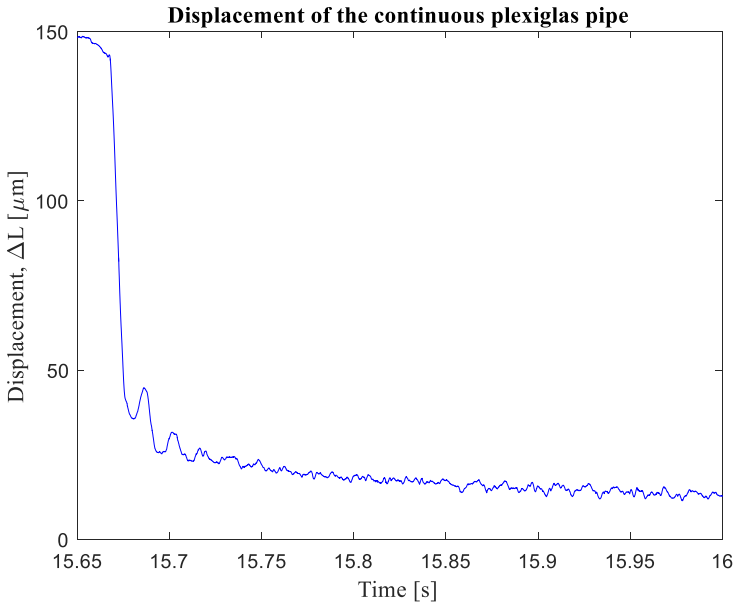


**Figure 5.19:** Displacement of the continuous plexiglas pipe during, and after release of the mass.

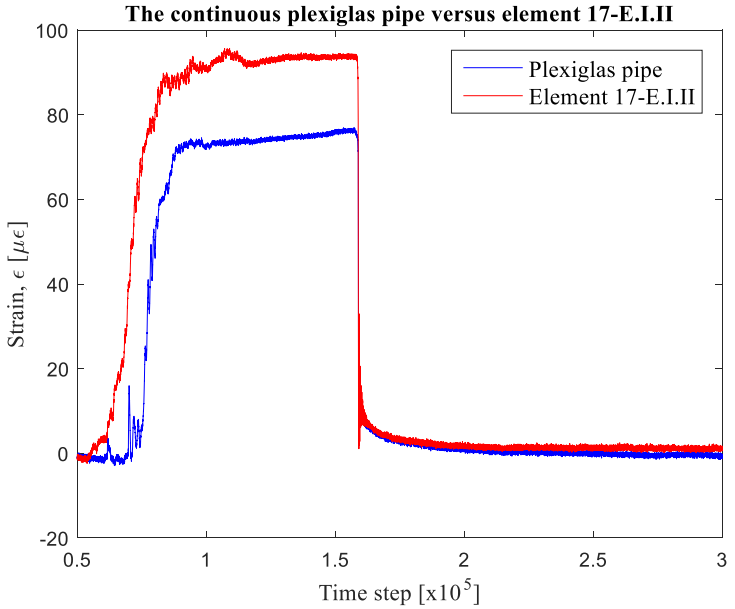


**Figure 5.20:** The continuous plexiglas pipe versus element 17 in experiment I.II. Only strain is considered. The data to the plexiglas pipe has been shifted by a factor of $-0.134\times10^5$ in order to correlate with element 17.

**Figure 5.21** shows the comparison of strain for the plexiglas pipe and elements 2, 17, 18, and 19 of the test segment from experiment I.II. Observing clear correlation between the shape of the graphs. However, the applied mass results in higher strain on the elements. Besides, they tend to oscillate at a higher scale. This is a result of the additional mass loaded on the elements, which includes the weight of the next elements and BHA.

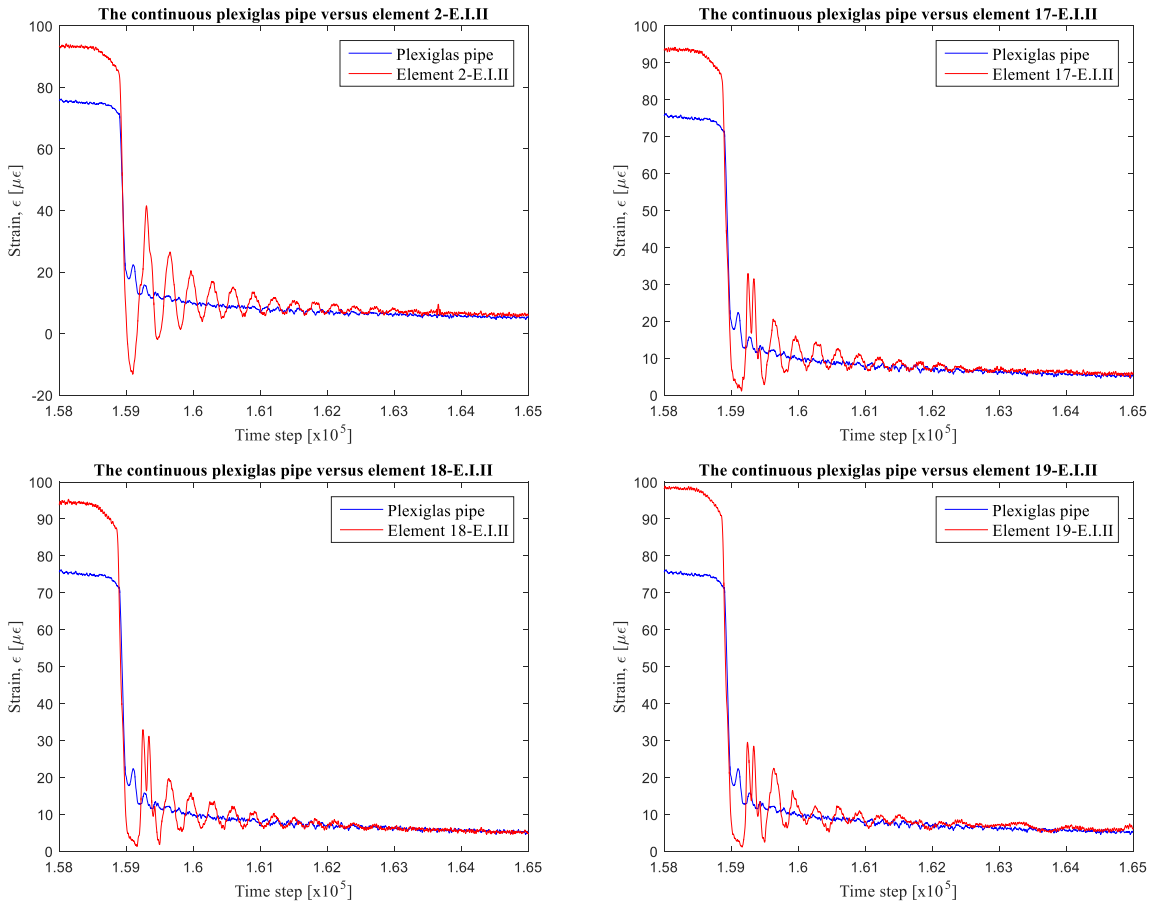


**Figure 5.21:** Strain comparison of the continuous plexiglas pipe and elements 2, 17, 18, and 19. A clear correlation between the shape of the graphs are observed. The graph of the elements oscillates at a larger scale. The additional masses loaded on the elements explains this behavior.

## 5.3 Experiment III: Step Response

The behavior of the test segment is determined by the step, $Q_s$. Therefore, it is necessary to determine a reasonable value for it before further simulations of the model. Because the initial displacement of the elements in the experimental results of section 5.1 was established around $13.0\ \mu m$, it will be a fair assumption to define that $Q_s = 13.0\ \mu m$. This corresponds to a mechanical motor that initiate a displacement change of the first element equivalent to $Q_s$. Two systems have been considered, whereas the first one is the test segment in experiment I.I, and the second one the test segment in experiment I.III. Both systems are assumed underdamped. **Table 5.1** presents both systems with the respective parameters. Notice that the values of viscosity corresponds to the one used in experiments I.I and I.III.

**Table 5.1:** The input parameters of system I and II. Notice that the values of viscosity corresponds to the one used in experiments I.I and I.III.

| System # | Total depth $[m]$ | Elements | Viscosity [Pas] | Damping ratio $\varsigma_i$ |
|---|---|---|---|---|
| I | 0.975 | 6 | 1.5 | 0.01301787 |
| II | 6.375 | 46 | 0.015 | 0.00095840 |

**Figure 5.22** compares both systems for elements $i = 1,\ n-1,$ and $n$. We observe that element 1 oscillates with the smallest amplitude in both systems, an amplitude around $4\ \mu m,$ which is very low compared to the step. However, as element $i$ increases, the amplitude also increases. Obviously, the amplitude of system II is generally higher than system I because of the lower viscosity factor, and therefore lower damping ratio.

By close observation of elements 5 and 45, the response time of the longitudinal mode can be determined. The response time for element 5 is approximately $T_5 = 0.8\ ms,$ and for element 45 $T_{45} = 1.16\ ms.$ This is quite different from the theoretically calculated period of the longitudinal mode in **table 4.2**.

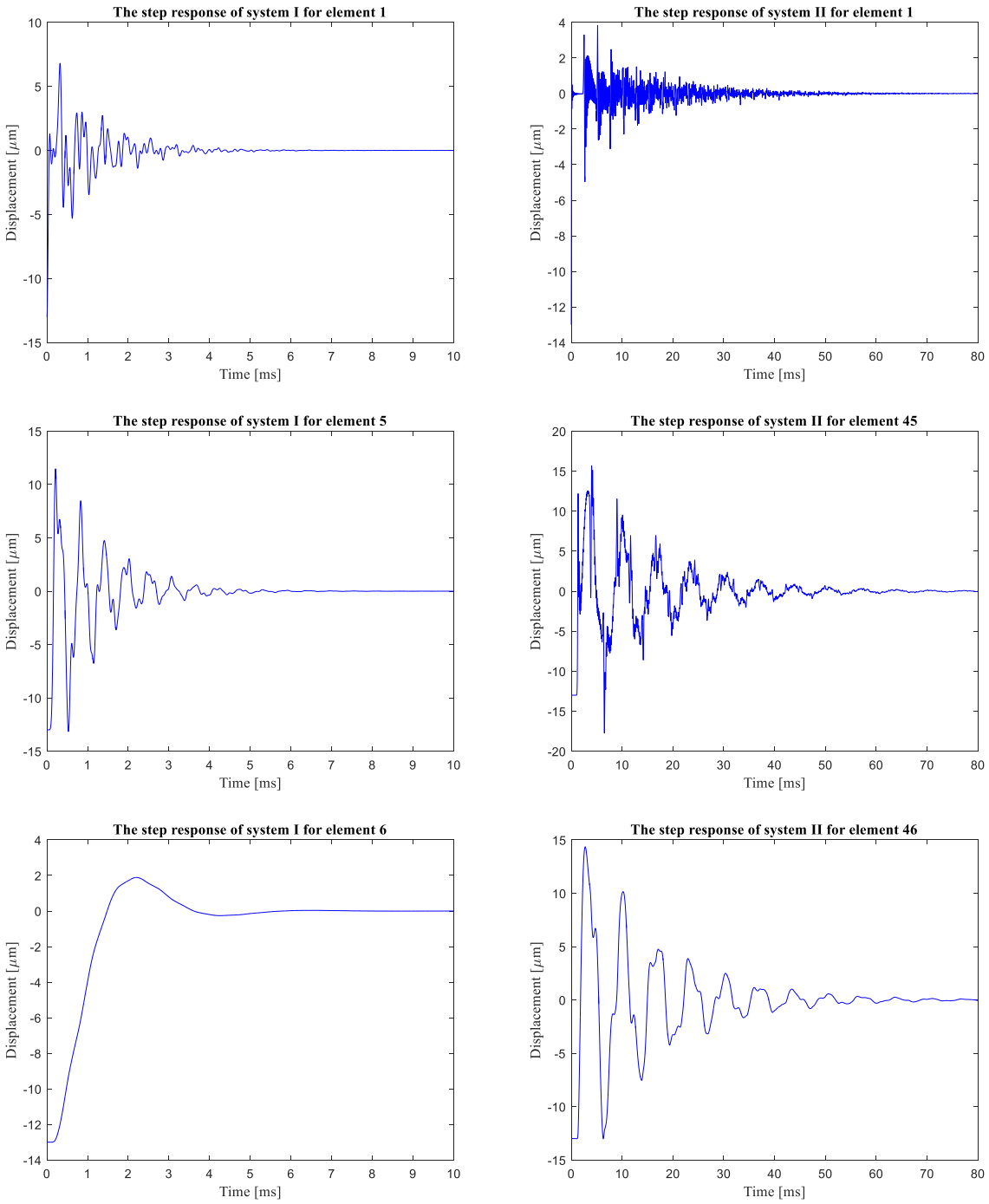


**Figure 5.22:** Comparison of system I and system II for elements $i = 1,\ n-1,$ and $n$.

## 5.4 Experiment IV: Sinusoidal Driving Force

The test segment presented in experiment I.III is chosen for the simulation with the sinusoidal driving force due to the high number of elements. By implementing equation (2.25) and (2.26) in MATLAB, the behavior of the model can be evaluated. Two systems have been considered, as shown in **Table 5.2**. The amplitude factor of both systems is set to $A = 0.01\ \text{m}$. Two different periods have been chosen so that $T_1 = 0.1\ \text{s}$ and $T_2 = 0.001\ \text{s}$ for system I and II, respectively. The relation $\omega = 2\pi / T,$ determines the driving frequency of the system. The driving frequency is therefore $\omega_1 = 20\ \pi$ and $\omega_2 = 2000\ \pi$ for system I and II, respectively. From **Table 5.2** it is clear that both eigenfrequencies and the damping ratios of the elements are independent of the driving frequency. Furthermore, it is important to notice that the viscosity of the test segment has been reduced to $\mu = 0.00015\ \text{Pas}$ for the sake of simplicity.

**Table 5.2:** The comparison of systems I and II with their respective damped eigenfrequencies, $\omega_{d,eigen}$, and the corresponding damping ratios, $\varsigma_i$, for elements 1, 15, 30, and 46. The value of both parameters are independent of the driving frequency.

| **Element #** | **System I** | | **System II** | |
|---|---|---|---|---|
| | $\omega_{d,\text{eigen}}\left[\times 10^4 \text{s}^{-1}\right]$ | $\varsigma_i\left[\times 10^{-5}\right]$ | $\omega_{d,\text{eigen}}\left[\times 10^4 \text{s}^{-1}\right]$ | $\varsigma_i\left[\times 10^{-5}\right]$ |
| 1 | 0.9375 | 75.027 | 0.9375 | 75.027 |
| 15 | 3.3041 | 2.1287 | 3.3041 | 2.1287 |
| 30 | 6.1154 | 1.1502 | 6.1154 | 1.1502 |
| $46\left(\text{BHA}\right)$ | 7.3390 | 0.9584 | 7.3390 | 0.9584 |

**Figure 5.23** shows the plot of both systems. Evidently, the movement of each element reaches steady state at the same time for both systems, which is approximately $t_{set} = 6.55\ \text{s}$. Observations indicate that element 1 have the smallest initial displacement, and that the value increases as we move down the test segment. Hence, element 46 have the highest initial displacement. Furthermore, both systems oscillate with the same amplitude. The only difference is the driving frequency.

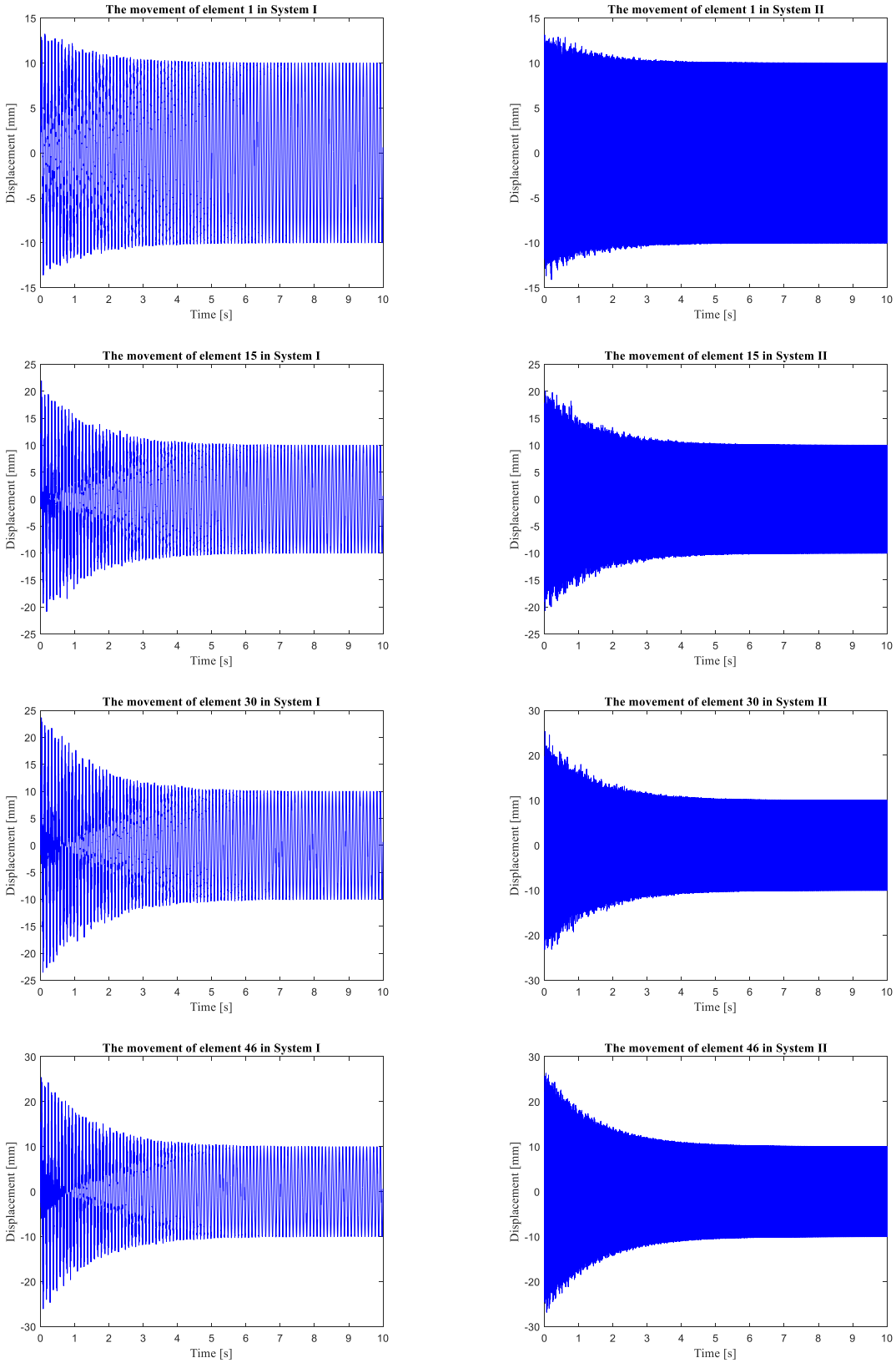


**Figure 5.23:** The movement of the test segment in system I and II for elements 1, 15, 30, and 46. Both systems have the same amplitude and settling time. The only difference is the driving frequency.

# 6 Discussion

## 6.1 Quality of Measured Data

Measurement errors occur in all experimental data. Each part of the experimental model consists of uncertainties, which together affect the measurements. The constructed model, the strain gauges, connecting wires between strain gauges and the amplifier, the amplifier, and even the data filtration process are all sources of uncertainties. Each affects the output data to a different degree. However, the major contributions come from the model itself, strain gauges, and the filtration.

### 6.1.1 Factors That Limit the Validity of the Constructed Model

The model is associated with a number of limitations that arise as a result of its simple design, yet complex behavior. As shown in **figure 4.3**, the model is attached to utility clamps or steel wires in order to prevent element 1 from moving. However, utility clamps tend to oscillate after the mass is released. As a result, the entire system oscillates with the same frequency. This causes a ringing behavior, which appears clearly on the plots of the experimental results. The ringing behavior can be observed in **figure 5.3** for time interval $19.1 \leq t \leq 19.2$. It can also be observed in **figure 5.10** for time interval $14.47 \leq t \leq 14.7$. The effect of such behavior is reduced, but not eliminated after introduction of a steel wire. The contribution of the ringing effect to the overall uncertainty in experimental results is difficult to determine.

Multiple elements, attached together with bolts, behave differently than expected during release of the mass. It was assumed that each element would only oscillate vertically, but observations indicate that the elements “jump up” and swing like a pendulum. This behavior is primarily observed in the last elements, including the BHA. Strain gauges used in the experiments measure only the axial strain, and not the bending strain. Moreover, they are extremely sensitive to movement and temperature changes. As a result, the pendulum behavior interrupts the measurements of the strain gauges. The contribution of this interruption to the overall uncertainty is difficult to determine, but it is known to cause the ringing behavior observed in the experimental results.

Comparison of the continuous plexiglas pipe and the test segment with 20 elements in **figure 5.21** clearly indicates the effect on the ringing behavior. A continuous pipe eliminates the

jumping effect after the release of the weight and reduces the pendulum behavior to a certain degree.

Basically, the model is constructed with an assumption that the steel elements behave like point-masses rather than pipes. Even though the modulus of elasticity of steel is much greater than that of plexiglas, the steel elements will expand. It is difficult to determine the effect of such strain on the experimental results, because no strain measurements were recorded on the steel elements.

### 6.1.2 Noise That Affects the Strain Gauge systems

Section 3.3 provides several techniques to minimize noise that affects the strain gauges. All electrostatic and electromagnetic noises affect the system in different ways. It is therefore difficult, if not impossible, to eliminate the effect of the noise on the experimental results. However, several techniques are introduced to minimize such effects. First, the strain gauges are glued with an insulating adhesive to the plexiglas elements. The adhesive functions as temperature insulator, but can also minimize electrostatic noise to a limited degree. Second, the connecting wires are twisted together as pairs and insulated with a thermoplastic PVC (alternative c in **figure 3.11**). Third, the steel elements are wrapped into an insulating tape in order to reduce its effect on the strain gauges.

### 6.1.3 Effect of the Filtration Process

The filtrating process is an important part of the data evaluation because a significant amount of data is filtered out. Choosing the right filtration method is therefore crucial for the outcome of the experiments. The main argument behind choosing the Savitzky-Golay filtering method is its ability to preserve the high-frequency components of the signal. It is also effective at preserving the shape of the peaks that appear in the measurements. However, choosing an appropriate polynomial order and a frame size is only based on visual observations. As shown in **figure 5.1**, several cases are evaluated in order to produce a convenient filtration. A trial-and-error process leads to choosing a polynomial order of $p = 5$ and a frame size of $N = 51$. This combination filters most of the noise, and at the same time, preserves the overall shape of the curve.

Further, one may argue that the trial-and-error process, based only on visual observations, is a highly simplified method to filter out the noise. Such method will probably filter out some of

the high-frequency signals along with the noise. This may change the understanding of the experimental results. However, because of the lack of a systematic method to determine and measure the sources of noise, it is difficult to implement other more effective methods.

## 6.2 Quality of the Analytical Model

The lumped element model approximates the spatially distributed drill string by a topology of discrete entities. This allows the derivation of a simple analytical model that describes axial vibrations in a vertical drill string. However, the model presents a significant simplification of the continuous drill string. There are three key factors in the analytical model that must be analyzed.

The model assumes that each element consists of a point mass and a spring, whereas all the mass is concentrated in one point mass. This simplifies the physical behavior of the element and allows neglecting its size and shape. Thus, neglecting the moment of inertia and rotational properties. It is, however, difficult to find a material that satisfies the properties of a point mass. The use of a steel pipe as a point mass limits this assumption because each steel pipe has a length and shape. Therefore, the steel pipes undergo strain during loading of the mass. Moreover, because the steel pipes are connected with bolts to the plexiglas elements, there is a high possibility that they take up angular momentum. The effect of this is unknown because measurements of bending stress are not made.

Further, the analytical model assumes that the sum of all external friction forces is integrated into the viscous friction force. Clearly, equation (2.14) from section 2.2.1 shows that the magnitude of the viscous friction force varies only with the viscosity of the liquid. This means that the viscosity parameter behaves more like the friction factor of the system rather than a parameter related only to the viscous fluid. It is therefore necessary to adjust the magnitude of the viscosity in order to satisfy the requirements of the damping ratio. This adjustment, however, resulted in unrealistically high viscosity factors, especially in the overdamped system.

For the test segment in experiment I.I, a viscosity factor of $\mu = 180\,\mathrm{Pa}\times\mathrm{s}$ is determined. Theoretically, it requires a heavy viscous fluid with properties close to peanut butter in order to replicate such high damping ratio (Liquid Control, 2016). However, it is observed that the viscosity factor reduces as the number of elements increases. This is seen in the test segments in experiment I.II and I.III, where the viscosity factor is reduced to $\mu = 55\,\mathrm{Pa}\times\mathrm{s}$ and $\mu = 25\,\mathrm{Pa}\times\mathrm{s},$ respectively, in order to create the same damping ratio.

In addition, determining the size of the "invisible" borehole is crucial for the outcome of the damping ratio. The argument behind determining the size of the borehole is the relation between a $9\ ⅝''$ borehole drilled with a $5\ ½''$ drill string. This resulted in an $OD = 52.5\ \text{mm}$ for the borehole. Increasing the size of the borehole, for the same viscosity, reduces the value of the damping ratio, and vice versa.

### 6.3 Further Work

Further experiments should be developed for the transient state scenario in order to verify the initial conditions. Experiment I.III should be conducted alongside further experiments where the number of elements is increased, i.e. $i = 100,\ 150,\ 200$ etc. Conducting the experiment in an actual borehole with a viscous fluid should be considered. A combination of a sufficient number of elements and an actual borehole would result in an appropriate choice of the viscous fluid. Experimenting with different loaded mass should also be considered.

The ringing behavior that occurs after release of the mass should be further examined. Necessary measures should be implemented in order to either minimize its effect, or determine its magnitude in order to adjust the data. Such measures include the use of a better equipment to attach the test segment to, i.e. steel beams or a concrete ceiling. This will eliminate the oscillations of the entire test segment after the release of the mass. A better mechanism to attach and release the loaded mass of the last element should also be considered. If necessary, a continuous pipe should be considered rather than multiple elements.

Furthermore, plexiglas elements should be replaced by metal pipes, for example aluminum. Plexiglas pipes undergo elastic deformation at small strain, but the way they behave cannot completely replicate the behavior of a metal pipe. It is important to choose pipes with small thickness when metals like aluminum is considered. This will allow the pipes to expand to a greater extent, and therefore present a better replication of a spring. On the other hand, the thickness of the steel pipes should be increased in order to maintain the mass ratio between steel and aluminum pipes.

Experiments related to scenario 1 and 2 should be performed in accordance with the guidelines given in this paper. Regarding the step response, it is necessary to implement a sufficient amount of elements in order to increase the response time of the last several elements. Furthermore, this will simplify the process of designing a mechanical motor which can generate a displacement change faster than the response time of the last elements.

If the validity of the model is proven for these particular scenarios, then further steps is to implement the theoretical model for more sophisticated geometries, such as deviated wells. Development of the model is based on a simple geometry, and must be expanded in order to apply to different geometries. Further expansion must include parameters such as Coulomb's friction between the borehole and the drill string, and angular momentum at the connection points between the elements. Because of the deviation, Newton's way of approaching the solution complicates the process. Therefore, more simplified methods, such as an Euler-Lagrange method should be considered.

# 7 Conclusion

A study of axial vibrations in a vertical drill string is conducted using a $n$- coupled spring-mass-damper model. The main motivation behind this is to describe the axial vibrations using a simple mathematical model that allows for a substantial interpretation and application of control theory. In other words, the analytical model used to describe test segments in this thesis can easily apply to other vertical drill string models, with a few adjustments. For this reason, this thesis investigates to what extent the lumped element model can be used to replicate and predict axial vibrations in a vertical drill string.

It is found that the lumped element model cannot be verified on the basis of a comparison of the experimental results and the analytical model for the transient state. The analytical model cannot replicate and predict axial vibrations in a vertical drill string. Further, the comparison of test segments and the analytical model has led to the following two additional conclusions.

Firstly, there is no correlation between the underdamped system and test segments with 6 and 20 elements, respectively (experiment I.I and I.II). The same applies to the overdamped system and the test segment with 6 elements. However, a weak correlation between the overdamped system and the test segment with 20 elements is observed for the last three elements.

Secondly, a ringing behavior is observed in the test segments, which causes some of the oscillations that occurs after release of the mass. The effect of this is minimized by using a continuous drill string (experiment II) or by attaching the test segment to a firm object.

The experiments on the test segments are conducted on the basis of a simplified model. This is an oversimplification of the real life drill string. As a direct consequence of such choice of model, the study encountered three main limitations.

Firstly, the conclusions reached in this thesis may not necessarily apply to different models with complex geometries. Such models give a better representation of a real life drill string. Hence, the study should be extended to more complex geometries.

Secondly, the experiments only account for the transient state of the system. Physical experiments with step response and sinusoidal driving forces should also be conducted in accordance with the guidance given in this paper.

Finally, the number of elements in the test segment is inversely proportional to the damping ratio. A small number of elements requires an extremely high viscosity fluid in the borehole.

An increase in the number of elements in the test segment will alleviate this requirement and bring simulations closer to reality. The borehole size is also inversely proportional to the damping ratio. Therefore, a sufficient high number of elements in a test segment should be used in future experiments.

This thesis admires the previous research efforts by others. It shows that there is still much to be done to substantiate the use of a lumped element model to replicate and predict axial vibrations in a vertical drill string. Several improvements are proposed to pave the way for future research in this area.

## Bibliography


Agilent Technologies. (1999).
"*PRACTICAL STRAIN GAGE MEASUREMENTS"*.
[Online] Available at:
http://www.omega.co.uk/techref/pdf/straingage_measurement.pdf.
[Accessed 20 October 2015].

All About Circuits. (2015).
*"Strain Gauges: Chapter 9 - Electrical Instrumentation Signals – Electronics Textbook"*. [ONLINE] Available at:
http://www.allaboutcircuits.com/textbook/direct-current/chpt-9/strain-gauges/.
[Accessed 20 October 2015].

Altuglas International. (2008).
*"Plexiglas – CELL-CAST ACRYLIC SHEET"*. [ONLINE] Available at:
http://www.associatedplastics.com/forms/acrylic_plastics_data.pdf.
[Accessed 25 October 2015].

Azar, J. J. & Samuel, G. R. (2007).
*"Drilling Engineering"*. 1st ed. USA: PennWell Corporation. 335.

Bailey, J. J., & Finnie, I. (1960).
*"An Analytical Study of Drill-String Vibration"*. Journal of Engineering for Industry, Transactions of the ASME, 82(2), 122-128.

Bernat, B. & Bernat, H. (1997).
*"Mechanical oscillator frees stuck pipe strings using resonance technology."*
[ONLINE] Available at:
http://www.ogj.com/articles/print/volume-95/issue-44/in-this-issue/drilling/mechanical-oscillator-frees-stuck-pipe-strings-using-resonance-technology.html.
[Accessed 12 December 2015].

Bilbao, S. (2014).
*"Lumped vs. Distributed Systems"*. [ONLINE] Available at:
https://ccrma.stanford.edu/~jos/NumericalInt/Lumped_vs_Distributed_Systems.html.
[Accessed 26 May 2016].

ChinaICMart. (2012).
*"INA125 Selling Leads, INA125 Datasheet PDF"*. [ONLINE] Available at:
http://www.chinaicmart.com/series-INA/INA125.html.
[Accessed 28 April 2016].

Choudhary, N. & Verma, R. (2011).
*"Laser Systems and Applications"*. New Delhi: PHI Learning Private Limited. 136-138.

Chu, H., Shah, G. & Macall, T. (2011).
*"Linear Homogeneous Ordinary Differential Equations with Constant Coefficients".*
eFunda. [ONLINE] Available at:
http://www.efunda.com/math/ode/linearode_consthomo.cfm.
[Accessed 18 November 2015].

Classltd. (2013).
*"Class Instrumentation Ltd Ultrasonic Sound Velocity Chart"*. [ONLINE] Available at:
http://www.classltd.com/res/sound%20velocity%20chart.pdf.
[Accessed 05 May 2016].

Dupriest, F. E. (2006).
*"Comprehensive Drill-Rate Management Process To Maximize Rate of Penetration"*. In: SPE paper 102210. Texas: Society of Petroleum Engineers.
Dupriest, F. E. et al. (2010).
*"Borehole Quality Design and Practices to Maximize Drill Rate Performance"*. In: SPE paper 134580. Florence: Society of Petroleum Engineers.
Efstathiou, C. E. (2000).
*"Signal Smoothing Algorithms"*. [ONLINE] Available at: http://www.chem.uoa.gr/applets/appletsmooth/appl_smooth2.html. [Accessed 30 May 2016].
Electrical4u. (2015).
*"Time Response of Second-Order Control System"*. [ONLINE] Available at: http://www.electrical4u.com/time-response-of-second-order-control-system/. [Accessed 12 November 2015].
ETB. (2015).
*"Metals and Alloys - Densities"*. [ONLINE] Available at: http://www.engineeringtoolbox.com/metal-alloys-densities-d_50.html. [Accessed 27 November 2015].
ETB. (2015).
*"Modulus of Elasticity or Young's Modulus - and Tensile Modulus for some common Materials"*. [ONLINE] Available at: http://www.engineeringtoolbox.com/young-modulus-d_417.html. [Accessed 27 November 2015].
Gatti, P., L. & Ferrari, V. (1999).
*"Applied Structural and Mechanical Vibrations"*. ISBN 0-419-22710-5. London: E & FN Spon. 1st edition.
Ghasemloonia, A., Rideout, D. G., & Butt, S. D. (2015).
*"A review of drillstring vibration modeling and suppression methods"*. Journal of Petroleum Science and Engineering. Volume 131. 150-164.
Hassan, R. (2015).
*"Simulation of Axial Drillstring Vibrations using an Analytical Model"*. Project report submitted in the subject Drilling technology specialization project (TPG4520) at Norwegian University of Science and Technology, Trondheim on 15 December 2015.
Hovda, S. (2015).
*"Drillstring dynamics"*, lecture notes distributed in High Deviation Drilling (TPG4215) at Norwegian University of Science and Technology, Trondheim on 30 October 2015.
Hovda, S. (2016).
*"Gibbs-like Phenomenon Inherent in a Lumped Element Model of a Rod"*. Preprint submitted to Journal of Sound and Vibration on February, 18 2016.
Judson, T., W. (2008).
*"Math 106. Lecture 23 Forced Damped Harmonic Oscillators"*. [Online] Available at: http://isites.harvard.edu/fs/docs/icb.topic251677.files/notes23.pdf. [Accessed 11 November 2015].
Kreyszig, E. (2006).
*"Advanced Engineering Mathematics"*. ISBN: 978-0-471-72897-9. Singapore: John Wiley & Sons, Inc. 9th edition. P. 333-363.
Liquid Control. (2016).
"*VISCOSITY*". [ONLINE] Available at: http://www.vp-scientific.com/pdfs/www.liquidcontrol.com_eToolbox_viscosity.pdf. [Accessed 6 June 2016].

LMNO. (2015).
*"Gas Viscosity Calculator".* [ONLINE] Available at:
http://www.lmnoeng.com/Flow/GasViscosity.php.
[Accessed 29 November 2015].
Macpherson, J. D., Mason, J. S. & Kingman, J. E. E. (1993).
*"Surface Measurement and Analysis of Drillstring Vibrations while Drilling"*. In: SPE/IADC paper 25777. Netherlands: Society of Petroleum Engineers.
Márquez, M. B. S. et al. (2015).
*"Analysis and Control of Oilwell Drilling Vibrations".* ISBN: 978-3-319-15747-4 (eBook). Switzerland: Springer International Publishing AG. P. 8-10, 24.
MathWorks. (2016).
*"sgolay"*. [ONLINE] Available at:
http://se.mathworks.com/help/signal/ref/sgolay.html. [Accessed 30 May 2016].
Morin, D. (2015).
*"Chapter 1; Oscillations"*. [Online] Available at:
http://www.people.fas.harvard.edu/~djmorin/waves/oscillations.pdf.
[Accessed 11 November 2015].
Morrison, F., A. (2011).
*"The Equation of Continuity and the Equation of Motion in Cartesian, cylindrical, and spherical coordinates"*. [Online] Available at:
http://www.chem.mtu.edu/~fmorriso/cm310/Navier.pdf.
[Accessed 13 November 2015].
NI. (2012).
*"Making Accurate Strain Measurements"*. [Online] Available at:
http://www.ni.com/white-paper/6186/en/.
[Accessed 27 October 2015].
NI. (2014).
*"Measuring Strain with Strain Gages"*. [Online] Available at:
http://www.ni.com/white-paper/3642/en/.
[Accessed 19 October 2015].
NI. (2015).
*"How Is Temperature Affecting Your Strain Measurement Accuracy?"*.
[Online] Available at:
http://www.ni.com/white-paper/3432/en/.
[Accessed 22 October 2015].
NI. (2015).
*"USER GUIDE: NI USB-6008/6009, Bus-Powered Multifunction DAQ USB Device"*.
[Online] Available at:
http://www.ni.com/pdf/manuals/375295a.pdf.
[Accessed 26 April 2016].
NI. (2016).
*"Measuring Strain with Strain Gages"*. [Online]. Available at:
http://www.ni.com/white-paper/3642/en/.
[Accessed 08 June 2016].
NSMarket. (2016).
*"HBM-1-XY11-6/120 Rosette Strain gauge for ferritic steel"*. [ONLINE] Available at:
https://www.nsmarket.gr/en/index/products/HBM_SrainGauges?row=914.
[Accessed 25 April 2016].

Omega. (2015).
*"The Strain Gage"*. [ONLINE] Available at:
http://www.omega.com/literature/transactions/volume3/strain2.html.
[Accessed 26 October 2015].
PubChem Compound Database. (2015).
*"METHYL METHACRYLATE"*. [ONLINE] Available at:
http://pubchem.ncbi.nlm.nih.gov/compound/6658#section=Top.
[Accessed 06 December 2015].
Savitzky, A. & Golay, M. (1964).
*"Smoothing and Differentiation of Data by Simplified Least Squares Procedures"*.
[ONLINE] Available at: http://pubs.acs.org/doi/pdf/10.1021/ac60214a047.
[Accessed 30 May 2016].
SEESL. (2015).
*"Figure 3.7.1.3-1: Bonded Metallic Strain Gauge"*. [ONLINE] Available at:
http://nees.buffalo.edu/docs/labmanual/HTML/Chapter%203_files/image047.png.
[Accessed 19 October 2015].
Smyth, T. (2015).
*"Music 270a: Modulation"*. [ONLINE] Available at:
http://musicweb.ucsd.edu/~trsmyth/modulation/modulation_4up.pdf.
[Accessed 16 April 2016].
Taylor, R. L. & Zhu, J. Z. (2005).
*"The Finite Element Method: Its Basis and Fundamentals"*. ISBN: 0-7506-6320-0.
Oxford: Elsevier Butterworth-Heinemann. Sixth edition. P. 1-13.
TI. (1998).
*"INSTRUMENTATION AMPLIFIER With Precision Voltage Reference"*.
[ONLINE] Available at: http://www.ti.com/lit/ds/symlink/ina125.pdf.
[Accessed 25 April 2016].
Tseng, Z., S. (2008).
*"Mechanical Vibrations"*. [Online] Available at:
http://www.math.psu.edu/tseng/class/Math251/Notes-MechV.pdf.
[Accessed 10 November 2015].
Vishay Precision Group. (2013).
*"Noise Control in Strain Gage Measurements. Strain Gages and Instruments"*.
[Online] Available at: http://www.vishaypg.com/docs/11051/tn501.pdf.
[Accessed 26 October 2015].
Vishay Precision Group. (2013).
*"Shunt Calibration of Strain Gage Instrumentation"*. [ONLINE] Available at:
http://www.vishaypg.com/docs/11064/tn514.pdf.
[Accessed 27 October 2015].
Weisstein, E., W. (2015).
*"Critically Damped Simple Harmonic Motion"*. [ONLINE] Available at:
http://mathworld.wolfram.com/UnderdampedSimpleHarmonicMotion.html.
[Accessed 29 October 2015].
Weisstein, E., W. (2015).
*"Underdamped Simple Harmonic Motion"*. [ONLINE] Available at:
http://mathworld.wolfram.com/UnderdampedSimpleHarmonicMotion.html.
[Accessed 29 October 2015].

## Nomenclature and Abbreviations

**Roman Symbols**

| | |
|---|---|
| $A$ | Amplitude of the oscillations for an underdamped system |
| $A_c$ | Cross-sectional area of an element |
| $c$ | Damping factor of the viscous piston |
| $c_s$ | Speed of sound in a specific material |
| $C_1$ | Constant related to the ordinary solution of the homogeneous differential equation |
| $C_2$ | Constant related to the ordinary solution of the homogeneous differential equation |
| $\mathbf{C}$ | $n \times n$ diagonal matrix representing the spring constant of elements |
| $\mathbf{C}_{\mathbf{I.C.}}$ | $n \times 1$ vector describing the initial conditions of the transient state |
| $D$ | Diameter of a solid body |
| $\mathbf{D}$ | $n \times n$ diagonal matrix of eigenvectors |
| $E$ | Modulus of elasticity (Young's modulus) |
| $f$ | Frequency |
| $\mathbf{f}$ | Vector with dimensions $n \times 1$ representing the driving force of the system |
| $F_s$ | Spring force, given by Hooke's law, acting on a point mass |
| $g$ | Gravity of Earth |
| $\mathbf{g}$ | Vector with dimensions $n \times 1$ representing the gravity force of all elements |
| $i$ | Element number |
| $\mathbf{I}$ | Identity vector with dimensions $n \times 1$ |
| $k$ | Spring constant given by Hooke's law |
| $k_i$ | The spring constant of the spring that is connected above element $i$ |
| $\mathbf{k}$ | $n \times n$ tridiagonal matrix representing spring constants of $n$ springs |
| $L$ | Length of a test segment |
| $L_i$ | Length of element $i$ |
| $L_0$ | Initial length of element $i$ |
| $m$ | Mass of an element/point mass |
| $m_i$ | Mass of element $i$ |
| $m_n$ | Mass of element $i = n$ |
| $\mathbf{M}$ | Diagonal matrix with dimensions $n \times n$ representing the mass of all elements |

| | |
|---|---|
| $n$ | Number of elements in the spring-mass-damper model |
| $n_r$ | Refractive index of a material |
| $N$ | Frame size, i.e. data window during filtration of a data set |
| $p$ | Polynomial order |
| $q$ | Displacement of an element/point mass |
| $q_0$ | Initial displacement of element/point mass, i.e. equilibrium position |
| $q_i$ | Displacement of element $i$ |
| $\dot{q}$ | Velocity of an element |
| $\ddot{q}$ | Acceleration of an element |
| $Q$ | Position of origin for the one-dimensional coordinate system (assumed at drill deck) |
| $Q_i$ | Initial displacement of element $i$ for the transient state |
| $Q_s$ | Initial displacement of element 1 as a result of the step |
| $Q_d$ | Amplitude of the driving force |
| $\mathbf{Q}$ | $n \times 1$ vector representing Initial displacement of all elements for the transient state |
| $r$ | Variable forming the characteristic equation of a 2nd order differential equation |
| $R_{hole}$ | Radius of the borehole |
| $R$ | Electrical resistance (only chapter 3) |
| $R_G$ | Resistance change measured by a strain gauge (only chapter 3) |
| $R_i$ | The external forces/viscous friction force acting on element $i$ |
| $R_{wire}$ | Wire resistance in a Wheatstone bridge (only chapter 3) |
| $t$ | Time |
| $T$ | Period of a pressure wave/longitudinal mode |
| $u_i$ | Velocity of drilling fluid at element $i$ |
| $v_p$ | Velocity of the drill string when POOH |
| $\mathbf{v}$ | Arbitrary, nonzero and real column vector for the generalized eigenvalue problem |
| $V_{EX}$ | Excitation voltage of a Wheatstone bridge |
| $V_o$ | Output voltage of a Wheatstone bridge |
| $V_{offset}$ | Offset voltage |
| $V_r$ | Voltage ratio between voltage change in the circuit and excitation voltage |
| $\mathbf{V}$ | $n \times 1$ vector of eigenvectors |

| | |
|---|---|
| $\mathbf{w}$ | $n \times 1$ vector representing the gravitational force caused by a loaded mass |
| $x$ | Displacement of an element in the new coordinate system |
| $x_i$ | Displacement of element $i$ |
| $x_o$ | Transient/ordinary solution of $n$ - coupled spring-mass-damper system |
| $x_p$ | Steady-state/particular solution of $n$ - coupled spring-mass-damper system |
| $\dot{x}$ | Velocity of an element |
| $\ddot{x}$ | Acceleration of an element |
| $\mathbf{y}$ | $n \times 1$ vector representing the displacement of all elements |
| $\dot{\mathbf{y}}$ | $n \times 1$ vector representing the velocity of all elements |
| $\ddot{\mathbf{y}}$ | $n \times 1$ vector representing the acceleration of all elements |

**Greek Symbols**

| | |
|---|---|
| $\alpha$ | Ratio between outer radius of the drill string and radius of the borehole |
| $\alpha_i$ | Ratio of the outer radius of the drillpipe and radius of the borehole |
| $\alpha_n$ | Ratio of the outer radius of the drill collar and radius of the borehole |
| $\alpha_i R_{hole}$ | Outer radius of the drill string at element $i$ |
| $\beta$ | Buoyancy factor |
| $\gamma_{i,1}$ | Variable representing $-\varsigma_i \omega_i - \omega_i \sqrt{\varsigma_i^2 - 1}$ in the transient solution |
| $\gamma_{i,2}$ | Variable representing $-\varsigma_i \omega_i + \omega_i \sqrt{\varsigma_i^2 - 1}$ in the transient solution |
| $\gamma_j$ | Phase shift for element $j = i$ |
| $\Gamma_j$ | Amplification factor for element $j = i$ |
| $\delta$ | Change in the value of a variable |
| $\Delta$ | Change of any changeable quantity |
| $\Delta L$ | Change in length of a material |
| $\Delta R$ | Change in resistance (only chapter 3) |
| $\varepsilon$ | Strain |
| $\varepsilon_T$ | Strain in transverse direction of the applied force |
| $\lambda$ | Scalar used in the eigenvalue decomposition |
| $\mu$ | Viscosity of drilling fluid |
| $\nu$ | Poisson's ratio |

| | |
|---|---|
| $\nu_{plexiglas}$ | Poisson's ratio, plexiglas |
| $\nu\varepsilon$ | Bending strain in the transverse direction of applied force |
| $\sigma$ | Axial stress acting on a cross-sectional area |
| $\varsigma$ | Damping factor/ratio |
| $\varsigma_i$ | Damping factor/ratio of element $i$ |
| $\Sigma$ | Summation operator |
| $\tau_w$ | Shear stress at wellbore wall |
| $\phi$ | Phase shift |
| $\phi_i$ | Phase shift of element $i$ |
| $\psi_i$ | Induced phase shift relative to the driving force, for element $i$ |
| $\Psi_{ij}$ | Variable summarizing the amplitudes of all elements for sinusoidal driving force |
| $\Psi_{kj}$ | Variable summarizing the amplitudes of all elements for sinusoidal driving force |
| $\omega$ | Angular frequency of the driving force |
| $\omega_0$ | Natural frequency of a system, i.e. frequency of an undamped harmonic oscillator |
| $\omega_d$ | Damped angular frequency of a system |
| $\omega_{d,i}$ | Damped angular frequency of element $i$ |
| $\omega_i$ | Natural angular frequency of element $i$ |
| $\Omega$ | Unit ohm |

**Abbreviations**

| | |
|---|---|
| AC | Alternating current |
| AI | Analog input channel |
| ADC | Analog to digital converter |
| AO | Analog output channel |
| BB | Burr-Brown (integrated circuits manufacturer) |
| BHA | Bottom hole assembly |
| DAQ | Data acquisition |
| DC | Direct current |
| DIO | Digital input/output channel |
| GF | Gage factor |

| | |
|---|---|
| GND | Ground |
| HBM | Hottinger Baldwin Messtechnik GmbH (strain gauge manufacturer) |
| HWDP | Heavyweight drillpipe |
| ID | Inner diameter |
| INA | Instrumentation amplifier |
| LabVIEW | Laboratory Virtual Instrument Engineering Workbench |
| MATLAB | Matrix Laboratory |
| MD | Measured depth |
| NI | National Instruments |
| OD | Outer diameter |
| POOH | Pull out of the hole, i.e. to remove the drill string from the wellbore |
| PVC | Polyvinyl Chloride – a thermostatic insulator |
| ROP | Rate of penetration |

# Appendices

## A Viscous Friction Force

The viscous friction force acts in opposite direction of the movement of the drill string. $R_i$ is the viscous force acting on element $i$ of the drill string. **Figure A-1** illustrates a moving drill string when POOH. The velocity profile of the drill mud shows the impact of the moving drill string. The velocity of the drill mud is higher between the drill collar and the borehole wall because the distance is smaller, i.e. $(R_{hole} - \alpha_p R_{hole}) < (R_{hole} - \alpha_c R_{hole})$. Hence, the force acting on the drill collar is larger than the one acting on the drillpipe.

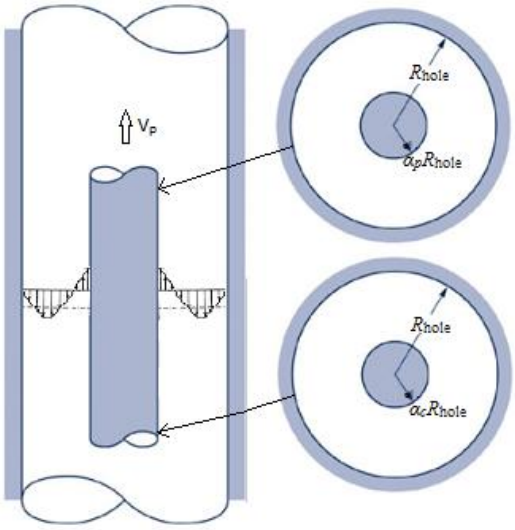


**Figure A-1:** The viscous forces acting on the drillpipe and the drill collar when POOH. $R_{hole}$ is the radius of the borehole, $\alpha_p R_{hole}$ and $\alpha_c R_{hole}$ are radiuses of the drillpipe and drill the collar, respectively.

In order to derive a useful equation for the viscous friction force, it is necessary to generate the following assumptions, where we assume that

- the mud pump is turned off and no circulation in the mud.
- the fluid is Newtonian, i.e. $\tau_w = -\mu \frac{\delta v}{\delta r}\Big|_{\alpha R_{\text{hole}}}$
- the flow is laminar, steady and axial symmetric
- the flow component is only parallel to the movement of the drillpipe, i.e. no flow in horizontal plane (**figure A-1**).

- no slip condition at the wellbore wall, $r = R_{\text{hole}}$, so that $u_i\left(R_{\text{hole}}\right) = 0$. In annulus, no slip condition on inner pipe as well, i.e. $u_i\left(\alpha_i R_{\text{hole}}\right) = \dot{q}_i$, where $\alpha_i R_{\text{hole}}$ is the outer radius of the drill string and $\dot{q}_i$ is the velocity of the drill string ($v_p$ in **figure A-1**).

Investigating the Navier-Stokes momentum equation in three-dimensional cylindrical coordinates, in the z-direction (Morrison, 2011).

$$\rho\left(\frac{\partial u_z}{\partial t} + u_r\frac{\partial u_z}{\partial r} + \frac{u_\phi}{r}\frac{\partial u_z}{\partial \phi} + u_z\frac{\partial u_z}{\partial z}\right) = -\frac{\partial p}{\partial z} + \mu\left[\frac{1}{r}\frac{\partial}{\partial r}\left(r\frac{\partial u_z}{\partial r}\right) + \frac{1}{r^2}\frac{\partial^2 u_z}{\partial \phi^2} + \frac{\partial^2 u_z}{\partial z^2}\right] + \rho g_z. \quad \text{(A.1)}$$

By applying the assumptions, equation (A.1) reduces to

$$\frac{1}{\mu}\frac{\partial p}{\partial z} = \frac{1}{r}\frac{\partial}{\partial r}\left(r\frac{\partial u_i}{\partial r}\right), \quad \text{(A.2)}$$

where $u_i$ is the axial velocity component around element $i$. Solving the differential equation:

$$\begin{aligned}
&\int 1\times\partial\left(r\frac{\partial u_i}{\partial r}\right) = \int\frac{r}{\mu}\frac{\partial p}{\partial z}\partial r \\
&r\frac{\partial u_i}{\partial r} = \frac{r^2}{2\mu}\frac{\partial p}{\partial z} + c_1 \\
&\int 1\times\partial u_i = \int\left(\frac{r}{2\mu}\frac{\partial p}{\partial z} + \frac{c_1}{r}\right)\partial r \\
&u_i = Ur^2 + c_1\ln r + c_2.
\end{aligned} \quad \text{(A.3)}$$

Here, $U = \frac{1}{4\mu}\frac{\partial p}{\partial z}$, $c_1$ and $c_2$ are constants calculated from the boundary conditions given under the assumptions. Implementing the boundary conditions into equation (A.3):

$$0 = UR_{\text{hole}}{}^2 + c_1\ln R_{\text{hole}} + c_2 \Leftrightarrow c_2 = -UR_{\text{hole}}{}^2 - c_1\ln R_{\text{hole}} \quad \text{(A.4)}$$

$$\dot{q}_i = U\alpha_i^2 R_{\text{hole}}{}^2 + c_1\ln\left(\alpha R_{\text{hole}}\right) + c_2 \quad \text{(A.5)}$$

Inserting equation (A.4) into (A.5) gives the following solution:

$$c_1 = \frac{\dot{q}_i + UR_{\text{hole}}{}^2\left(1-\alpha_i^2\right)}{\ln\left(\alpha_i\right)} \quad \text{(A.6)}$$

Equation (A.4) into (A.3) gives then:

$$u_i = -UR_{\text{hole}}{}^2\left(1-\left(\frac{r}{R_{\text{hole}}}\right)^2\right) + c_1\ln\left(\frac{r}{R_{\text{hole}}}\right) \quad \text{(A.7)}$$

Next step is to determine the pressure gradient, $\frac{\partial p}{\partial z}$. It can be determined from the volumetric flow rate in the well:

$$Q = -\pi \alpha_n^2 R_{\text{hole}}{}^2 \dot{q}_n \tag{A.8}$$

where $\alpha_n R$ is the outer radius of the drill collar ($\alpha_c R_{\text{hole}}$ in **figure A-1**). This is also equal to taking the integral of the velocity profile over the annulus (Hovda, 2015).

$$Q = \int_{\alpha_i R}^{R} 2\pi r u_i(r)\, dr = 2\pi R_{\text{hole}}{}^2 \left( -U R_{\text{hole}}{}^2 \int_{\alpha_i}^{1} \upsilon - \upsilon^3 d\upsilon + c_1 \int_{\alpha_i}^{1} \upsilon \ln(\upsilon)\, d\upsilon \right)$$

$$= 2\pi R_{\text{hole}}{}^2 \left( -U R_{\text{hole}}{}^2 \left( -\frac{1}{4}\left(1-\alpha_i^4\right) + \frac{1}{2}\left(1-\alpha_i^2\right) \right) + c_1 \left( -\frac{1}{4}\left(1-\alpha_i^2\right) - \frac{1}{2}\alpha_i^2 \ln(\alpha_i) \right) \right)$$

$$= \frac{\pi R_{\text{hole}}{}^2}{2} \left( U R_{\text{hole}}{}^2 \left( \left(1-\alpha_i^4\right) - 2U R_{\text{hole}}{}^2 \left(1-\alpha_i^2\right)\left(1+\alpha_i^2\right) + \frac{-U R_{\text{hole}}{}^2 \left(1-\alpha_i^2\right)^2 - \left(1-\alpha_i^2\right)\dot{q}_i}{\ln(\alpha_i)} - 2\alpha_i^2 \dot{q}_i \right) \right)$$

This leads to:

$$Q = \frac{\pi R_{\text{hole}}{}^2}{2} \left( -U R_{\text{hole}}{}^2 \left(1-\alpha_i^4\right) - \frac{U R_{\text{hole}}{}^2 \left(1-\alpha_i^2\right)^2 + \left(1-\alpha_i^2\right)\dot{q}_i}{\ln(\alpha_i)} - 2\alpha_i^2 \dot{q}_i \right). \tag{A.9}$$

It was necessary to make the assumption that $\dot{q}_n = \dot{q}_i$ in order to derive a useful expression for the viscous friction force. From equation (A.8) and (A.9), we get an expression for $U$:

$$U = -\frac{\phi_i \dot{q}_i}{R_{\text{hole}}{}^2} \quad \text{where} \quad \phi_i = \frac{2\left(\alpha_i^2 - \alpha_n^2\right)\ln(\alpha_i) + 1 - \alpha_i^2}{\left(1-\alpha_i^4\right)\ln(\alpha_i) + \left(1-\alpha_i^2\right)^2}. \tag{A.10}$$

Inserting equation (A.10) into (A.7) gives an expression for the velocity:

$$u_i = \dot{q}_i \left( \phi_i \left( 1 - \left( \frac{r}{R_{\text{hole}}} \right)^2 \right) + \frac{1 - \phi_i\left(1-\alpha_i^2\right)}{\ln(\alpha_i)} \ln\left( \frac{r}{R_{\text{hole}}} \right) \right) \tag{A.11}$$

The derivative of (A.11) is:

$$\frac{\partial u_i}{\partial r} = \dot{q}_i \left( \frac{1 - \phi_i\left(1-\alpha_i^2\right)}{r \ln(\alpha_i)} - \frac{2\phi_i}{R_{\text{hole}}{}^2} r \right). \tag{A.12}$$

The viscous friction force acting on element $i$ $(L_i)$ is given by:

$$R_i = -2\pi R_{\text{hole}} L_i \mu \left. \frac{\partial u_i}{\partial r} \right|_{\alpha_i R_{hole}} \tag{A.13}$$

Finally, by inserting equations (A.11) and (A.12) into (A.13), we can derive an expression for the viscous friction force acting on element $i$ $\left(L_i\right)$ (Hovda, 2015).

$$R_i = -2\pi R_{\text{hole}} L_i \mu \left. \frac{\partial u_i}{\partial r} \right|_{\alpha_i R}$$

$$R_i = -2\pi L_i \mu \dot{q}_i \left( \frac{1-\phi_i\left(1-\alpha_i^2\right)}{\ln\left(\alpha_i\right)} - 2\phi_i \alpha_i^2 \right)$$

$$R_i = -2\pi L_i \mu \dot{q}_i \left( \frac{2\left(1-\alpha_i^2\right)^2 + \left(\alpha_i^2-\alpha_n^2\right)^2 - \left(1-\alpha_n^2\right)^2 - 4\alpha_i^2\left(\alpha_i^2-\alpha_n^2\right)^2 \ln\left(\alpha_i\right)}{\left(1-\alpha_i^4\right)\ln\left(\alpha_i\right) + \left(1-\alpha_i^2\right)^2} \right) \tag{A.14}$$

# B Complex Number Representation

Recalling equation (2.20) and (2.21) from section 2.2.4:

$$\ddot{x}_i + 2\varsigma_i\omega_i\dot{x}_i + \omega_i^2 x_i = -V_{1i}k_1Q_d\sin(\omega t), \tag{2.20}$$

$$x_i(t) = A_i\sin(\omega t + \psi_i). \tag{2.21}$$

The method used to determine $A_i$ and the phase shift $\psi_i$, is by using the relation between sine- and cosine functions and the exponential function with the imaginary argument. This relation is known as Euler's formula and states that

$$e^{ix} = \cos x + i\sin x, \tag{B.1}$$

where $i = \sqrt{-1}$ is the imaginary unit. Obviously, $e^{ix}$ is a complex quantity with $\cos x$ as the real part and $i\sin x$ as the imaginary part. Observing that equation (2.21) is the imaginary part of the complex function $A_ie^{i(\omega t+\psi_i)}$ and the right-hand side of equation (2.20) is the imaginary part of $-V_{1i}k_1Q_de^{i\omega t}$. Hence, by taking the expression

$$x(t) = A_ie^{i(\omega t+\psi_i)} \tag{B.2}$$

and substituting it into the modified version of the equation (2.20), i.e.:

$$\ddot{x}_i + 2\varsigma_i\omega_i\dot{x}_i + \omega_i^2 x_i = -V_{1i}k_1Q_de^{i\omega t}, \tag{B.3}$$

then the 'imaginary part' of equation (B.2) is a solution of (2.21) if equation (B.2) is a solution of (B.3). Therefore, substituting gives:

$$\left(-\omega^2 + 2\varsigma_i\omega_i\omega i + \omega_i^2\right)A_ie^{i(\omega t+\psi_i)} = -V_{1i}k_iQ_de^{i\omega t}.$$

Dividing out the common factor $e^{i\omega t}$ and re-arranging to obtain

$$A_ie^{i\psi_i} = -\frac{V_{1i}k_iQ_d}{\omega_i^2 - \omega^2 + 2\varsigma_i\omega_i\omega i}.$$

Inverting this and expanding the exponential function using equation (B.1):

$$\frac{1}{A_i}e^{-i\psi_i} = \frac{1}{A_i}\left(\cos\psi_i - i\sin\psi_i\right) = -\frac{\omega_i^2 - \omega^2 + 2\varsigma_i\omega_i\omega i}{V_{1i}k_iQ_d}.$$

By evaluating the equation, it is possible to see that

$$\frac{1}{A_i}\cos\psi_i = \frac{\omega_i^2 - \omega^2}{V_{1i}k_iQ_d} \quad \text{and} \quad \frac{1}{A_i}\sin\psi_i = \frac{2\varsigma_i\omega_i\omega}{V_{1i}k_iQ_d}. \tag{B.4}$$

Squaring each of equation (B.4), adding and re-arranging gives:

$$\frac{1}{A_i^2}\left(\cos^2\psi_i + \sin^2\psi_i\right) = \frac{\left(\omega_i^2 - \omega^2\right)^2 + \left(2\varsigma_i\omega_i\omega\right)^2}{\left(V_{1i}k_iQ_d\right)^2}. \tag{B.5}$$

Hence

$$A_i = \frac{V_{1i}k_iQ_d}{\sqrt{\left(\omega_i^2 - \omega^2\right)^2 + c^2\omega^2}}. \tag{B.6}$$

By dividing the imaginary part of equation (B.4) by the real part of equation (B.4), we obtain:

$$\psi_i = \arctan\left(\frac{c\omega}{\omega^2 - \omega_i^2}\right),$$

where $c = 2\varsigma_i\omega_i$.

# C LabVIEW Program

## C.1 Front Panel

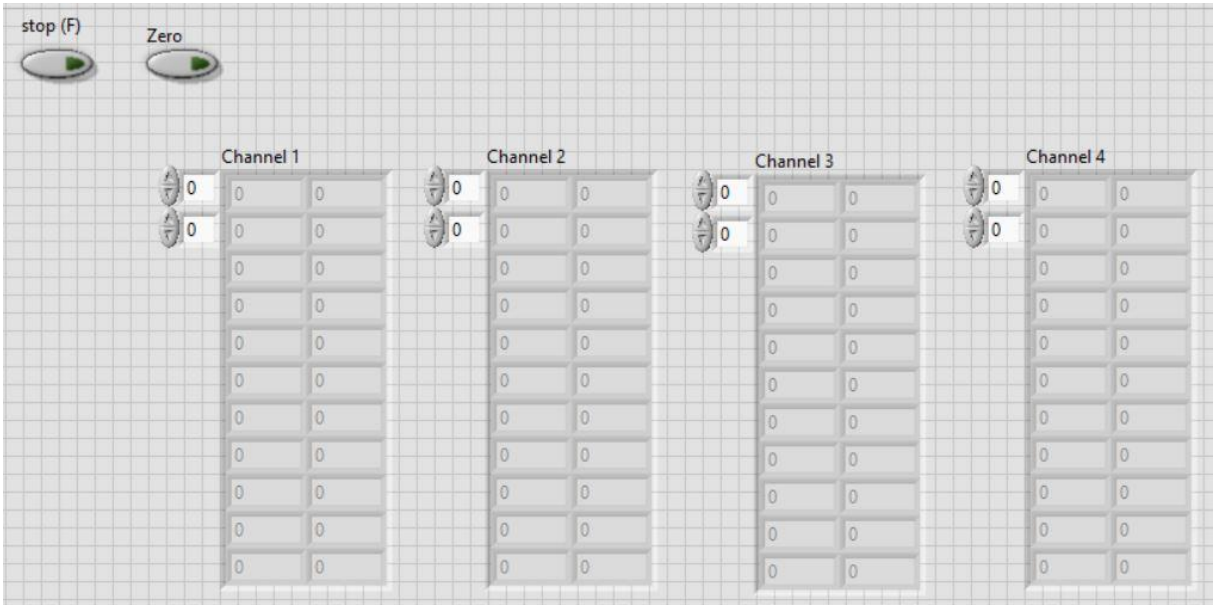


**Figure C-1:** Front panel of the LabVIEW program. Channel 1-4 indicate the measuring elements. Two columns are aligned to each channel. Left one is for time and right one for measured resistance in the strain gauge circuit. The function stop (F) breaks the measuring process The offset nulling the circuit is done by the function Zero.

**Figure C-1** illustrates the front panel of the LabVIEW program. It is primarily used to run the measurements, stop the measuring process (stop (F)), and to offset nulling the circuit (Zero). The program measures with an accuracy of 7 decimals.

## C.2 Block Diagram

**Figure C-2** illustrates the block diagram of the LabVIEW program.

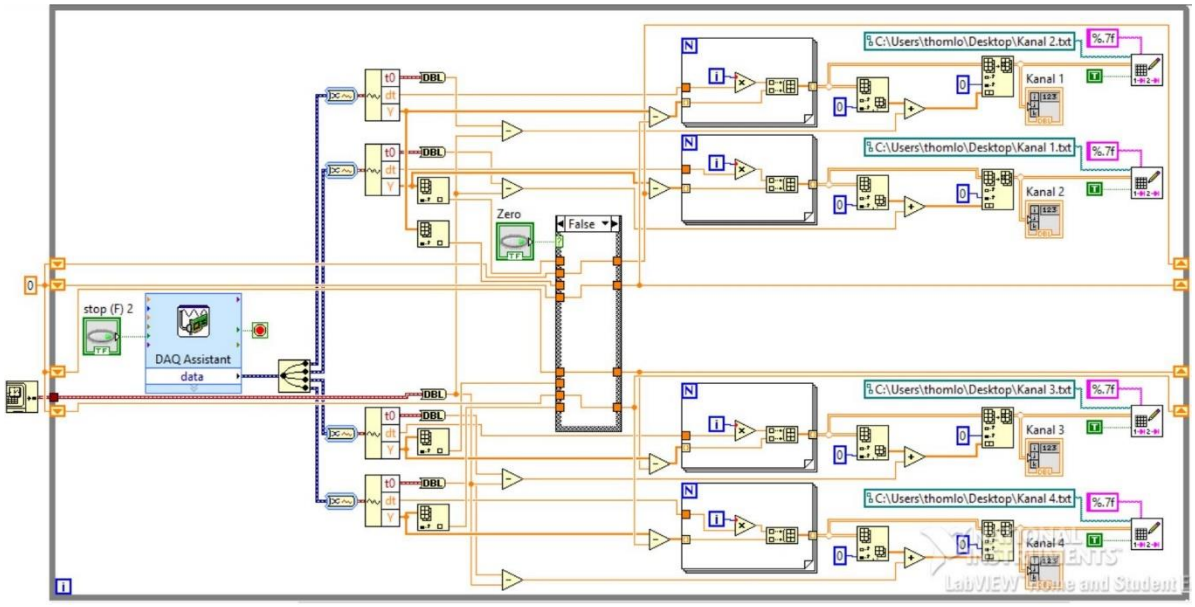


**Figure C-2:** The block diagram of the LabVIEW program.

# D Savitzky-Golay Filtering Method

MathWorks (2016) describes the Savitzky-Golay filtering method as:

Savitzky-Golay smoothing filters (also called digital smoothing polynomial filters or least-squares smoothing filters) are typically used to "smooth out" a noisy signal whose frequency span (without noise) is large. In this type of application, Savitzky-Golay smoothing filters perform much better than standard averaging finite impulse response (FIR) filters, which tend to filter out a significant portion of the signal's high frequency content along with the noise. Although Savitzky-Golay filters are more effective at preserving the pertinent high frequency components of the signal. Savitzky-Golay filters are optimal in the sense that they minimize the least-squares error in fitting a polynomial to frames of noisy data.

Basically, Savitzky & Golay (1964) showed that a set of integers, i.e. $A_{-n}, A_{-n+1}, \ldots, A_n, A_n$, can be derived and used as weighting coefficients to perform the smoothing process. These weighting coefficients are known as convolution integers. Savitzky and Golay proved that the use of these convolution integers are equivalent with the process of fitting the data to a polynomial. In comparison, the method is computationally more effective and much faster. Hence, the smoothed data point, $(y_k)_s$, by the Savitzky-Golay algorithm is given by the following equation (Efstathiou, 2000):

$$(y_k)_s = \frac{\sum_{i=-n}^{n} A_i y_{k+1}}{\sum_{i=-n}^{n} A_i} \tag{D.1}$$